U.S. Department
of Transportation
Federal Railroad
Administration

Office of Research,
Development and Technology
Washington, DC 20590

Side Impact Test and Analyses of a DOT-105 Tank Car – 6 X 6 Inch Indenter

DOT/FRA/ORD-20/38

Final Report | September 2020

REPORT DOCUMENTATION PAGE

Form Approved
OMB No. 0704-0188

1. REPORT DATE *(DD-MM-YYYY)*	**2. REPORT TYPE**	**3. DATES COVERED** *(From - To)*
September 2020	Technical Report	August 1, 2018

4. TITLE AND SUBTITLE

Side Impact Test and Analyses of a DOT-105 Tank Car – 6 X 6 Inch Indenter

5a. CONTRACT NUMBER
DTFR53-11-D-00008

5b. GRANT NUMBER

5c. PROGRAM ELEMENT NUMBER

6. AUTHOR(S)
Nicholas Wilson** 0000-0003-1140-7108
Shaun Eshraghi* 0000-0002-8152-0838
Shawn Trevithick** 0000-0001-6155-5526
Michael Carolan* 0000-0002-8758-5739
Przemyslaw Rakoczy** 0000-0002-1924-7172

5d. PROJECT NUMBER

5e. TASK NUMBER
Task Order 008

5f. WORK UNIT NUMBER

7. PERFORMING ORGANIZATION NAME(S) AND ADDRESS(ES)
*Volpe National Transportation Systems Center
55 Broadway, Cambridge, MA 02142
**Transportation Technology Center, Inc.
55500 DOT Road, Pueblo, CO 81001

8. PERFORMING ORGANIZATION REPORT NUMBER

9. SPONSORING/MONITORING AGENCY NAME(S) AND ADDRESS(ES)
U.S. Department of Transportation
Federal Railroad Administration
Office of Railroad Policy and Development
Office of Research, Development and Technology
Washington, DC 20590

10. SPONSOR/MONITOR'S ACRONYM(S)

11. SPONSOR/MONITOR'S REPORT NUMBER(S)
DOT/FRA/ORD-20/38

12. DISTRIBUTION/AVAILABILITY STATEMENT
This document is available to the public through the FRA website

13. SUPPLEMENTARY NOTES
COR: Francisco González, III

14. ABSTRACT

The Federal Railroad Administration (FRA) conducted a side impact test on a DOT-105 tank car at the Transportation Technology Center (TTC) to evaluate its performance under dynamic impact conditions and to provide data for the verification and refinement of a computational model. The tank car was filled with water to approximately 89.5 percent of its volume and pressurized to 100 psi. A 296,775-pound ram car equipped with a 6- by 6-inch indenter struck the tank car at 9.7 mph. The ram car impacted the tank center; puncturing the tank after slowing nearly to a stop. The Volpe National Transportation Systems Center (Volpe) performed finite element (FE) modeling to estimate the overall response of the tank to the impact. The pre-test model used two different material models for the steel in the tank car shell. The pre-test model that used a lower-ductility material response was found to be in good agreement with the test results. After the test, material coupons were cut from the car and subjected to tensile testing. The post-test FE model was updated to include the actual material behavior of the test car, and continued to be in good agreement with the test measurements. The test data is intended to be useful to entities who wish to develop FE models of tank cars under similar puncture conditions in their modeling validation and verification efforts.

15. SUBJECT TERMS
Impact test, DOT-105 tank car, tank car performance, transportation safety, toxic by inhalation, TIH, finite element analysis, FEA, hazardous materials

16. SECURITY CLASSIFICATION OF:			**17. LIMITATION OF ABSTRACT**	**18. NUMBER OF PAGES**	**19a. NAME OF RESPONSIBLE PERSON**
a. REPORT	**b. ABSTRACT**	**c. THIS PAGE**			Nicholas Wilson, TTCI
Unclassified	Unclassified	Unclassified		136	**19b. TELEPHONE NUMBER** *(Include area code)* 719-584-0573

Standard Form 298 (Rev. 8/98)
Prescribed by ANSI Std. Z39.18

METRIC/ENGLISH CONVERSION FACTORS

ENGLISH TO METRIC

LENGTH (APPROXIMATE)

1 inch (in)	=	2.5 centimeters (cm)
1 foot (ft)	=	30 centimeters (cm)
1 yard (yd)	=	0.9 meter (m)
1 mile (mi)	=	1.6 kilometers (km)

AREA (APPROXIMATE)

1 square inch (sq in, in^2)	=	6.5 square centimeters (cm^2)
1 square foot (sq ft, ft^2)	=	0.09 square meter (m^2)
1 square yard (sq yd, yd^2)	=	0.8 square meter (m^2)
1 square mile (sq mi, mi^2)	=	2.6 square kilometers (km^2)
1 acre = 0.4 hectare (he)	=	4,000 square meters (m^2)

MASS - WEIGHT (APPROXIMATE)

1 ounce (oz)	=	28 grams (gm)
1 pound (lb)	=	0.45 kilogram (kg)
1 short ton = 2,000 pounds (lb)	=	0.9 tonne (t)

VOLUME (APPROXIMATE)

1 teaspoon (tsp)	=	5 milliliters (ml)
1 tablespoon (tbsp)	=	15 milliliters (ml)
1 fluid ounce (fl oz)	=	30 milliliters (ml)
1 cup (c)	=	0.24 liter (l)
1 pint (pt)	=	0.47 liter (l)
1 quart (qt)	=	0.96 liter (l)
1 gallon (gal)	=	3.8 liters (l)
1 cubic foot (cu ft, ft^3)	=	0.03 cubic meter (m^3)
1 cubic yard (cu yd, yd^3)	=	0.76 cubic meter (m^3)

TEMPERATURE (EXACT)

[(x-32)(5/9)] °F = y °C

METRIC TO ENGLISH

LENGTH (APPROXIMATE)

1 millimeter (mm)	=	0.04 inch (in)
1 centimeter (cm)	=	0.4 inch (in)
1 meter (m)	=	3.3 feet (ft)
1 meter (m)	=	1.1 yards (yd)
1 kilometer (km)	=	0.6 mile (mi)

AREA (APPROXIMATE)

1 square centimeter (cm^2)	=	0.16 square inch (sq in, in^2)
1 square meter (m^2)	=	1.2 square yards (sq yd, yd^2)
1 square kilometer (km^2)	=	0.4 square mile (sq mi, mi^2)
10,000 square meters (m^2)	=	1 hectare (ha) = 2.5 acres

MASS - WEIGHT (APPROXIMATE)

1 gram (gm)	=	0.036 ounce (oz)
1 kilogram (kg)	=	2.2 pounds (lb)
1 tonne (t)	=	1,000 kilograms (kg)
	=	1.1 short tons

VOLUME (APPROXIMATE)

1 milliliter (ml)	=	0.03 fluid ounce (fl oz)
1 liter (l)	=	2.1 pints (pt)
1 liter (l)	=	1.06 quarts (qt)
1 liter (l)	=	0.26 gallon (gal)
1 cubic meter (m^3)	=	36 cubic feet (cu ft, ft^3)
1 cubic meter (m^3)	=	1.3 cubic yards (cu yd, yd^3)

TEMPERATURE (EXACT)

[(9/5) y + 32] °C = x °F

QUICK INCH - CENTIMETER LENGTH CONVERSION

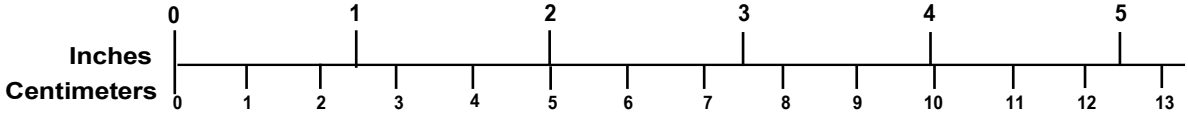

QUICK FAHRENHEIT - CELSIUS TEMPERATURE CONVERSIO

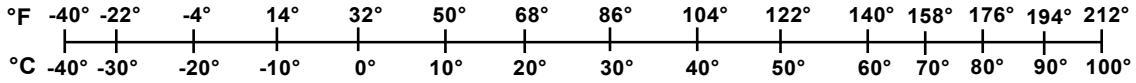

For more exact and or other conversion factors, see NIST Miscellaneous Publication 286, Units of Weights and Measures. Price $2.50 SD Catalog No. C13 10286

Updated 6/17/98

Acknowledgements

Special thanks to Axiall Chemical for donating the DOT-105 tank car used in this impact test to the Federal Railroad Administration (FRA).

The authors of this report gratefully acknowledge the technical assistance of the Volpe National Transportation Systems Center's Senior Engineer Benjamin Perlman. Additionally, discussions with Francisco González, III of FRA's Office of Research, Development and Technology were valuable in developing this testing program.

Contents

Illustrations

Tables

Equations

Executive Summary

The test and analyses described in this report support the overall objective of the Federal Railroad Administration's (FRA) research program to improve transportation safety for tank cars. This report documents the combined efforts of Transportation Technology Center, Inc. (TTCI) and the Volpe National Transportation Systems Center (Volpe) to test and analyze the side impact puncture performance of a DOT-105A500W (DOT-105) tank car. FRA conducted the impact test at the Transportation Technology Center (TTC) on August 1, 2018, to evaluate the performance of the tank car and to provide data for the validation and refinement of a computational model. All test requirements were met. Volpe performed both pre-test and post-test analyses of the impact response to evaluate and improve the capabilities of the modeling tank car puncture involving fluid-structure interaction and material failure.

The tank car was filled with water to approximately 89.5 percent of its volume. It was then sealed and pressurized to 100 psi. A 296,775-pound ram car traveling at 9.7 mph impacted the tank car. A 6-inch by 6-inch ram head fitted to the ram car impacted the tank center. The impact resulted in puncture of the tank as the tank car rebounded off the impact wall, which indicated that the impact occurred at a speed only slightly above the puncture/non-puncture threshold speed for these test conditions.

Pre-test finite element (FE) modeling was used to estimate the overall response of the tank to the impact, including the force-displacement response. While it was known before the test that the tank car heads and shell were made of TC128 steel, the exact material properties (i.e., yield strength, ultimate tensile strength (UTS), and ductility) were not known for this specific tank car. Therefore, the pre-test model was run using two different TC128 characteristics based on previously encountered TC128 samples. The pre-test model that used a lower-ductility TC128 material response was found to be in good agreement with the test results, including estimation of puncture at the test speed.

After the test, material coupons were cut from the tank car shell and subjected to tensile testing. The material characterization indicated that the actual tank car material had similar mechanical properties to the lower-ductility material used in the pre-test models. Updating the post-test model to include the actual material response allowed the model to continue to exhibit qualitative and quantitative agreement with the test results. The post-test model was conservative, meaning the post-test model estimated puncture at a speed lower than that measured during the test.

The intent of sharing the results of this test, including test data, photos, and videos, is to permit interested parties to attempt to validate and verify their own FE models simulating tank car shell impacts. The authors hope that by comparing model results to test measurements, confidence can be developed in the modeling techniques (e.g., modeling software, element type, fluid representation, material behaviors, etc.) used to represent the impact conditions of the test. Model validation efforts are an essential part of any process where FE simulations are to be used to represent tank car impact conditions that have not been tested.

1. Introduction

1.1 Background

In recent years, significant research has been conducted to analyze and improve the impact behavior and puncture resistance of railroad tank cars. Ultimately, the results of this research can be used by the Government regulatory agencies in the United States and Canada—FRA and Transport Canada (TC), respectively—to establish performance-based testing requirements and to develop methods to evaluate the crashworthiness and structural integrity of different tank car designs when subjected to a standardized shell impact scenario. A performance-based requirement for tank car head impact protection has already been defined within the current regulations (Pipeline and Hazardous Materials Safety Administration, U.S. Department of Transportation, 2015).

FRA has a continuing research program to provide the technical basis for rulemaking on enhanced and alternative performance standards for tank cars and review of new and innovative designs that are developed by the industry and other countries. In support of this ongoing research program, full-scale tests are necessary to provide the technical information to validate modeling efforts and to inform regulatory activities. These tests evaluate the crashworthiness performance of tank cars used in the transportation of hazardous materials including designs that comply with current regulations as well as innovative new designs that have improved puncture resistance. FRA is currently working closely with key industry stakeholders to use the information being generated from these programs to revise and refine the construction, design, and use of tank cars.

This report documents the analyses and test results for a side impact test performed on a DOT-105 tank car. The DOT-105 tank car is a current design pressurized car equipped with head protection and thermal protection enclosed in an exterior jacket. This report documents the impact test and describes the finite element (FE) model development and pre-test estimates, the comparisons of the test and analyses, and the subsequent post-test analyses performed to address the variations between the pre-test analyses and actual test conditions.

1.2 Objectives

The objective of the test was to quantify the deformation mode, impact load-time history, and puncture resistance of an existing DOT-105 tank car in a side impact. This test was also intended to provide test data that would be made publicly available to further model validation efforts. Moreover, the impact conditions were developed so that the side impact test is: 1) safe; 2) repeatable; and 3) analyzable.

The objective of the analyses was to estimate the tank car impact response both for pre-test planning and for validation of tank car impact and puncture modeling capabilities.

1.3 Scope

This report includes a discussion of developing and executing the FE models for this program, including modeling the tank car steel, modeling the water within the tank, and modeling the gas phase outage within the tank. This report presents the test results, discusses the execution of the test, and summarizes the overall results of the test. A discussion is included in the report of the

post-test modeling adjustments. Finally, this report presents a comparison between the test measurements and the model results.

This report does not include any results from further analyses using the DOT-105 tank car model, such as impact conditions outside of the conditions of the test. While this report refers to previously-performed shell impact tests on tank cars of different specifications (Kirkpatrick, S., Rakoczy, P., MacNeill, R. A., & Anderson, A, 2015) (Rakoczy, P., & Carolan, M, 2016) (Kirkpatrick, S. W, 2010) (Carolan, M. E., et al, 2013) (Yu, H., Jeong, D. Y., Gordon, J. E., & Tang, Y. H, 2007) (Tang, Y. H., Yu, H., Gordon, J. E., Jeong, D. Y., & Perlman, A. B, 2008) (Yu, H., Tang, Y.H. Gordon, J. E., & Jeong, D. Y, 2009) (Carolan, M., & Rakoczy, P., 2019) (Rakoczy, P., Carolan, M., Gorhum, T., & Eshraghi, S., 2019), no comparisons of results from different tests are included within the scope of this report. Research into the puncture resistance of tank cars is ongoing, and such further simulations or comparisons may be considered in future work.

1.4 Overall Approach

Because of the difficult-to-control variables of testing, such as wind speed, unknown weld qualities, and the inherent variability of material behavior even within a single plate, there is no such thing as a certain test outcome. It is more useful to frame the discussion of test planning in terms of likelihood of puncture. In an ideal test, the chosen target test speed would fall somewhere in the shaded range in Figure 1 where puncture is possible, but not certain.

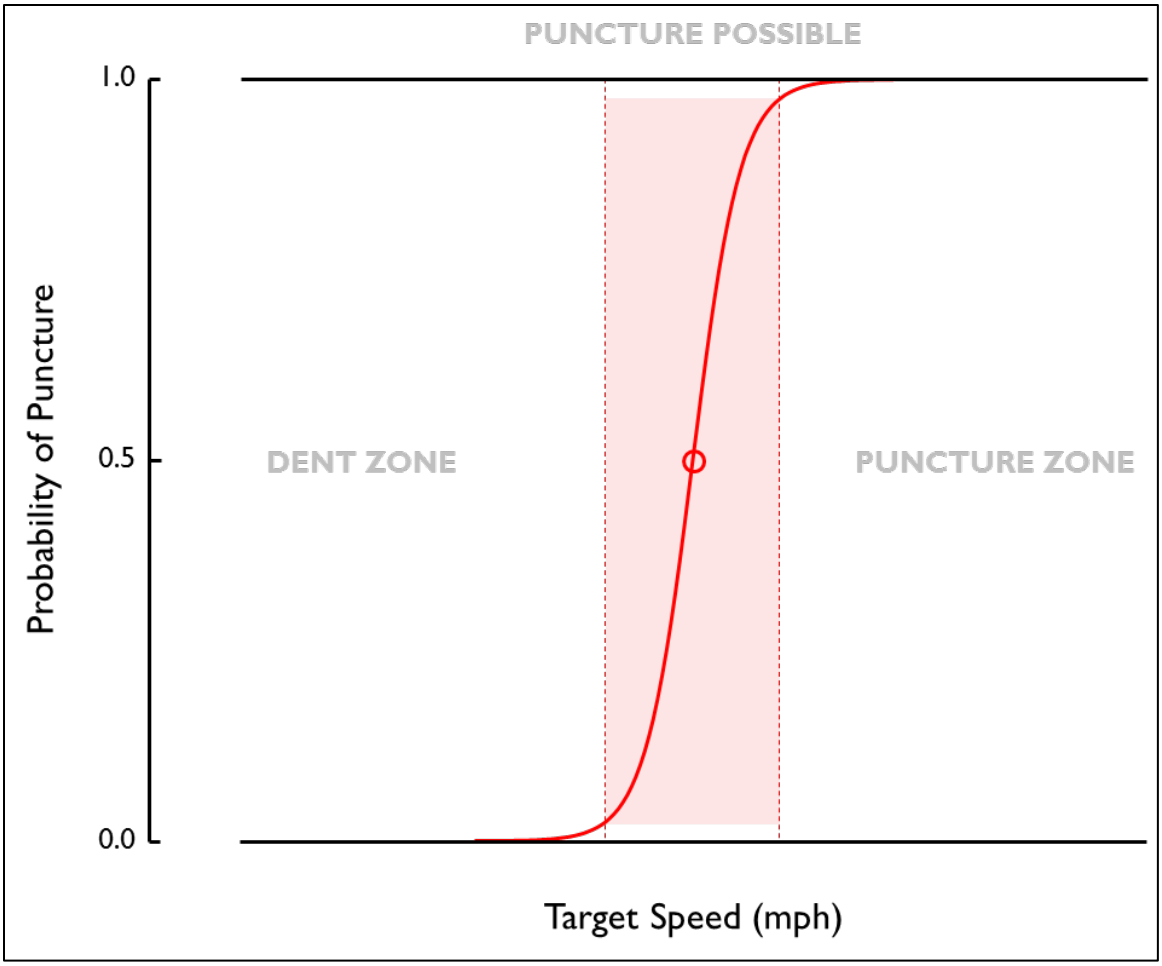

Figure 1. Schematic of Probability of Puncture vs. Impact Speed

The value of a test can be increased by targeting an impact speed that is very close to the threshold speed. This is the speed between where the tank car punctures and where it does not puncture for a given impactor shape, size, and mass. If the tested tank speed is close to this threshold speed, regardless of whether or not the tank punctures, the data that is collected can be extremely valuable both for model validation and for estimating the threshold puncture speed under the given impact conditions. From the standpoint of test execution, the ideal range of test speeds provides a practical target to maximize the value of the test. One potential target for maximizing the value of the test data could be to run a test where the impactor is brought to a complete stop at the instant the tank punctures. Such a test would be an experimental demonstration of the threshold puncture speed because all the ram car's initial kinetic energy has been transferred into the tank car at the same instant that the tank car reaches the limit of its capacity. An incrementally slower test would have been a non-puncture test, and an incrementally faster test would have exceeded the capacity of the tank car to resist puncturing.

In the same spirit, making a blanket statement as to the superiority of a puncture test or a non-puncture test does not support a useful discussion without considering proximity to the theoretical threshold puncture speed. As the test speed moves farther from the center of the puncture threshold range, the value of the test data decreases. Neither a test that causes catastrophic damage to the tank car structure, nor a test that scarcely creates a dent would be an

effective tool for evaluating the puncture resistance of the car. These tests also would not provide much utility for model validation, evaluating the relative impact resistance offered by different tank car designs, or for evaluating new or novel methods of simulating impacts. The extremely unlikely-to-puncture case does not provide enough information to assess the model sufficiently to make a comparison, and the overwhelmingly likely-to-puncture case can result in a mode of tank failure that does not truly represent the way tank cars experience puncture near their puncture/non-puncture thresholds.

The force response of an impacted tank car is highly nonlinear. This makes extrapolation or interpolation of test results to attempt to calculate the threshold speed between puncture and non-puncture challenging. The uncertainty of an interpolation or extrapolation increases when the test speed is either significantly higher or significantly lower than the threshold speed. Thus, if test results are obtained at speeds far away from the theoretical threshold puncture speed, the threshold puncture speed will not be known with a high degree of certainty.

A test that punctures the tank but does not leave the impactor with an excessive amount of residual kinetic energy can be used to verify that a model captures both the overall response of the tank car and the puncture modeling techniques defined for the materials of the car. However, achieving this outcome can be extremely challenging. A test may be planned to be run at slightly above the threshold puncture speed. The threshold puncture speed is typically estimated from pre-test models. If the pre-test model predicts a higher threshold puncture speed than the tank car actually possesses, then a test planned at that speed may in fact be an excessively fast test. While the energy absorbed by the tank up to the point of puncture in the test can be used to estimate the energy necessary to cause puncture, this estimate becomes less reliable as the actual impact speed gets farther from the threshold puncture speed. At the same time, if the pre-test model is overly conservative, then a test that is planned for just below the threshold puncture speed based on a conservative model may in fact result in an impact speed that is well below the threshold puncture speed.

Figure 2 shows a flowchart that presents a schematic view of the overall approach followed by the Volpe National Transportation Systems Center's (Volpe) FE model development and Transportation Technology Center Inc.'s (TTCI) development and execution of the test. The flowchart illustrates the collaboration between both Volpe and TTCI throughout the testing and modeling process, all of which was coordinated with FRA. For example, the instrumentation placement described in the test plan guided requests for corresponding results in the FE model. The model results were then used to estimate the magnitude of the response (e.g., such as pressure or displacement) that the instrumentation would experience at that location. If necessary, the instrumentation in the test plan could be updated to account for the expected response.

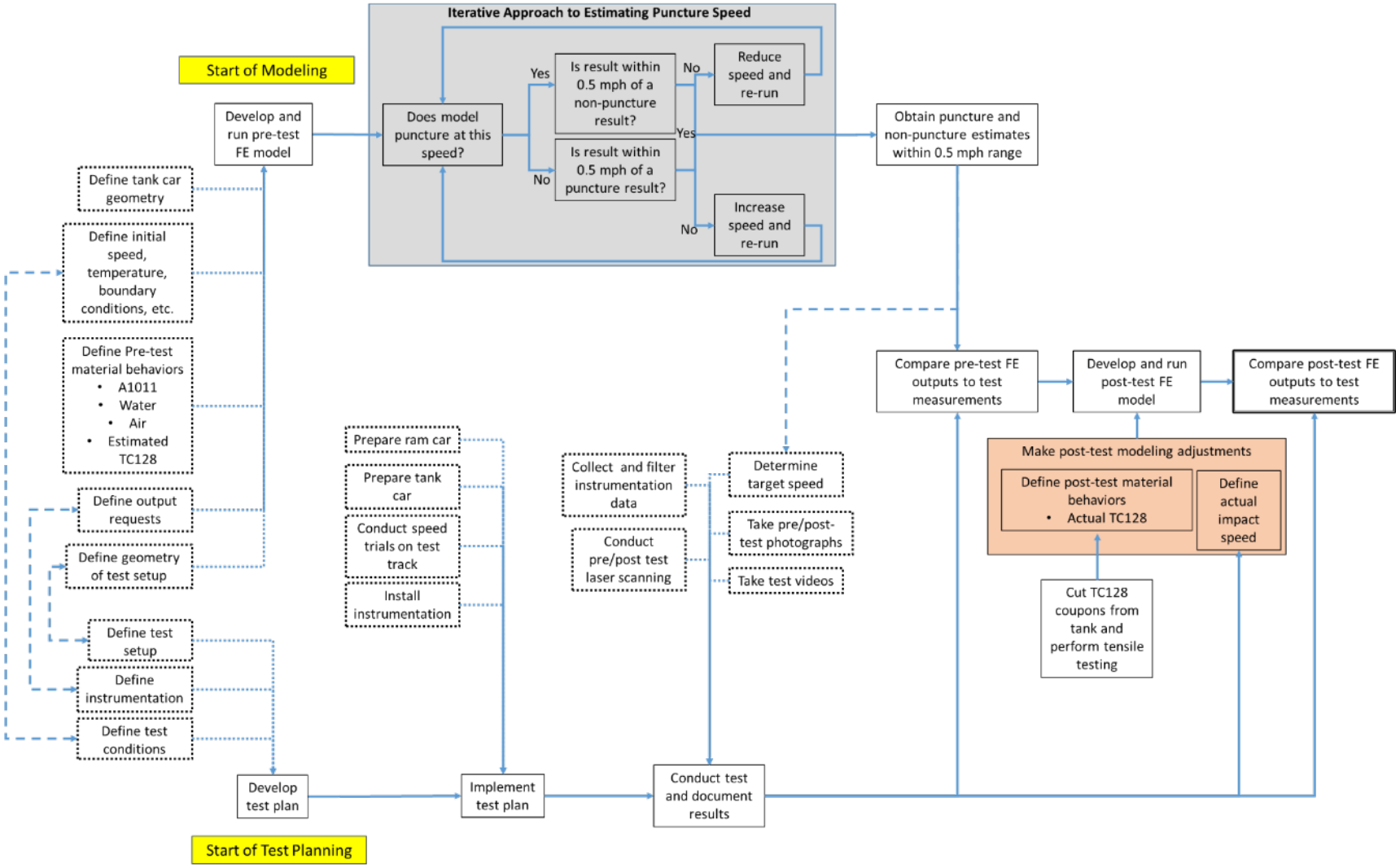

Figure 2. Flowchart of Overall Modeling and Testing Approach

Prior to the test itself, Volpe, TTCI, and FRA collaborated to determine the target test speed based on the pre-test FE model estimates, the desired outcome of the test, and such factors as ambient conditions (e.g., wind speed influencing actual impact speed) at the time of the test. After the test, the authors used the material coupon test data from the TC128 shell of the car and the measured test speed to update the pre-test FE model to reflect the actual test conditions. Finally, a comparison of the post-test FE model results and the test measurement results took place.

1.5 Organization of the Report

Section 1 introduces the test and analyses conducted for this project and a summation of results.

Section 2 describes the tank car undergoing testing and analyses, and it describes the shell impact test setup.

Section 3 describes the instrumentation used during the test and its placement. This description includes a discussion of the cameras used to capture the impact event.

Section 4 presents the results of the test. These results include a description of the actual conditions of the impact, a description of the test itself, and a summary of the measured test data.

Section 5 describes the development of the FE models used in this program. This section describes the geometry used in the model, the different material models developed, and modeling techniques used in the pre- and post-test FE models.

Section 6 presents test measurements alongside the corresponding estimates from the pre-test FE models.

Section 7 presents test measurements alongside the corresponding estimates from the post-test FE models.

Section 8 includes a summary of the report and concluding remarks.

Appendix A describes the positions of the cameras and targets used in the test.

Appendix B contains the full set of test data, and also the material data measured during the tensile coupon tests for the TC128 steel making up the car's shell.

Appendix C contains a full set of comparisons for pre-test FE models using two different material behaviors, and for the post-test FE model using the actual TC128 behavior.

Appendix D describes the geometry and mesh on each part used in the FE models.

Appendix E contains a description of the modeling techniques used in both the pre- and post-test FE models.

Appendix F contains a description of the development of each material behavior in the FE models.

2. Test Conditions

2.1 Tank Car

The DOT-105 tank car is a pressurized tank car used in North America to carry pressurized gases. It is equipped with head protection and foam insulation enclosed in the exterior jacket. According to the certificate of construction, this car was constructed between 1979 and 1980. The 0.775-inch thick tank car shell is constructed with TC-128 Grade B steel. The tank was made of a cylindrical shell with an inside diameter of 100.45 inches. The tank itself was covered with a 4-inch layer of foam insulation having a density of 2 pounds per cubic foot, which is enclosed within an 11-gauge steel jacket. The jacket had an inside diameter of 110 inches. Previously, FRA conducted a puncture test using a 12-inch by 12-inch impactor on another DOT-105 tank car built under this certificate of construction (Carolan, M., & Rakoczy, P., 2019).

Figure 3 shows the general arrangement drawings for an example DOT-105 tank car (Elkins, A, 2017).

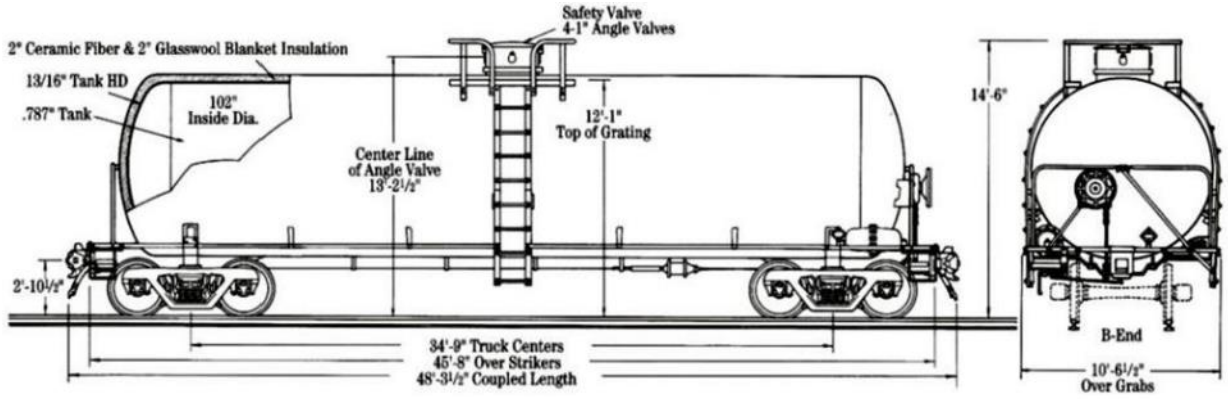

Figure 3. Example DOT-105 Tank Car Design Specification

The certificate of construction for the group of tank cars including the tested DOT-105 listed its full water capacity as 17,360 gallons. The car was designed to carry a commodity having a density of approximately 11.74 pounds per gallon at 68 °F. Because the test used water within the tank, the tank car in the test would be somewhat lighter than a car filled to the same level with the design commodity. The outage for the test conditions was obtained using the loading procedure described in Section 2.2.

2.2 Test Setup

On August 1, 2018, FRA performed the test at the Transportation Technology Center (TTC) in Pueblo, CO. The test was performed by sending a ram car into the side of the tank car, which was mounted on skids and backed by a rigid impact barrier as shown in Figure 4.

Figure 4. Target Tank Mounted on Support Skids

Researchers visually inspected the tank car structure and all interior welds before the test for any damage or evidence of repair.

Figure 5(a) shows one of the two skids that the tank car was placed on, oriented parallel to the track with one side near the impact barrier. Four sections of I-beams were welded to the tank car and skids for the attachment, as Figure 5(b) shows. The tank car with skids attached was placed on 1-inch steel plates. The design of this test configuration was to minimize the tank car rollback and allow the tank car on the skids to slide on the steel plates during the impact.

(a) Support skids (b) Welded I-beam connection

Figure 5. Tank Support Skid System (i.e., from a previous test)

The tank car jacket and shell were not modified in any way. The tank car ladder would have interfered with the impactor; therefore, it was removed before the test. The authors used water as

the lading for this test, in lieu of any commodity typically carried in this type of car. The tank car was filled with water until the shell was full. This capacity was measured as 17,132 gallons. Based on a desired outage of 10.6 percent, 1,793 gallons of water was then pumped out of the tank. The height from the top of the water to the top of the tank was measured to be approximately 16.5 inches. The manhole lid was sealed, and the car was pressurized to 100 psi just before the test.

The indenter was positioned to align with the mid-length and mid-height of the target tank car as closely as possible. Figure 6 shows the ram car. For this test, researchers used a 6-inch by 6-inch indenter with 0.5-inch radii on the edges and corners.

Figure 6. Ram Car and Head (i.e., from a previous test with 6-inch by 6-inch indenter)

Figure 7 and Figure 8 show the indenter attached to the ram car and aligned with the tank car. To confirm the actual weight of the ram car, researchers weighed it before the test. The measured weight was 296,775 pounds.

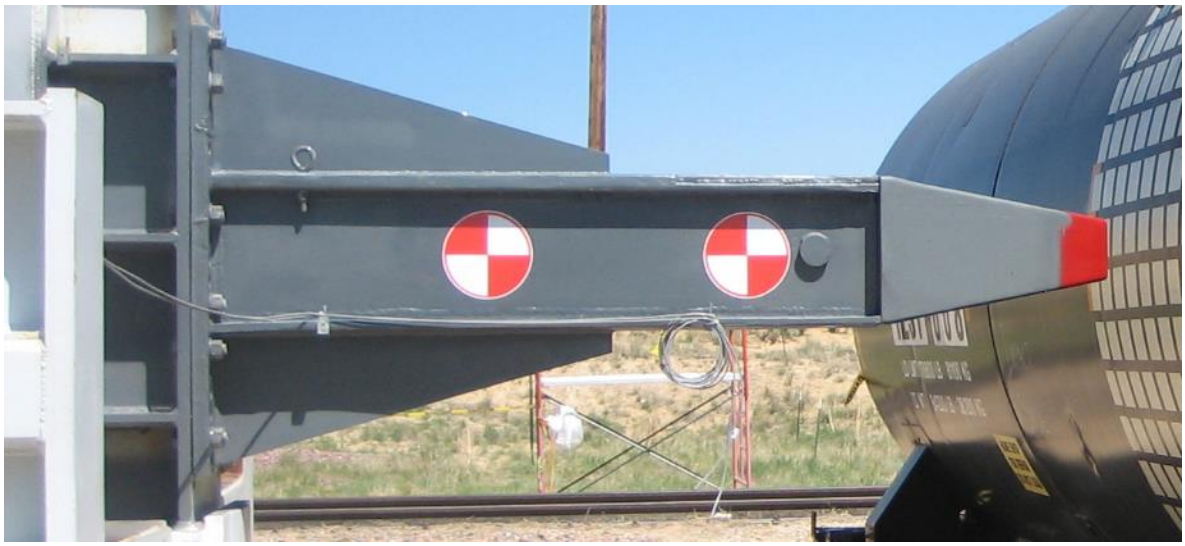

Figure 7. Ram Arm with 6-inch by 6-inch Indenter

Figure 8. Overall Test Setup (left) and Ram Arm with 6-inch by 6-inch Indenter Aligned with Center of the Tank Car (right)

3. Test Instrumentation

3.1 Overview

The test configuration and instrumentation were all consistent with the specifications of the test implementation plan (Transportation Technology Center, Inc., 2016). Table 1 provides a list of all instrumentation used for this test. Additional descriptions of the various types of instrumentation are provided in the following subsections.

Table 1. Instrumentation Summary

Type of Instrumentation	Channel Count
Accelerometers	11
Speed Sensors	2
Pressure Transducers	13
String Potentiometers	10
Total Data Channels	36
Digital Video	6 Cameras (including 4 high speed cameras)

3.2 Ram Car Accelerometers and Speed Sensors

The local acceleration coordinate systems were defined relative to the ram car. Positive x, y, and z directions were forward, left, and up relative to the lead end of the ram.

TTCI personnel mounted three triaxial accelerometers on the longitudinal centerline of the ram car at the front, rear, and near the middle of the car. They also mounted two uniaxial accelerometers on the left and right sides of the car to supplement recording of longitudinal acceleration. Figure 9 illustrates the positions of these accelerometers. A summary of the ram car accelerometer types and positions are provided in Table 2.

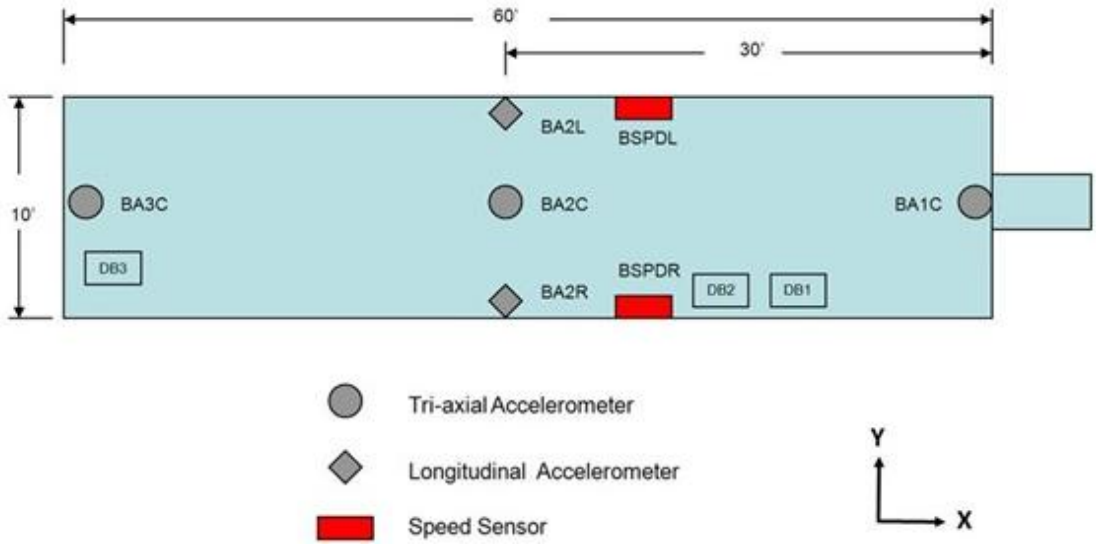

Figure 9. Ram Car Instrumentation

Table 2. Ram Car Accelerometers

Channel Name	Sensor Description	Range
BA1CX	Leading end, Centerline, X Accel	200g
BA1CY	Leading end, Centerline, Y Accel	100g
BA1CZ	Leading, Centerline, Z Accel	200g
BA2LX	Middle, Left Side X Accel	100g
BA2CX	Middle, Centerline, X Accel	50g
BA2CY	Middle, Centerline, Y Accel	50g
BA2CZ	Middle, Centerline, Z Accel	50g
BA2RX	Middle, Right Side X Accel	100g
BA3CX	Trailing end, Centerline, X Accel	200g
BA3CY	Trailing end, Centerline, Y Accel	100g
BA3CZ	Trailing end, Centerline, Z Accel	200g

To provide accurate measurement of the car's speed within 2 feet of the impact point, researchers mounted the speed sensors on both sides of the ram car. The speed sensors were reflector-based light sensors. They use ground reflectors separated by a known distance in conjunction with light sensors mounted on the car that trigger as the car passes over the reflector. The position of the last reflector aligned with the sensor when the ram head was within a few inches of the impact point. The time interval between passing the reflectors was recorded, and speed was calculated from distance and time. A handheld radar gun was also used to take supplemental speed measurements.

3.3 Tank Car String Potentiometers and Pressure Transducers

The local displacement coordinate systems (except for the tank head) are defined relative to the tank car. Positive x, y, and z directions are forward, right (away from the wall), and up relative to the A-end of the tank car. Tank head displacements are positive toward the impact wall.

Six string potentiometers were used to measure the tank crush displacements around the immediate impact zone during the test. Five string potentiometers measured the dent formation of the tank at the tank center and at locations 24 inches and 48 inches to either side of the impact point. The sixth string potentiometer measured the vertical deformations of the tank at the center (aligned with the impact point). Four additional string potentiometers measured the tank motions. The string potentiometers were attached to each of the tank skids and to the center of the tank heads at either end of the car. Fixed anchor positions were established so that these potentiometers measured the longitudinal motions of the tank head and skid.

Table 3 is a list of all string potentiometers inside and outside the tank car. Figure 10 and Figure 11 show their placement.

Table 3. Tank Car String Potentiometers

Area	Location	Axis	Channel Name	Range
Impact Area	B-End – 48-inch offset	Y	TD1Y	40 inches
Impact Area	B-End – 24-inch offset	Y	TD2Y	50 inches
Impact Area	Center	Y	TD3Y	50 inches
Impact Area	Center	Z	TD3Z	40 inches
Impact Area	A-End – 24-inch offset	Y	TD4Y	50 inches
Impact Area	A-End – 48-inch offset	Y	TD5Y	40 inches
Tank Head	A-End	Y	TDAend	50 inches
Tank Head	B-End	Y	TDBend	50 inches
Skid	A-End	Y	TDAskid	50 inches
Skid	B-End	Y	TDBskid	50 inches

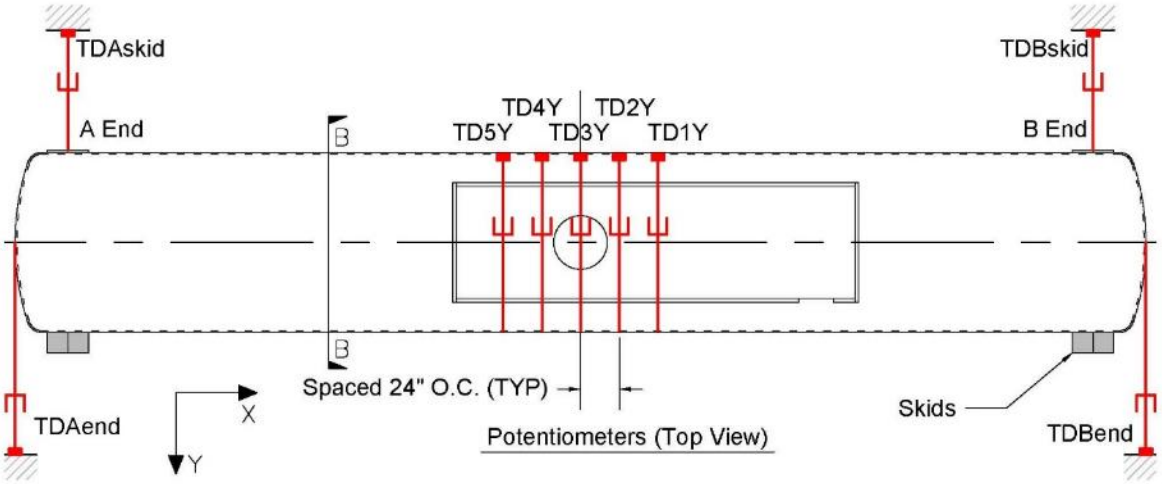

Figure 10. Tank Car String Potentiometers (top)

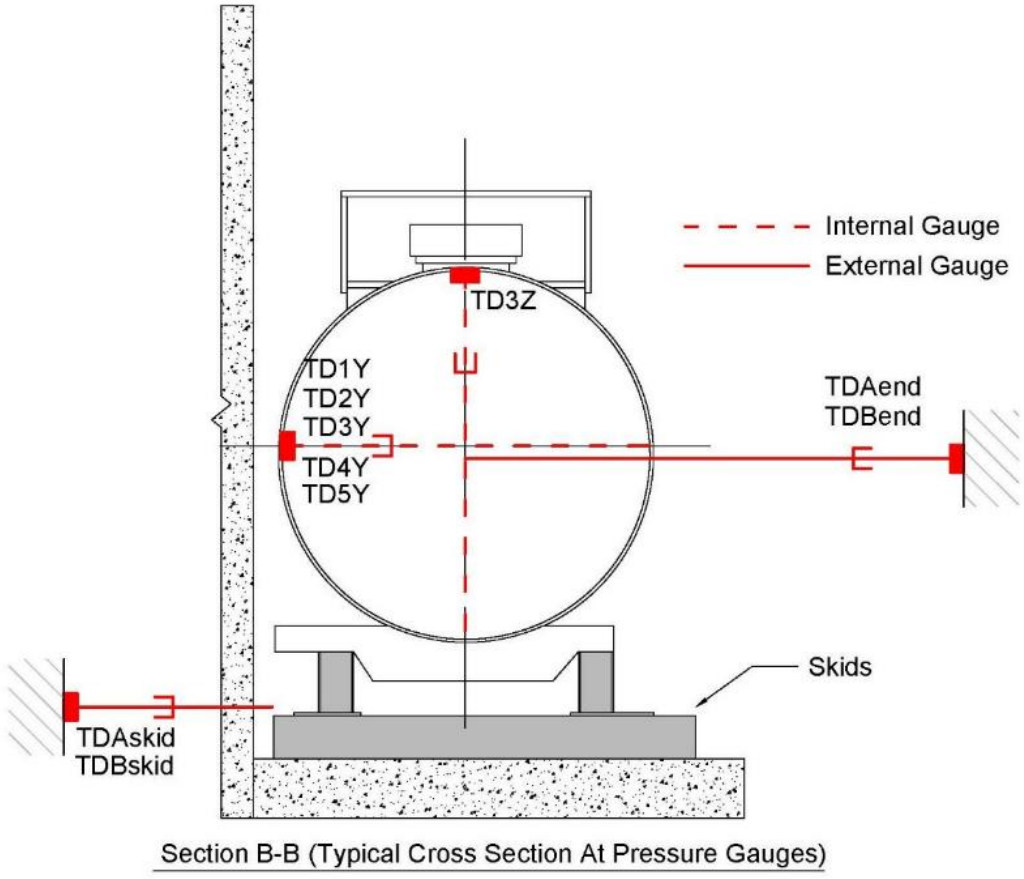

Figure 11. Tank Car String Potentiometers (side)

Two pressure transducers were mounted on the manhole, one on the pressure relief valve and one to measure pressure in the outage during the impact. In addition, an array of 11 pressure transducers were set up within the tank to record the pressure pulse through the lading. These were mounted in an array along the walls, bottom and top of the tank. The positions of the pressure transducers are shown in Figure 12 and Figure 13 and summarized in Table 4.

Table 4. Tank Car Pressure Transducers

Location	Channel Name	Sensor Description	Range
PR Valve	TPRV	Pressure Relief Valve	500 psi
B Top	TP1000	B-End Top Pressure	300 psi
B Back wall	TP1090	B-End Back Wall Pressure	300 psi
B Front wall	TP1270	B-End Front Wall Pressure	300 psi
B Floor	TP1180	B-End Floor Pressure	300 psi
M Top	TP2000	Mid-length Top Pressure	300 psi
M Back wall	TP2090	Mid-length Back Wall Pressure	300 psi
M Front wall	TP2270	Mid-length Front Wall Pressure	300 psi
M Floor	TP2180	Mid-length Floor Pressure	300 psi
C Back wall	TP3090	Center Back Wall Pressure	300 psi
C Floor	TP3180	Center Floor Pressure	300 psi
C Front wall	TP3270	Center Front Wall Pressure	300 psi
Manhole lid	TPMH	Outage Pressure	500 psi

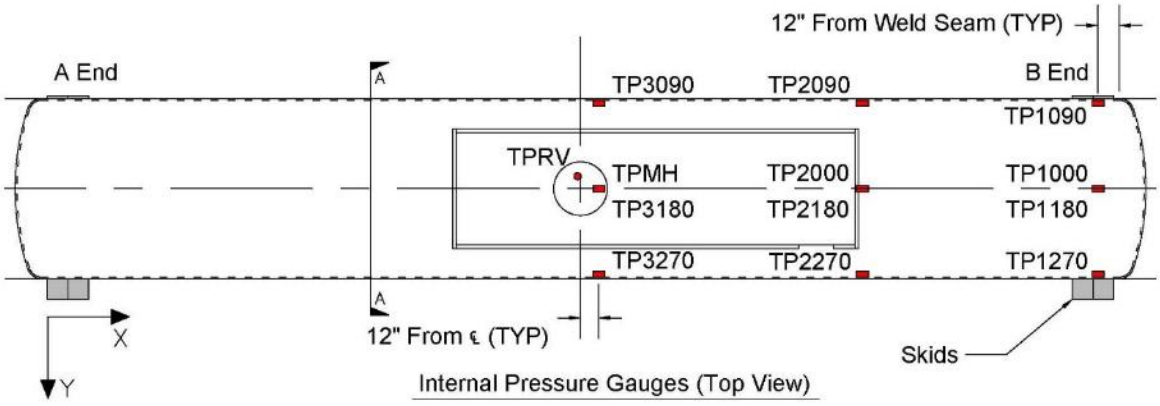

Figure 12. Tank Car Pressure Transducers (top)

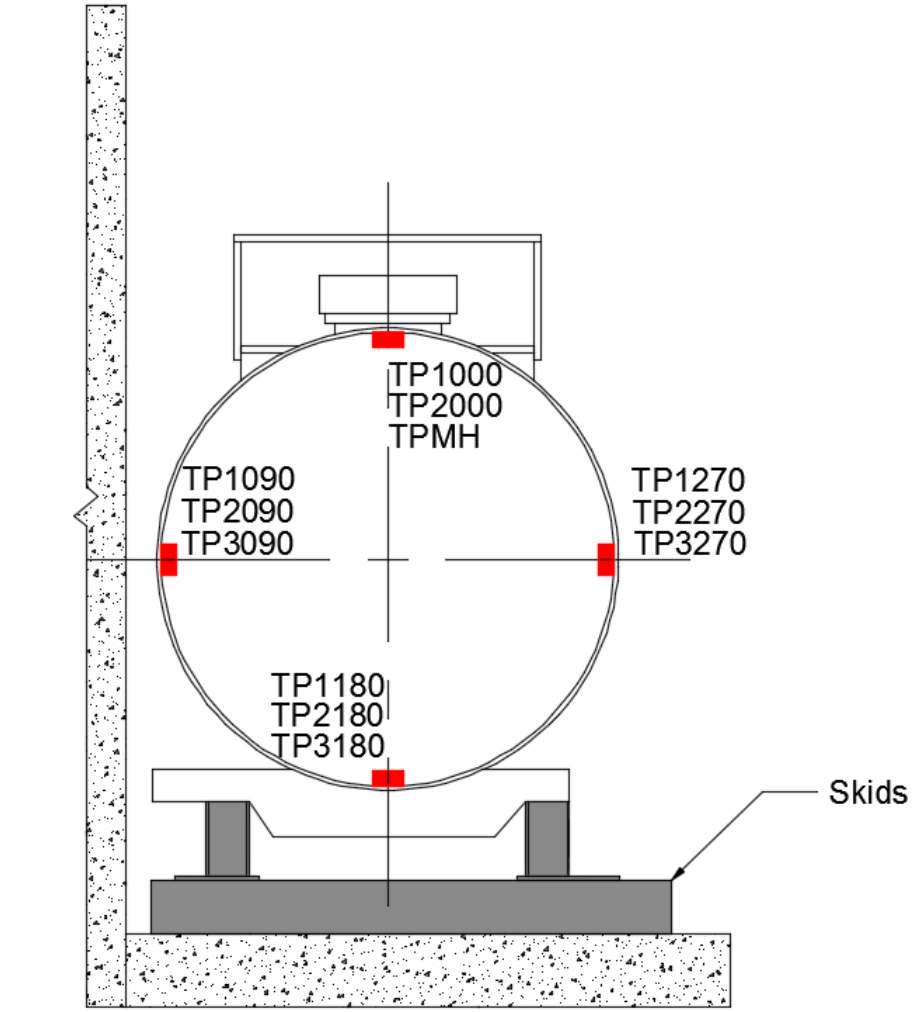

Figure 13. Tank Car Pressure Transducers (side)

3.4 Real Time and High-Speed Photography

Four high-speed and two real time high definition video cameras were used to document the impact event. Appendix A contains a schematic of the locations of the cameras and positions of the targets.

3.5 Data Acquisition

A set of 8-channel battery-powered onboard data acquisition systems was used to record the data from instrumentation mounted on the ram car. These systems provided excitation to the instrumentation, analog anti-aliasing filtering of the signals, analog-to-digital conversion, and recording of each data stream. A similar set of ground-based data acquisition systems was used to record data from the pressure transducers on the tank car.

The data acquisition systems were GMH Engineering Data BRICK Model III units. Data acquisition complied with the appropriate sections of SAE J211 (SAE International, 2007).

Data from each channel was anti-alias filtered at 1,735 Hz then sampled and recorded at 12,800 Hz. Data recorded on the data bricks was synchronized to time zero at initial impact. The time reference came from closure of the tape switches on the front of the test vehicle. Each data brick is ruggedized for shock loading up to at least 100 g. Onboard battery power was provided by GMH Engineering 1.7 Amp-hour 14.4 Volt NiCad Packs. Tape Switches, Inc., model 1201-131-A tape switches provided event initial contact.

Software in the data bricks was used to determine zero levels and calibration factors rather than relying on set gains and expecting no zero drift. The data bricks were set to record 1 second of data before initial impact and 4 seconds of data after initial impact.

4. Results

4.1 Test Conditions

As described in Sections 2.1 and 2.2, this test was a side impact on a DOT-105 tank car, performed on August 1, 2018. This test involved a 9.7 mph side impact by a structurally rigid 296,775-pound ram car with a 6-inch square impactor head into the side of the DOT-105. The tank car was backed by a rigid impact barrier. The actual impact speed of 9.7 mph was very close to the target test speed of 9.9 mph. The test tank car was filled to approximately 89.5 percent capacity with water to simulate standard commodity loading volume of a DOT-105 tank car and pressurized to 100 psi. At the time of the test, the ambient conditions included a wind speed of 4 mph, gusting to 15 mph from the southeast, and an air temperature of 76.1 °F. Prior to the test, the water within the tank had a measured temperature of approximately 75 °F.

4.2 Details of Test

Pre-test simulations estimated a failure speed between 9 and 11 mph. Section 6 discusses how researchers chose the target test speed using pre-test simulations.

Review of high-speed videos and test data revealed that the ram car was brought to a stop shortly after puncture, and it rebounded away from the tank after the impact until its brakes brought it to a stop. Figure 14 shows the impact from the point-of-view of the ram car at an instant just before puncture.

Figure 14. Deformed Tank Just Prior to Puncture

Figure 15 shows the damage to the tank car after impact. Through the tear in the jacket, the tear in the inner tank is also visible. The two parallel, horizontal dark lines on the inner tank indicate the imprint from the impactor's top and bottom edges.

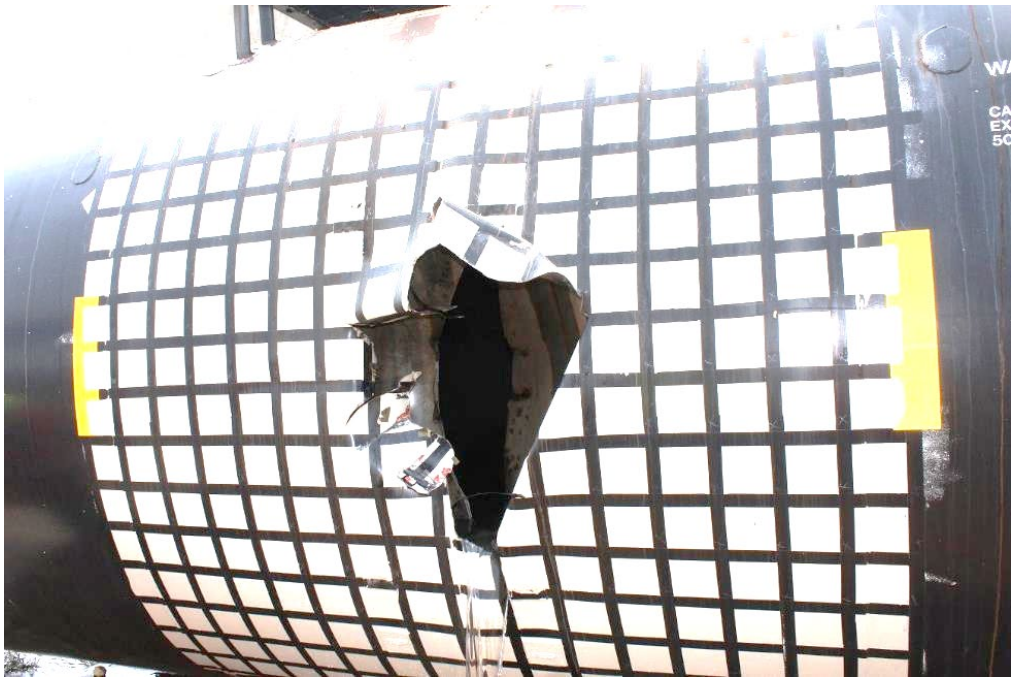

Figure 15. Tank Car—Post Impact (impact side)

The tank car recovered a portion of energy post-rupture, resulting in a slight rebound. Figure 16 shows the post-test position of the tank car relative to the supporting wall.

Figure 16. Tank Car—Post Impact (wall side)

4.3 Measured Data

This section contains a summary of key measurements from the test. Section 6 contains an overview of the comparison between pre-test FE calculations and the test measurements, while Section 7 contains an overview of the comparison between post-test FE calculations and the test measurements. The complete set of test measurements and finite element analysis (FEA)

comparisons is in Appendix C. The data collected during the test was processed (i.e., offset corrections, filtering, etc.) initially by TTCI and given to Volpe for comparison to analyses. The offset adjustment procedure ensured that the data plotted and analyzed contained only impact-related accelerations and strains. The offset adjustment excluded electronic offsets or steady biases in the data. To determine the necessary offset, the data collected before impact was averaged. This offset was then subtracted from the entire data set for each channel. This post-test offset adjustment was independent of, and in addition to, the pre-test offset adjustment made by the data acquisition system.

The post-test filtering of the data was accomplished with a phaseless four-pole digital filter algorithm consistent with the requirements of SAE J211 (SAE International, 2007). A 60 Hz channel frequency class (CFC) filter was applied for the filtered acceleration data shown in this report. A summary of the measured data is provided in this section. Appendix B contains the plots of filtered data from all transducers.

The longitudinal acceleration of the ram car was one of the primary measurements in the test. Multiple accelerometers were used on the ram car to capture this data. The ram car acceleration was used to derive the impact energy, deceleration of the ram car, and contact forces between the ram and target tank car. Figure 17 shows the ram car average longitudinal acceleration history from all the ram accelerometers.

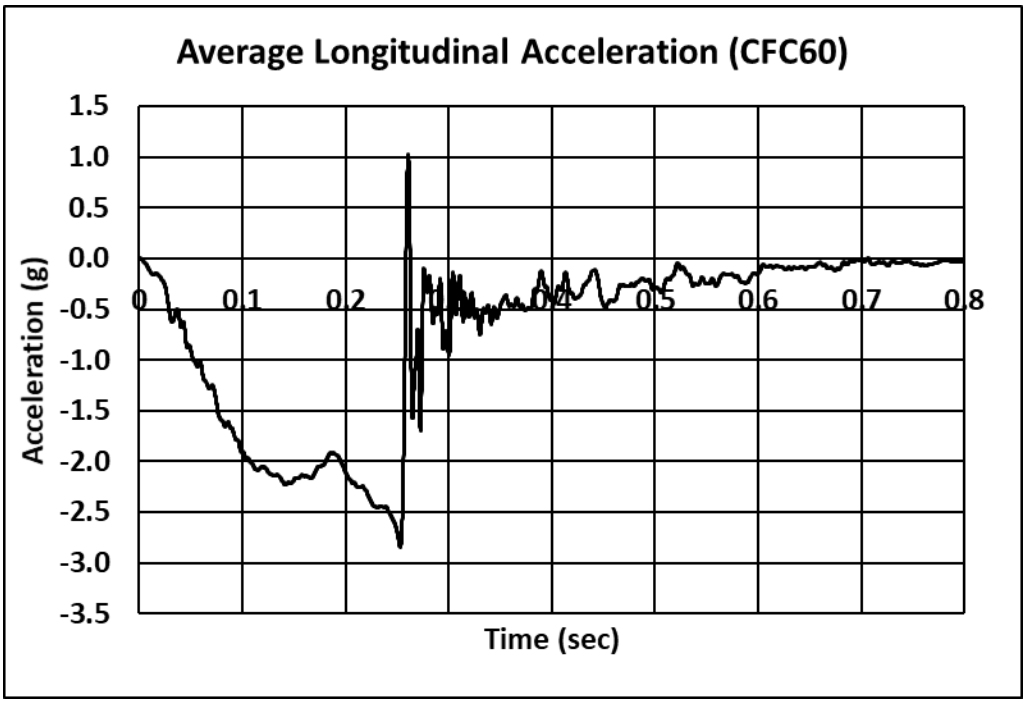

Figure 17. Longitudinal Acceleration Data (averaged)

The maximum measured deceleration was approximately 2.8 g. Deceleration dropped to zero approximately 0.26 seconds after the initial impact.

The ram car velocity history in the test was calculated by integrating the average longitudinal acceleration of the ram car and using the impact speed measurement as an initial condition. Contact forces between the ram car and target tank car were calculated as the product of the average acceleration and the mass of the ram car. Figure 18 shows the force-time and the

velocity-time histories. Negative velocity is the speed of the rebounding ram car. This data shows that the ram car was traveling at less than 1 mph at the time of the sudden force drop that corresponds to puncture.

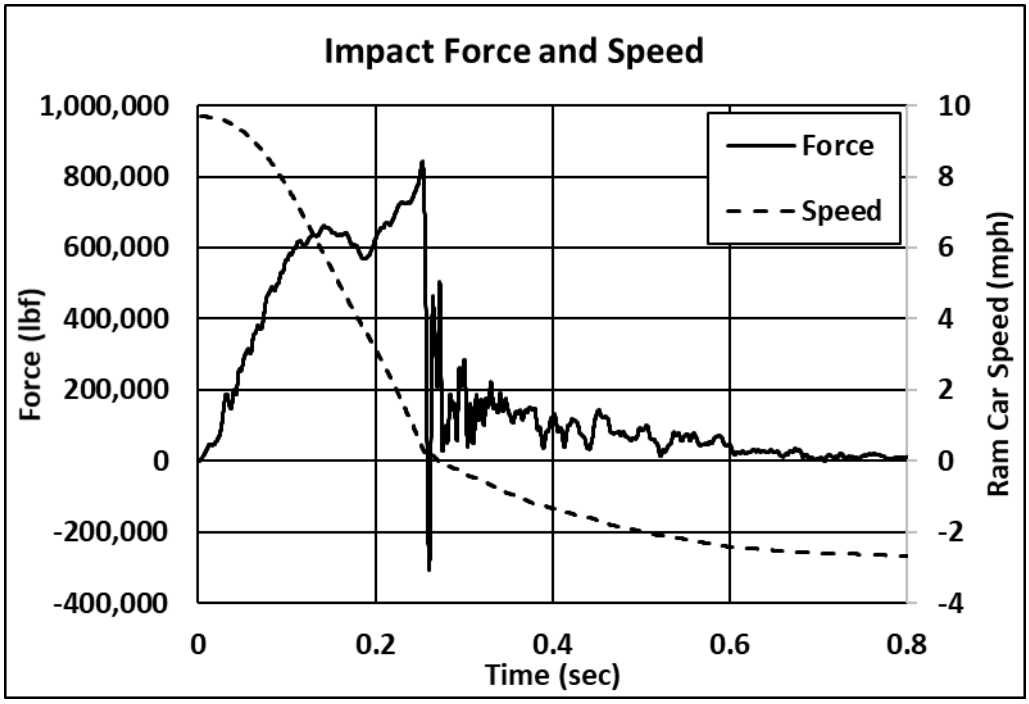

Figure 18. Impact Force and Ram Car Speed

Similarly, the kinetic energy was calculated for the ram car from its speed-time history and weight. Figure 19 shows the kinetic energy time history of the ram car and energy absorbed by the tank car. The energy absorbed by the tank car is capped at the time of the maximum force, when the puncture occurred, at approximately 0.26 seconds.

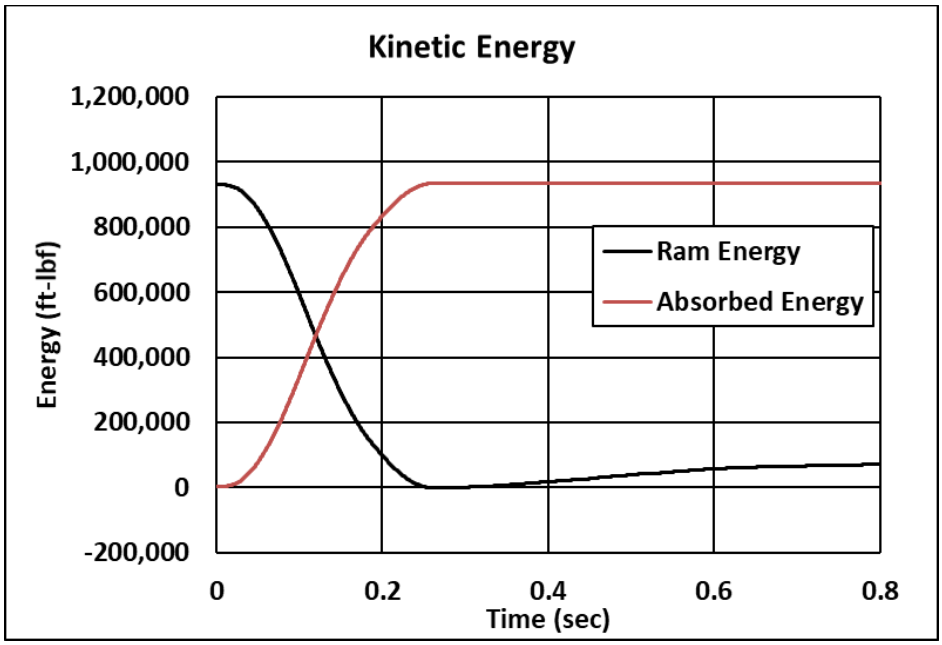

Figure 19. Kinetic Energy

The total kinetic energy of the ram car was approximately 933,000 ft-lbf and the energy absorbed by the tank car before puncture was 932,000 ft-lbf. The difference between the ram cars' kinetic energy and the energy absorbed by the tank before puncture was only 1,000 ft-lbf of residual energy, or only 0.2 percent of the total kinetic energy.

Another significant impact response measured in the test was the effects on the internal pressure as the indentation formed and reduced the volume of the tank. The tank was filled to approximately 10.5 percent outage volume with water, which can be approximated as incompressible for the impact behavior. Then the tank's outage (air space above the lading) was pressurized to 100 psi relative to atmospheric pressure. The gas volume in the outage was compressed as the dent formation reduced the tank's volume, causing the internal pressure to increase. As described in Section 3.3, the mounting of pressure transducers occurred at several locations in the tank, both within the water and at the pressure release valve within the air.

Figure 20 shows pressure data from transducers TP3090, TP3180, TP3270, and TPMH (Back Wall, Bottom, Front Wall, and Outage, respectively) located at the center of the tank car. The comparison of pressure data shows that the pressure was dominated by the average hydrostatic pressure developed from the denting and volume change up to the point of puncture. After the tank was punctured, there were additional dynamic pressures caused by the sloshing motions of the water in the tank that added local pressure variations that were up to approximately 70 psi different from the average value. The impact increased the hydrostatic pressure by approximately 15 psi, and the maximum pressure occurred at the time of puncture. It should be noted that the sudden, short duration pressure change observed in transducer TP3180 (labeled "bottom" in Figure 20) was not believed to be representative of any real event and was most likely a malfunction in the transducer. Furthermore, all data recorded after the pressure jump is consistent with the data recorded from the other pressure transducers.

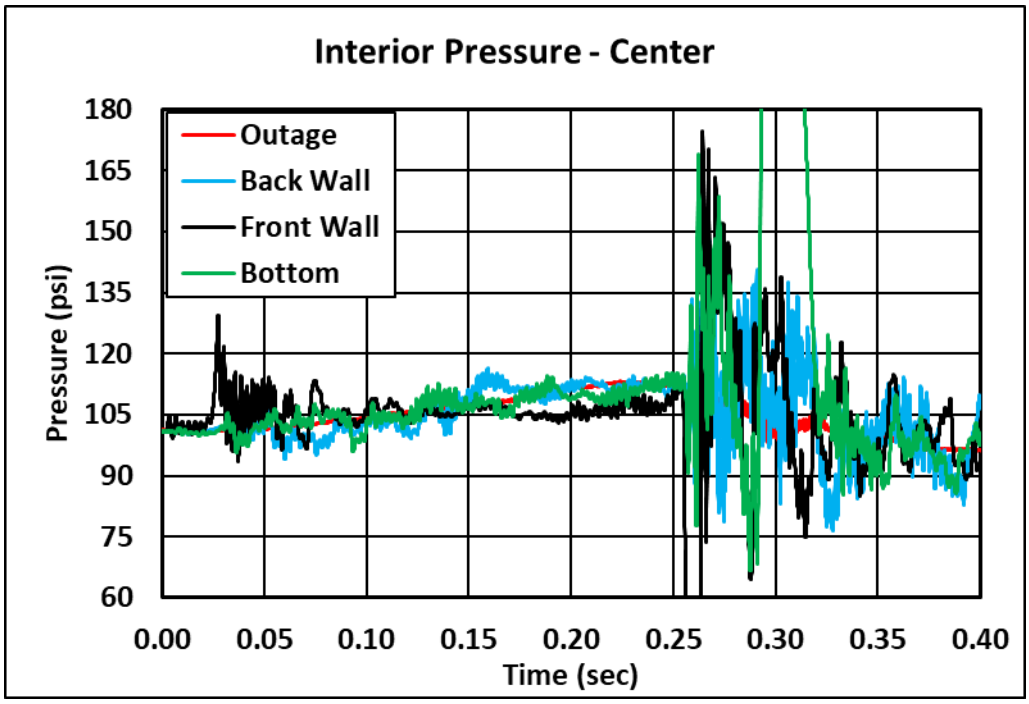

Figure 20. Pressure Data Measured at the Center of the Tank Car

The remaining quantitative measurements of the tank impact behavior were displacement histories recorded with string potentiometers. These included both internal tank deformations and external tank movements at both ends of the tank. Section 3.3 describes the layout of the string potentiometers.

Figure 21 shows the measured displacements for the horizontal tank internal string potentiometers (i.e., TD1Y through TD5Y). Overall, the data showed consistent measurements of the tank deflections, with the largest deflection at the impact location and reduced displacements at distances farther from the center of the impact. The displacements recorded by transducers TD1Y and TD5Y (B-end 48-inch offset and A-end 48-inch offset) are approximately the same. The displacements recorded by TD2Y and TD4Y (B-end 24-inch offset and A-end 24-inch offset) are noticeably different. TD2Y showed greater plastic deformation. The gages TD4Y and TD5Y (A-end 24-inch offset and A-end 48-inch offset) appeared to have experienced malfunctions, as the sharp spikes in the data are not consistent with a physical behavior. TD3Y (Center, Y-axis), appeared to have suffered damage during the impact and recorded an unrealistic permanent deformation of 24 inches. The maximum longitudinal compression of the tank should have occurred at around the same time as the puncture of the tank car (between 0.25 and 0.26 seconds). Additionally, the ram car was beginning to move backwards by approximately 0.3 seconds, making additional longitudinal compressive deformation extremely unlikely.

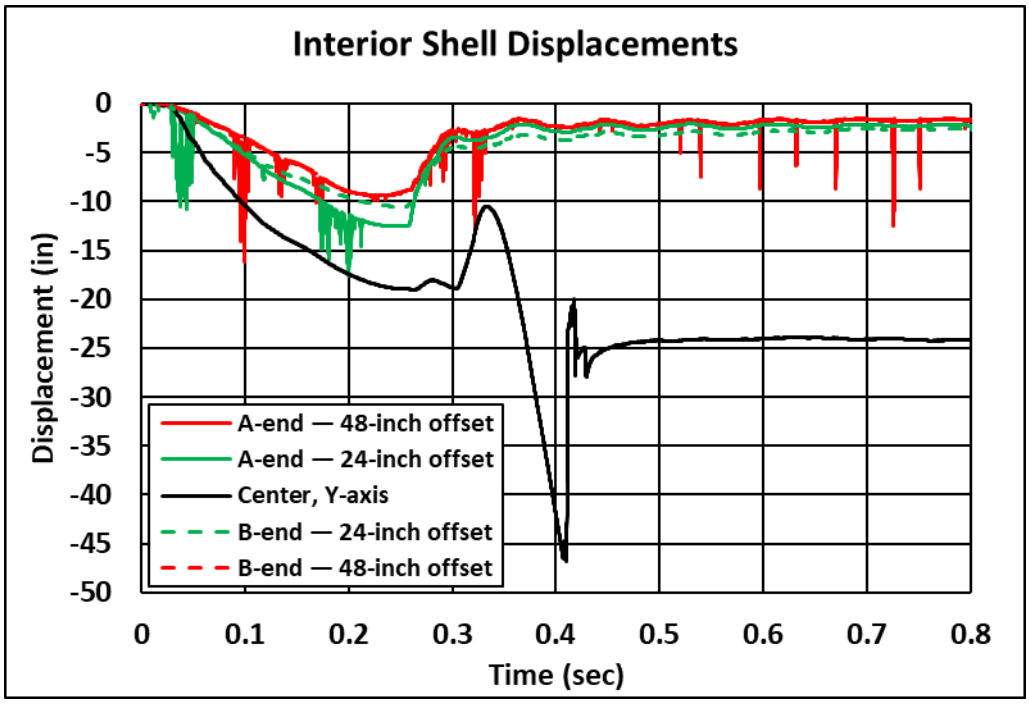

Figure 21. Internal Horizontal Displacements

Figure 22 shows vertical displacement of the shell inside the tank car at the mid-length cross-section. This channel indicates the car experienced a small amount of "ovalization" (increase in tank diameter at the top and bottom as a result of indentation on the side).

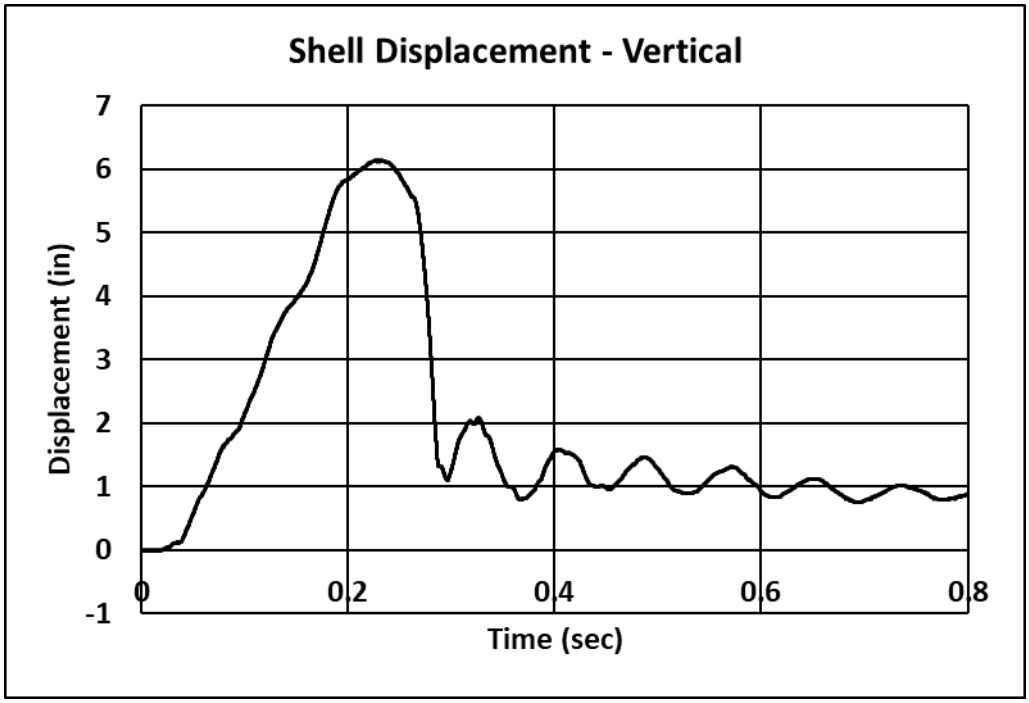

Figure 22. Internal Vertical Displacement

Figure 23 and Figure 24 show the measured displacements for the tank end external string potentiometers. The displacements of the car ends were delayed from the motions in the impact zone, and little displacement was seen for the first 60 milliseconds of the response. The measurements of the car end head displacements and the skid displacements were very similar. The response was symmetric between the A-end and B-end of the tank until approximately 0.12 seconds after impact. From that point, the A-end experienced a larger displacement than the B-end.

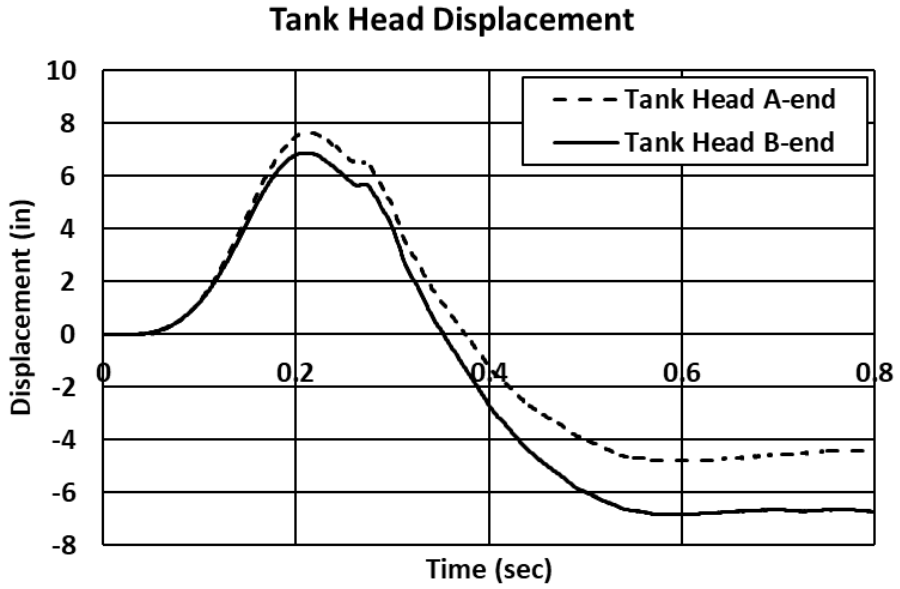

Figure 23. External Displacements–Tank Car Heads

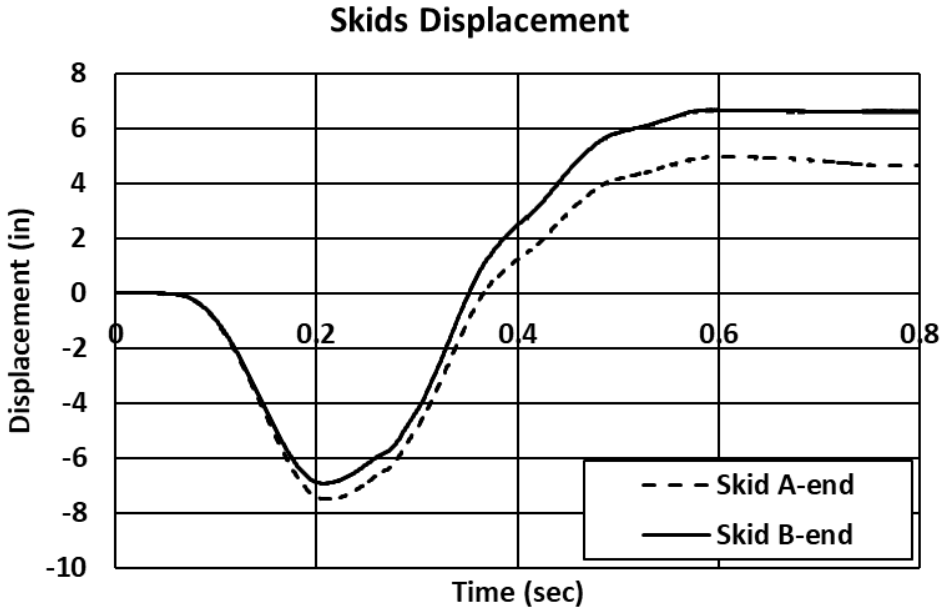

Figure 24. External Displacements—Skids

TTCI scanned an approximately 8-foot by 8-foot surface of the tank car in the impact zone before and after the impact test. Figure 25 shows a comparison of the cross-sections of the impact location

from the pre- and post-test scans aligned using reference points located on the tank car. The maximum permanent (plastic) deformation on the impact surface was approximately 17.7 inches. This is probably close to the maximum plastic longitudinal deformation incurred by the tank car. Visual inspection indicated additional deformation occurred on the side of the tank car that was facing the crash wall, but it was comparatively minor.

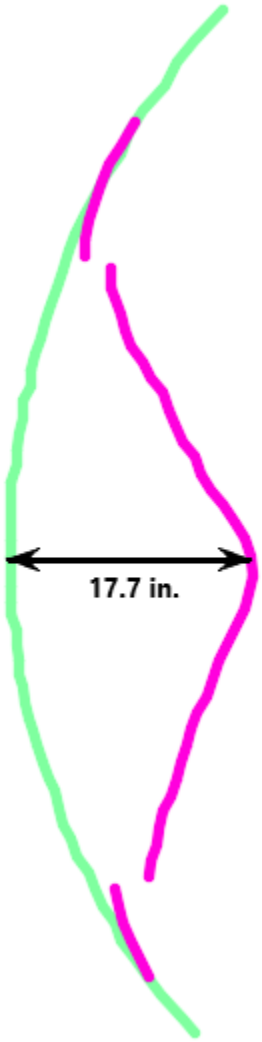

Figure 25. Scanned Geometry of Tank Car—Center Cross-Section

5. FE Model Development

Volpe personnel developed FE models of the DOT-105 tank car prior to the test to estimate the desired impact speed. These pre-test FE models provided estimates of the speed range where puncture could be expected to occur without knowing all the parameters, such as the exact material behavior in the tank car's shell. The FE models incorporated and expanded upon several techniques that had been used to simulate previous tank car impact tests (Kirkpatrick, S., Rakoczy, P., MacNeill, R. A., & Anderson, A, 2015) (Rakoczy, P., & Carolan, M, 2016) (Kirkpatrick, S. W, 2010) (Carolan, M. E., et al, 2013) (Yu, H., Jeong, D. Y., Gordon, J. E., & Tang, Y. H, 2007) (Tang, Y. H., Yu, H., Gordon, J. E., Jeong, D. Y., & Perlman, A. B, 2008) (Yu, H., Tang, Y.H. Gordon, J. E., & Jeong, D. Y, 2009) (Carolan, M., & Rakoczy, P., 2019) (Rakoczy, P., Carolan, M., Gorhum, T., & Eshraghi, S., 2019). The DOT-105 tank car FE model required definition of the tank car geometry, geometry of the impact setup (e.g., impact wall, impactor, etc.), definition of boundary conditions, initial conditions, and development of several material models. Additionally, modeling features such as element types, mesh sizes, and fluid/structure interactions were selected.

The FE models were developed using the Abaqus/CAE preprocessor and executed in Abaqus/Explicit (Dassault Systemes Simulia Corp, 2014). Abaqus/Explicit is a commercially available, general purpose nonlinear FE solver capable of simulating dynamic impacts involving complex material behaviors such as plasticity and puncture. The Abaqus software also includes several modeling techniques to represent the water and air phases of the lading, permitting these two parts to be modeled explicitly. The solid mechanics simulation features used in the DOT-105 FE model included modeling an elastic-plastic material response for the tank and jacket, ductile failure implementation of the Bao-Wierzbicki (B-W) triaxiality based damage initiation model (Bao, Y., & Wierzbicki, T., 2004).

In an ideal pre-test FE model, the actual material properties that include yield strength, ultimate strength, and plastic stress-strain response would be used as inputs to the model. Prior to this test, the tank car's material properties could not be known without excising coupons from the tank. Plastic stress-strain test data from two similar DOT-105 tank cars (Kirkpatrick, S. W, 2010) (Carolan, M., & Rakoczy, P., 2019) that were previously modeled in side impact tests were used to define the material input data in the pre-test FE model.

The choice of impact conditions for the test, and therefore the FE model, permitted comparison between this test and two previous DOT-105 tank car tests that took place on July 11, 2007, (Test 2) (Kirkpatrick, S. W, 2010) and April 27, 2016, (Test 6) (Carolan, M., & Rakoczy, P., 2019) respectively. All tests used the same ram car; however, it was equipped with a 6-inch by 6-inch impactor in Test 2 and a 12-inch by 12-inch impactor in Test 6.

The representation of the lading in the DOT-105 FE model used a hydraulic cavity technique for the water phase and a pneumatic cavity for the pressurized air phase. This approach is identical to what was used for the pre- and post-test FE models of Test 6, which used a companion DOT-105 tank car to the car used in this test (Carolan, M., & Rakoczy, P., 2019). In a previous side impact test of a DOT-112 tank car, Rakoczy et al. (2016) used a smoothed particle hydrodynamics (SPH) modeling approach to model the air phase and a Lagrangian (brick) formulation was used for the water phase. For a previous DOT-117 tank car test, Rakoczy et al. (2019) modeled the water phase using Lagrangian elements, and the air phase was modeled using a pneumatic cavity approach.

The pneumatic or hydraulic cavity approach is a simplified modeling technique that represents the fluid type (either gas or liquid, respectively) using an average pressure over the entire volume. This average pressure will change over the course of the impact simulation, as the volume enclosing the cavity is reduced through tank deformation. This dual-cavity approach to fluid modeling gave satisfactory representation of the fluid response seen in this test with a pressurized DOT-105 tank car, while offering considerable computational efficiency over an explicit representation of the liquid phase.

Following the test, researchers introduced several changes to the pre-test FE model to account for more accurate input conditions. An update took place of the material behaviors in the shell of the post-test FE model based on the results of tensile tests performed on the actual material of the tested car. The post-test FE model ran at the measured test speed of 9.7 mph, and an update of the ram car occurred from the estimated weight of 295,000 pounds to the measured weight of 296,775 pounds.

5.1 Overview of Models

The pre-test and post-test FE models were made up of: 1) geometry representing the components in the test setup, 2) material parameters describing the behavior of the materials making up the car and its lading, and 3) numerous constraints, boundary conditions, and loads describing the conditions of the test. As a part of both the pre-test and post-test modeling studies, researchers developed the non-puncture models along with puncture-capable models. Non-puncture models featured simplified material behaviors, where the tank and jacket featured only elastic-plastic material responses without ductile failure behaviors. The material definitions were incapable of simulating puncture, so coarser meshes were used on the non-puncture models in the impact zone in the interest of reducing model runtime. The non-puncture models were useful for investigating the overall response of the DOT-105 model prior to puncture, before implementing any new behavior in the more complex and time-intensive puncture-capable models.

Puncture-capable models featured more complex material definitions, capable of simulating element degradation and removal, and refined meshes on the tank and jacket in the areas of contact with the impactor. The refined area of the tank was meshed using solid elements, while the much thinner jacket featured a refined shell mesh. All FE results obtained in this report used models capable of simulating puncture.

All FE models (i.e., pre-test, post-test, puncture-capable, and non-puncture) used a half-symmetric condition, with a vertical-longitudinal symmetry plane at the centerline of the tank car to reduce the size of the model. The tank geometry was simplified, and structures such as the bolster were omitted. These simplifications have a relatively minor effect on the impact response of the tank under the test conditions. Figure 26 shows the pre-test FE model.

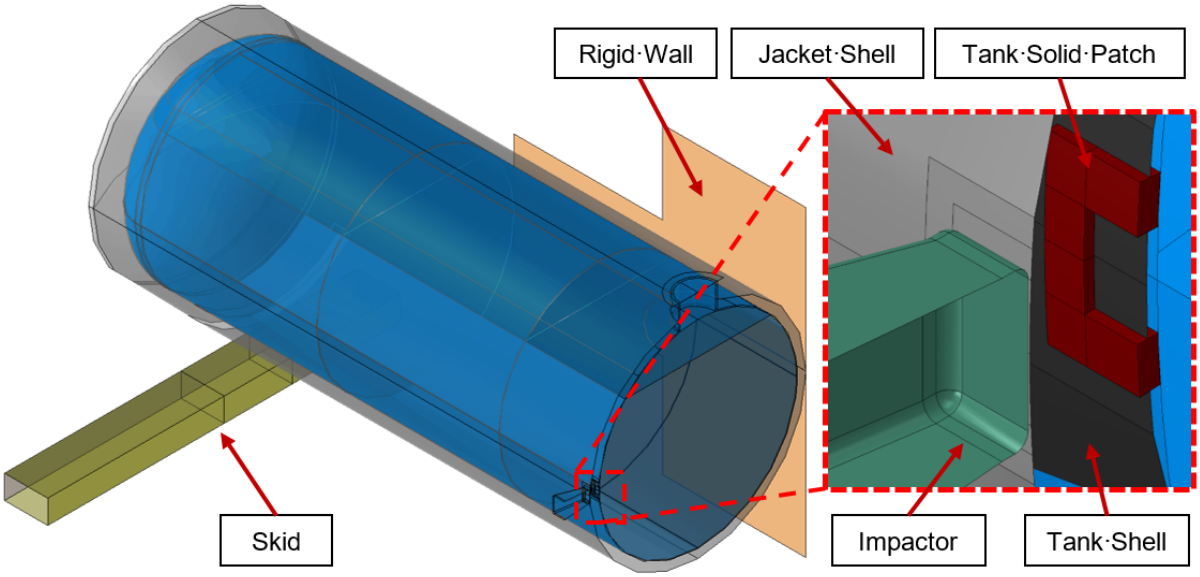

Figure 26. Annotated Pre-test FE Model (insulation hidden)

The parts included in the FE model can generally be divided into three categories: rigid bodies, deformable bodies made of steel, and deformable bodies made of other materials. Since the model was half-symmetric, the part weights in the FE model generally correspond to half the weight of the actual tested geometry. The exception to this is the skid, as the skid exists entirely to one side of the symmetry plane. Therefore, the full weight of one skid is included in the model, and in the actual test the DOT-105 tank car is attached to two skids.

Table 5 summarizes the parts making up the FE model used in the pre-test puncture simulations. This table contains the weight of the part in the model, as well as the weight of the full part (i.e., twice the model weight) for applicable parts. Due to adjustments made between this model and the post-test models, the meshes and part weights were slightly different in the post-test models. Appendix D provides a full description of each part in the pre-test and post-test FE models.

From Table 5, the total weight of the parts in the FE model corresponding to the entire DOT-105 tank car, which is twice the weight in the half-symmetric model, is approximately 210,000 pounds. The single heaviest part in both the FE model and the test setup is the water within the tank car. The use of water in the test accounted for both the mass and the dynamic effects of a fluid-filled tank car. However, the DOT-105 tank car would typically be used to carry liquefied compressed gases under pressure or other low-pressure, high-hazard materials. As it is neither safe nor practical to run an impact test using a typical DOT-105 tank car commodity such as chlorine, water is used as an analogue and the tank car is pressurized with air. The effect of using water in lieu of the commodity for which the tank car has been designed is that the as-tested car is lighter than an in-service car filled to the same level.

Table 5. Summary of Parts in FE Models

	Part Name	Elements No.	Symmetric Model Mass lbf s²/in	Symmetric Model Weight lbf	Full Size Mass lbf s²/in	Full Size Weight lbf
Rigid Body	Impactor	2,007	381.89	147,443	763.78	294,887
Rigid Body	Rigid Wall	442	-	-	-	-
Rigid Body	One Skid	360	29.06	11,220	29.06	11,220
Deformable, Steel	Jacket	16,442	8.60	3,320	17.20	6,641
Deformable, Steel	Tank (Shell Elements)	7,964	50.24	19,397	100.48	38,794
Deformable, Steel	Tank (Solid Elements)	23,760	0.00998	3.85	0.01996	7.71
Deformable, Non-steel	Membrane	9,560	183.07	69,620	366.14	141,362
Deformable, Non-steel	Foam Insulation	44,498	1.09	421	2.18	842

5.2 Material Behaviors in FE Models

Researchers used five material definitions in both the pre-test and post-test FE models without adjustment: A1011 steel, an internal membrane, air, water, and foam insulation. The model for a sixth material, Association of American Railroads (AAR) TC128 Grade B (TC128) steel, was different in the pre-test and post-test models. The material properties input to the FE models are summarized in this section. Appendix F contains complete descriptions of the development of the A1011, foam insulation, and TC128 steel characterizations.

5.2.1 Membrane

As described in Appendix D7, an artificial surface was modeled within the tank to define the limits of the hydraulic and pneumatic cavities. Because this surface does not correspond to any physical structure within the tank, modeling techniques were chosen to minimize the increase in either mass or stiffness introduced into the model by the membrane. The membrane material was modeled as having the same mass density of steel to avoid the minimum time increment becoming dominated by the artificial material in the membrane. Table 6 summarizes the material properties of the membrane.

Table 6. Material Properties Defined for Membrane Material

Parameter	Value
Density	7.35×10^{-4} lbf·s^2/in^4
Modulus of Elasticity	3×10^4 psi

Additionally, a nonstructural mass was added to the membrane around the hydraulic cavity to account for the mass of the water within the tank. Appendix D further describes this nonstructural mass.

5.2.2 Water

The target initial conditions for the side impact test of the DOT-105 tank car were set to a normal service outage of 10.6 percent and internal pressure of 100 psi. These initial conditions are identical to previous target conditions used in side impact tests with DOT-105 tank cars identified as Test 2 (Kirkpatrick, S. W, 2010) and Test 6 (Carolan, M., & Rakoczy, P., 2019). The liquid phase of the lading was modeled as water at approximately 70 °F (294.261 Kelvin) with property values previously defined in a side impact tank car model modeling a DOT-117 tank car (Rakoczy, P., Carolan, M., Gorhum, T., & Eshraghi, S., 2019). The use of a hydraulic cavity model within Abaqus described the behavior of the liquid water. The key material properties that must be input to this material model are the material's density and its bulk modulus. Values for density and speed of sound were obtained by interpolating published tabular values to the anticipated test temperature of 70 °F. Appendix E discusses further initial conditions.

The speed of sound (c) of a fluid can be determined from the fluid's bulk modulus (K) and density (ρ) according to the Newton-Laplace equation (Smits, 2000) given in Equation 1.

Equation 1. Calculation of Bulk Modulus

$$K = c^2 \rho$$

Table 7 shows the properties used in the DOT-105 tank car model. It includes both nominal units and the specific units used in the unit system of the FE model.

Table 7. Properties of Water Used in FE Models

Property	Value	Reference
Mass Density (ρ) *lbf·s²/in⁴*	9.41325×10^{-5}	(Engineering ToolBox, 2003)
Speed of Sound (c) *in/s*	57,553	(Engineering ToolBox, 2004)
Bulk Modulus (K) *lbf/in²*	311,797	

While density is among the parameters defined for the water in the hydraulic cavity, this value of density is only used by the solver to calculate the bulk modulus of the liquid in the hydraulic cavity. The representation of mass of the water in the tank was a distributed, nonstructural mass assigned to the membrane surrounding the hydraulic cavity. Appendix D describes further this nonstructural mass.

5.2.3 Air

The gas phase of the lading was modeled as air at a gauge pressure of 100 psi, as this was the desired internal pressure for the tank car at the beginning of the test. Within Abaqus, the air within the outage was modeled as an ideal gas, using a pneumatic cavity modeling technique. This modeling technique requires a surface to be defined that encloses the cavity, with a reference point defined within this cavity to which initial temperature and pressure can be assigned. Appendix E7 discusses further the initial pressure and temperature.

The pneumatic cavity approach models the entire cavity with a single average pressure and average temperature value, each of which can vary with time. Thus, by using this technique, the air pressure within the model can change as the volume of the tank changes due to the impact. Table 8 summarizes the modeling inputs defined for the air phase of the model.

Table 8. Properties for Air

Property	Value in Pre- and Post-Test Model	Reference
Universal Gas Constant (R) *in-lbf/(mol·K)*	73.583	(Engineering ToolBox, 2004)
Molecular Weight (MW) *(lbf·s²/in)/mol*	1.654×10^{-4}	(Engineering ToolBox, 2004)

Equation 2 shows the calculation of the molar specific heat capacity for air.

Equation 2. Calculation of Molar Specific Heat

$$c_{P.m} = c_P \cdot MW$$

Values for the specific heat capacity of air (C_p) were obtained from Urieli (2008). Table 9 shows the calculated values for molar specific heat at different temperatures defined as inputs to the FE models in the unit system used in the FE models.

Table 9. Molar Specific Heat for Air

Temperature *K*	$c_{P.m}$ *in-lbf/(mol·K)*
250	257.2
300	257.7
350	258.5
400	259.7

5.2.4 Foam Insulation

The DOT-105 tank car has roughly 4 inches of insulation between the tank car shell and jacket. Carolan & Rakoczy (2019) observed this in a previous side impact test (Test 6) with a companion DOT-105 tank car, while noting that modeling the area between the shell and jacket as a gap was not sufficient to accurately represent the force time history of the impactor. As a result of this observation, the authors developed a simplified foam material model for the Test 6 post-test model. The same foam material model was used in pre-test simulations for the current test (Test 8). Appendix F5 contains a thorough description of the development of the foam material model. Table 10 summarizes the material properties.

Table 10. Mechanical Properties of Foam Insulation

Property	Value
Density	3×10^{-6} lbf·s^2/in^4
Modulus of Elasticity	941.5 psi
Plasticity	Piecewise nonlinear (see Appendix F5)
Plastic Strain-to-failure	0.55

Material coupon testing was not conducted on the foam insulation. The material behavior described in this section is based on qualitative observations from Test 6 (Carolan, M., & Rakoczy, P., 2019).

5.2.5 ASTM A1011 Steel

The outer jacket was made of American Society for Testing and Materials (ASTM) A1011 steel for the tested DOT-105 tank car. The material properties defined for the A1011 material were derived from previous tests (Kirkpatrick, S. W, 2010). Appendix F3 contains a full description of the development of the material parameters. Table 11 summarizes these parameters.

Table 11. Summary of Material Parameters for A1011 Steel

Parameter	Value
Modulus of Elasticity	3×10^7 psi
Plasticity	Piecewise nonlinear (see Appendix F3)
Poisson's Ratio	0.3
Mass Density	7.35×10^{-4} lbf·s^2/in.^{4}
Damage Initiation	B-W Envelope (see Appendix F3)
Damage Progression	Linear, 1,500 in-lbf/in.^{2}
Mesh Implementation	0.04-inch Fully Integrated Shell (S4) Elements

5.2.6 AAR TC128 Grade B Steel

The construction of the 0.775-inch shell of the DOT-105 tank car was of AAR TC128 Grade B steel. One purpose of this test was to subject the tank car to a moderately high-speed impact that was close to the threshold speed between a puncture and a non-puncture test. It was known from the certificate of construction that the tank was manufactured from TC128 steel between 1979 and 1980, but the actual stress-strain response of the steel making up the car's shell was not known. Table 12 shows the minimum mechanical properties of TC128 (Association of American Railroads, 1978) that were required at the time of the car's construction.

Table 12. Minimum Properties for TC128

Property	Value
Yield Strength	50,000 psi
Ultimate Tensile Strength	81,000 psi
Elongation at Failure	22% (2-inch gauge)
Elongation at Failure	16% (8-inch gauge)

Table 13 summarizes the material models developed for the two definitions of TC128 in the pre-test models and the post-test material model that was calibrated from tensile coupons cut after the test actual.

Table 13. Summary of Material Parameters for TC128 Steels

Property	Value
Modulus of Elasticity	3×10^7 psi
Plasticity	Piecewise nonlinear (see Appendix F4)
Poisson's Ratio	0.3
Mass Density	7.35×10^{-4} lbf·s^2/in^4
Damage Initiation	B-W envelopes (see Appendix F4)
Damage Progression	Energy-based damage evolution (see Appendix F4)

Property	Value
Mesh Implementation	0.085-inch fully integrated brick (C3D8) elements (9 elements through 0.775-inch tank shell)

The process of developing the plastic stress-strain response in the format required by Abaqus, and the process of developing the ductile failure initiation and progression parameters are discussed in Appendix F4.

One purpose of the pre-test models was to provide an estimate of the speed range where puncture could be expected to occur. Two TC128 material response characteristics were selected for pre-test puncture modeling, using previous material characterizations of TC128 samples from similar DOT-105 tank cars. These characteristics were intended to represent a material that slightly exceeded the minimum ductility requirement for TC128 (as seen in Test 6 from Carolan & Rakoczy [2019]), and to represent a TC128 sample that greatly exceeded the ductility requirement (as seen in Test 2 from Kirkpatrick [2010]). The expectation was that by modeling the most- and least-ductile TC128 materials for which tensile coupon test data were available, the pre-test model would bound the expected range of speeds necessary to puncture the tank. After the test, tensile testing coupons were cut from the tank car and characterized. The actual post-test material behavior is compared with the estimated pre-test TC128 behavior in this section.

Detailed descriptions of: (1) how researchers selected the pre-test materials as candidates for pre-test material responses, (2) the process for calibrating the post-test material parameters in Abaqus/Explicit, (3) and results from simulations of pre-test and post-test tensile coupons are all contained in Appendix F4.

The results of FE simulations of 2-inch gauge length tensile coupons using the previously calibrated pre-test material models (Test 2 and Test 6) are plotted alongside the FE results from the newly calibrated post-test (Test 8) material in Figure 27.

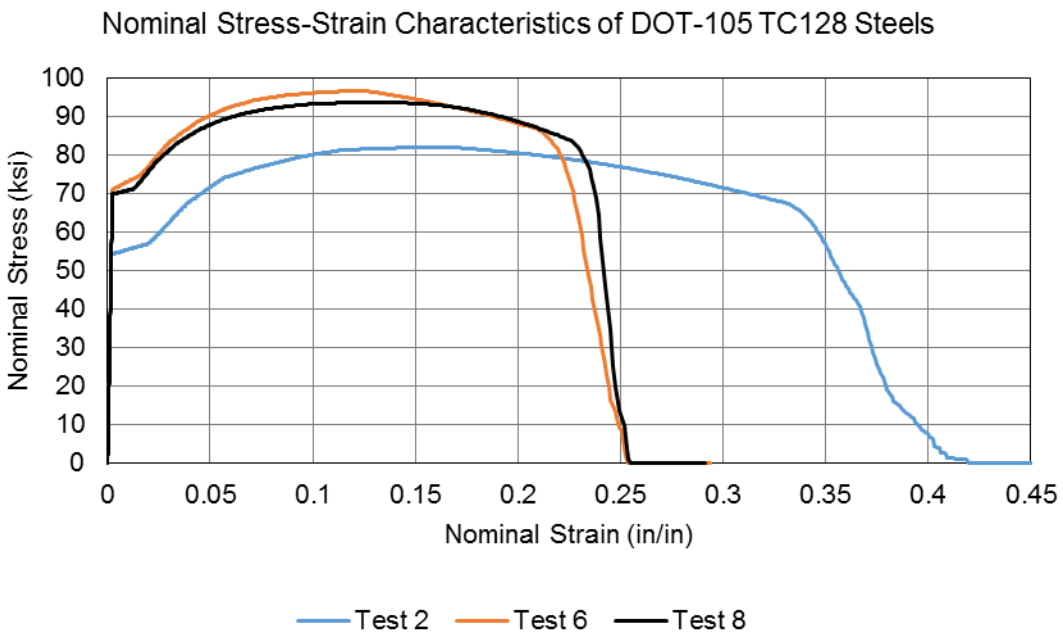

Figure 27. TC128 Nominal Stress-Strain Characteristics in Pre-Test (Test 2 and 6) and Post-Test (Test 8) Coupon Models

Figure 27 shows that the Test 8 TC128 nominal stress-strain characteristic was similar to the stress-strain characteristic from the Test 6 TC128. This was expected given that the tank cars were made by the same manufacturer at approximately the same time as indicated by the certificates of construction and car numbers. The methodology used for simulating the tensile coupon tests is detailed in Appendix F2.

In addition to requiring plastic stress-strain responses, the FE models used to simulate puncture required damage initiation envelopes and damage progression behaviors. The damage initiation envelopes that had been developed for the Test 2 and Test 6 FE models were used for pre-test simulations and are plotted alongside the envelope for the post-test model (Test 8) in Figure 28. As is discussed in Appendix F4, both Test 6 and Test 8 used the quick calibration procedure developed by Lee & Wierzbicki (2004) and Lee (2005). The resulting damage initiation envelopes for Test 6 and Test 8 TC128 were similar as expected due to the similarities between the tank cars, and the similar stress-strain behavior measured during the coupon tests. The Test 2 pre-test TC128 material was calibrated using a different approach, the details of which are provided in the Test 2 report (Kirkpatrick, S. W, 2010).

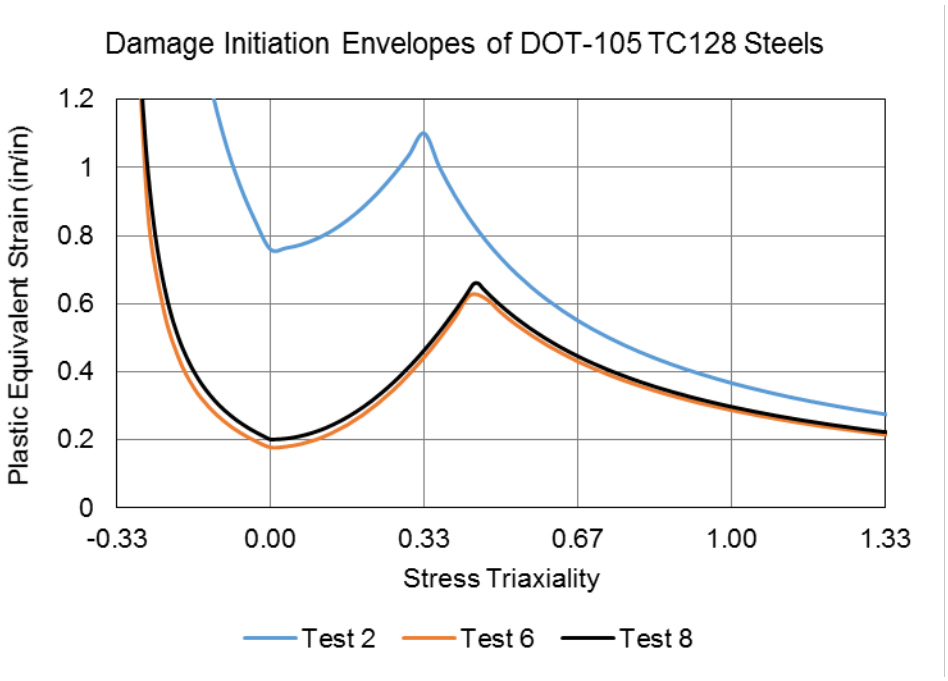

Figure 28. TC128 Ductile Damage Initiation Envelopes in Pre-Test and Post-Test FE Models

6. Comparison of Test Response to Pre-Test Analyses

Pre-test FE modeling was used to estimate the overall response of the tank to the impact, including the force-displacement response, as well as to estimate the expected range of puncture speeds on the basis of different TC128 steel properties. For each TC128 material used in the pre-test FE models, the simulated impact speed was varied in an iterative manner to attempt to estimate a puncture speed range within 0.5 mph. If a given combination of impact speed and material behavior resulted in puncture, then the model's speed was reduced and the model re-run. If the model did not puncture, then the impact speed was increased and the model re-run. This process was used for both pre-test TC128 steels.

The results of the pre-test modeling are summarized in Table 14, and more completely described in Appendix C1. Table 14 contains four results: the highest speed for which the model estimated a non-puncture outcome and the lowest speed for which the model estimated a puncture outcome for each of the two pre-test material behaviors. Based on these results, and assuming that the two selected materials do indeed bound the limits of material responses likely to be encountered during the test, these results indicate that for an impact speed below 8.5 mph, the tank would not be expected to puncture, regardless of the actual material response. Beginning at 8.5 mph, the likelihood of puncture increases with increasing impact speed. For speeds beyond 11 mph, puncture would be a very likely outcome regardless of the actual material response. The estimated puncture speed range is illustrated in Figure 29, with the actual impact speed of 9.7 mph indicated.

Table 14. Summary of Pre-Test FE Model Results

TC128 Sample Source	Highest Speed Without Puncture	Lowest Speed with Puncture
Test 2 DOT-105 Tank Car	10.5 mph	11 mph
Test 6 DOT-105 Tank Car	8.5 mph	9 mph

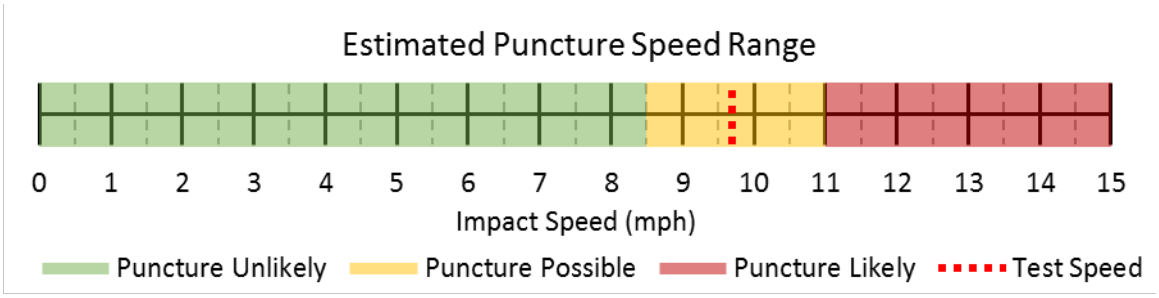

Figure 29. Estimated Puncture Speed Range from Pre-Test FEA

A target test speed of 9.9 mph was chosen to be within the range where puncture was a likely outcome, but not a certain outcome. Based on previous tank car tests, the test speed was expected to be within a +/-0.5 mph band around the target test speed. Thus, the anticipated range of impact

speeds was 9.4 to 10.4 mph. The measured test speed, as determined from speed traps, was 9.7 mph.

6.1 Pre-Test Impactor Force Results

Pre-test FE models using both the Test 2 and Test 6 calibrated TC128 material models were run at the measured test speed of 9.7 mph. Figure 30 compares the force-versus-displacement results from those models to the test results. In the test, the mass of the impactor is multiplied by the average deceleration from the five longitudinal accelerometers to obtain impact force. In the FE models, the acceleration is calculated at a single reference point on the impactor, since the impactor is modeled as a rigid body. Therefore, the impact forces in the FE models are simply the product of impactor mass and acceleration. A CFC60 filter has been applied to the FEA and test acceleration data in accordance with SAE J211 (SAE International, 2007).

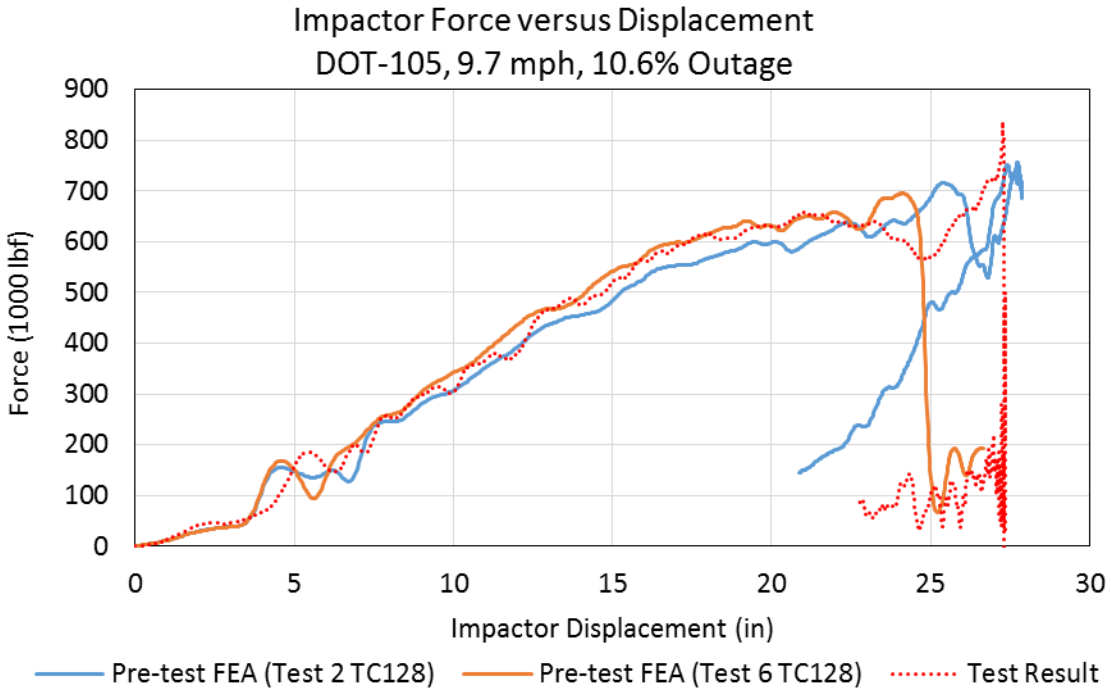

Figure 30. Force-displacement Responses from Pre-Test FEA Compared with Test Results

Both pre-test responses show a similar shape as the test measurements. The models do a good job of capturing the overall response of the test, including the changes-in-slope of the response as the impactor deforms the tank car and pushes it back against the wall. The pre-test simulation using the high-ductility Test 2 TC128 material model did not experience a puncture at the measured speed of 9.7 mph, and thus the impactor can be seen to rebound in this figure. The pre-test simulation using the low-ductility Test 6 TC128 material model estimated a puncture; thus, the impactor forced dropped out and a rebound was not observed. The test data shows a dip in force after approximately 24 inches of impactor travel before the force peaks at the maximum displacement. The pre-test FE models were able to bound the impactor displacement, but the peak force was not bounded and was slightly underestimated.

Pre-test simulation using the Test 2 and Test 6 TC128 calibrated material models were successful at bounding the residual speed of the impactor in the test, as Figure 31 shows. The residual speed is defined as the speed when the impactor force drops out. This force dropout occurs at approximately the time of puncture of the tank car shell, as the resistance offered by the tank car suddenly decreases. The pre-test simulation using the Test 2 material model rebounded with a velocity of approximately 5 mph. The pre-test simulation using the Test 6 material model punctured the shell of the DOT-105 tank car after slowing to a speed of approximately 3.5 mph. The actual test punctured after the ram car slowed to a speed of less than 1 mph, which is considered an excellent test outcome as there are many difficult-to-control variables during a side impact test. Further details regarding the difficulty in predicting the puncture speed in side impacts of tank cars are explained in Section 1.4.

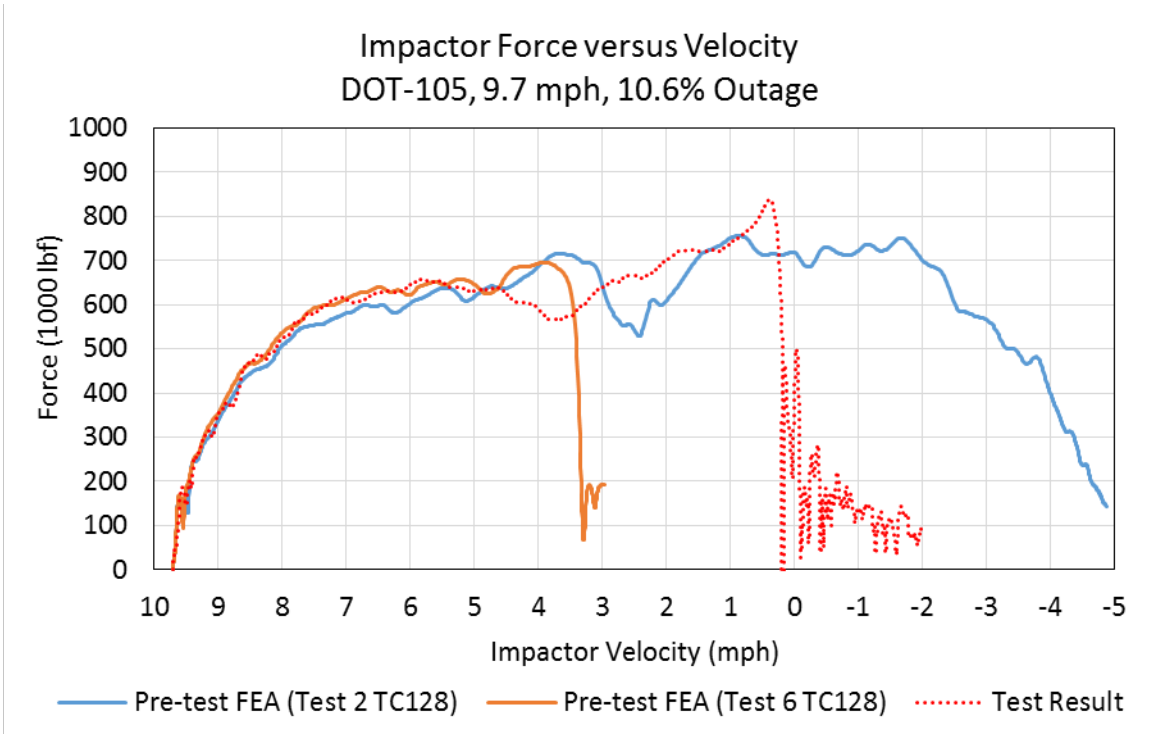

Figure 31. Impactor Force versus Velocity Responses from Pre-Test FEA Compared with Test Results

6.2 Pre-Test Air Pressure Results

Figure 32 shows a comparison plot of the average air pressure in the pre-test analyses compared to the test data. For each FE result, the average pressure in the outage is reported. For the test data, the air pressure measured by the gauge in the manway is plotted. Both pre-test FE models captured the shape of the pressure-time response measured in the test, though the models both underestimate the maximum pressure measured in the test. This underestimate is likely due to the pneumatic cavity only representing the average air pressure over the full outage volume, while in the actual tank the pressure can vary with both time and location within the tank.

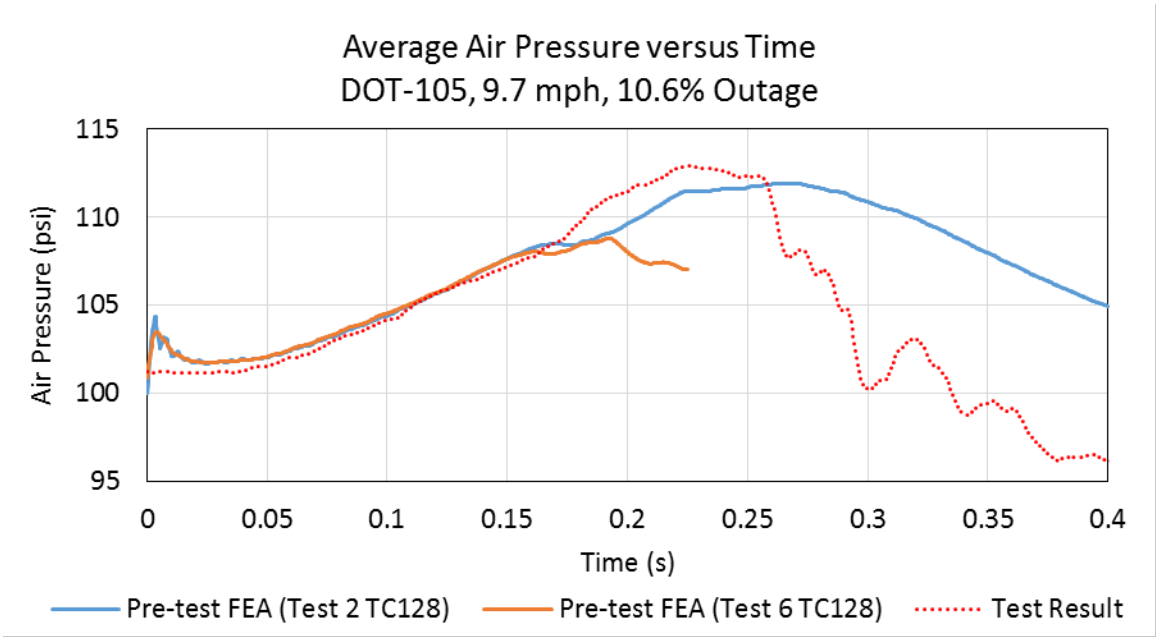

Figure 32. Air Pressure-time Responses from Pre-Test FEA Compared to Test Results

6.3 Pre-Test String Potentiometer Results

Figure 33 contains a plot comparing the internal string potentiometer measurement at the center of the car against the pre-test FE model results. In both pre-test FE models, the model captured the general shape of the test response quite well up to the point where puncture occurred at approximately 0.26 seconds.

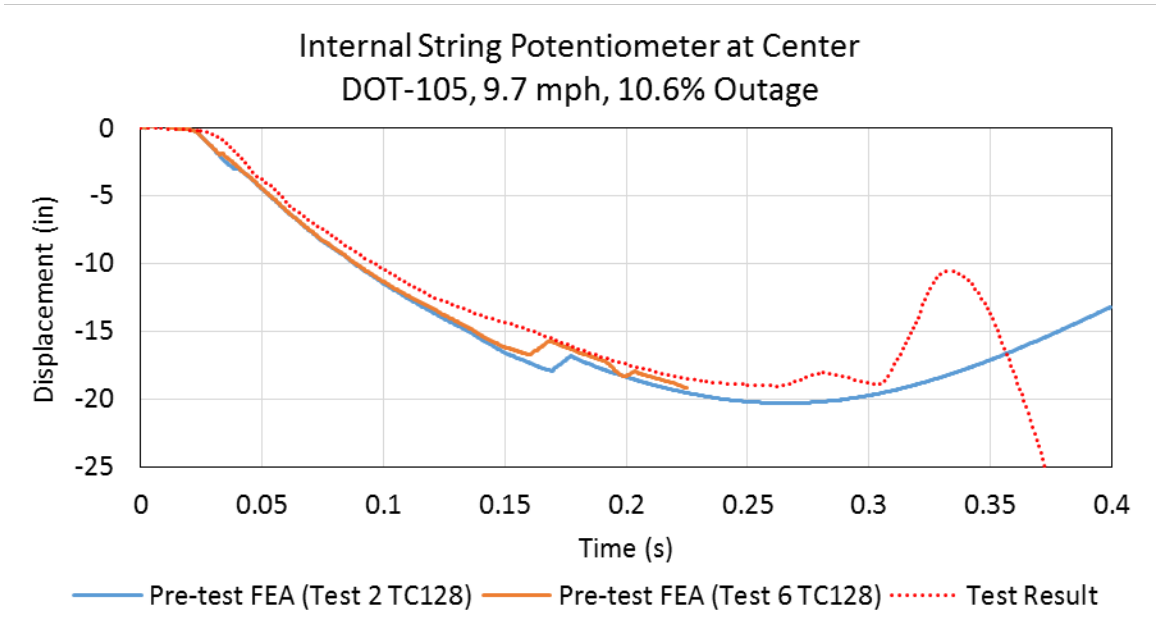

Figure 33. Change in Center String Potentiometer Length for Pre-Test FEA Compared to Test Results

Figure 34 contains a plot comparing the vertically oriented internal string potentiometer measurements at the center of the car against the pre-test FE model results. Both pre-test models exhibit good agreement with the test results in terms of the overall shapes of the curves, and the general magnitudes of the responses up to the point where puncture occurred at 0.26 seconds. The peak change in vertical length was bounded by the two TC128 material models used in pre-test simulations. A slight drop in displacement is observed at 0.175 seconds in the pre-test models that was not observed in the test result. This difference in vertical string potentiometer response may be due to the models not capturing fluid motion within the tank which could affect the ovalization of the tank.

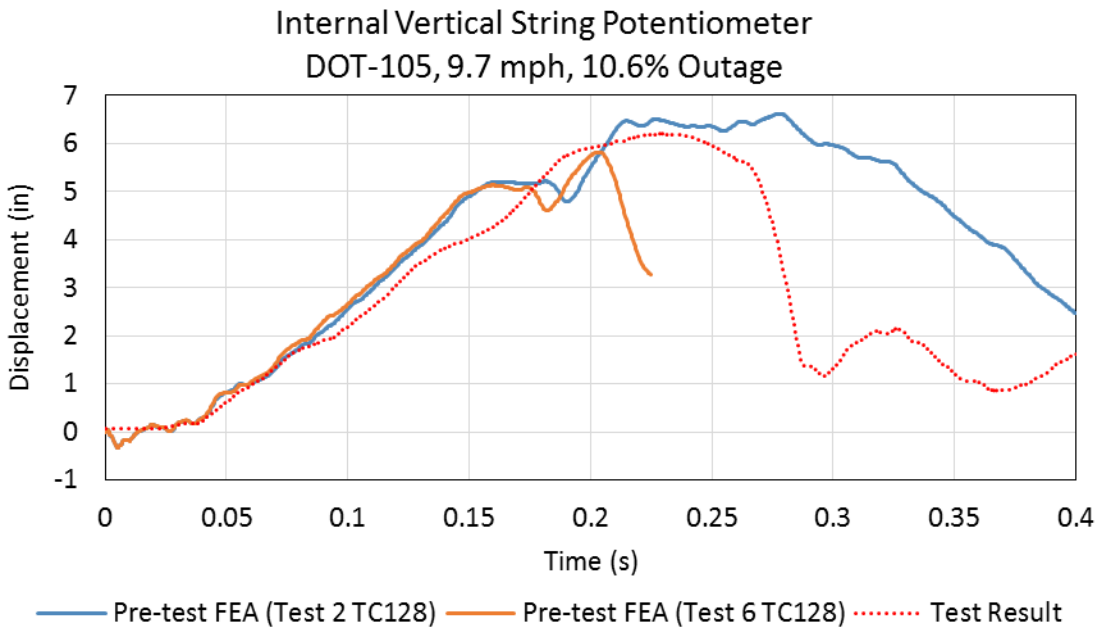

Figure 34. Change in Vertical String Potentiometer Length for Pre-Test FEA Compared to Test Results

6.4 Summary of Pre-Test FEA Comparison

The pre-test simulations were generally in agreement with the test results when comparing the peak values from the time history data channels. Table 15 summarizes the level of agreement between the pre-test simulations and the test results. Appendix C2 shows a more detailed comparison of the pre-test simulations and test results. Calculation for the peak values from the 24-inch and 48-inch offset string potentiometers were windowed around the time of puncture to remove noise (see Figure C15 and Figure C16 in Appendix C2).

The pre-test FEA using the Test 2 TC128 material model was generally in better agreement with the test results even though it did not experience puncture. While the Test 6 TC128 had mechanical properties that were closer to the actual material properties in the tested tank car, the puncture models tend to be conservative and predict puncture earlier in the impact than was observed in the test. This results in the Test 6 TC128 model predicting lower values for most results than were measured during the test. The differences in peak values from the pre-test FEA using the Test 6 TC128 material model are likely due to an early puncture outcome at

approximately 0.2 seconds while the impactor was still traveling at approximately 3.5 mph. For both the Test 2 and Test 6 TC128 materials, all the model results were within +/- 20 percent of the test measurements. The pre-test FE analyses allowed a test speed to be chosen that resulted in puncture of the tank car without an excess of residual kinetic energy.

Table 15. Comparison of Peak Results from Pre-Test Models and Test Results

Peak Measurement	Test Result	Pre-Test FEA (TC128 Test 2)	Pre-Test FEA (TC128 Test 2)	Pre-Test FEA (TC128 Test 6)	Pre-Test FEA (TC128 Test 6)
	Value	Value	Percent Difference	Value	Percent Difference
Longitudinal Acceleration (g)	2.84	2.57	-9.6%	2.36	-17.0%
Impact Force (kips)	842.7	756.8	-10.2%	695.2	-17.5%
Displacement at Peak Force (inches)	27.29	27.75	1.7%	24.12	-11.6%
Energy Absorbed at Peak Force (ft-kip)	929.9	920.2	-1.0%	776.7	-16.5%
Center String Potentiometer (inches)	19.11	20.30	6.2%	19.16	0.2%
24" Offset String Potentiometer (inches)	12.62	13.69	8.5%	10.98	-13.0%
24" Offset String Potentiometer (inches)	11.65	13.69	17.5%	10.98	-5.8%
48" Offset String Potentiometer (inches)	9.98	9.74	-2.4%	8.04	-19.4%
48" Offset String Potentiometer (inches)	9.50	9.74	2.5%	8.04	-15.4%
Vertical String Potentiometer (inches)	6.20	6.62	6.8%	5.82	-6.1%
Skid String Potentiometer (inches)	7.51	7.85	4.5%	7.80	3.8%
Skid String Potentiometer (inches)	6.94	7.85	13.1%	7.80	12.3%
Head String Potentiometer (inches)	7.61	7.54	-0.9%	7.52	-1.2%
Head String Potentiometer (inches)	6.84	7.54	10.2%	7.52	9.9%
Outage Pressure (psi)	112.9	111.9	-0.9%	108.8	-3.7%

7. Comparison of Test Response to Post-Test Analysis

Following the side impact test, the pre-test FE model was updated to include the measured TC128 mechanical properties. Researchers updated the impactor with the measured test speed of 9.7 mph and ram car weight of 296,775 pounds. The post-test modeling results are compared to the test results in this section. In general, the post-test model was conservative in predicting puncture but was still in good agreement with the measurements made during the test, as Figure 35 shows. The post-test simulation terminated at approximately 0.192 seconds due to puncture of the tank. Appendix C3 contains the complete set of comparisons between the post-test model and the test results.

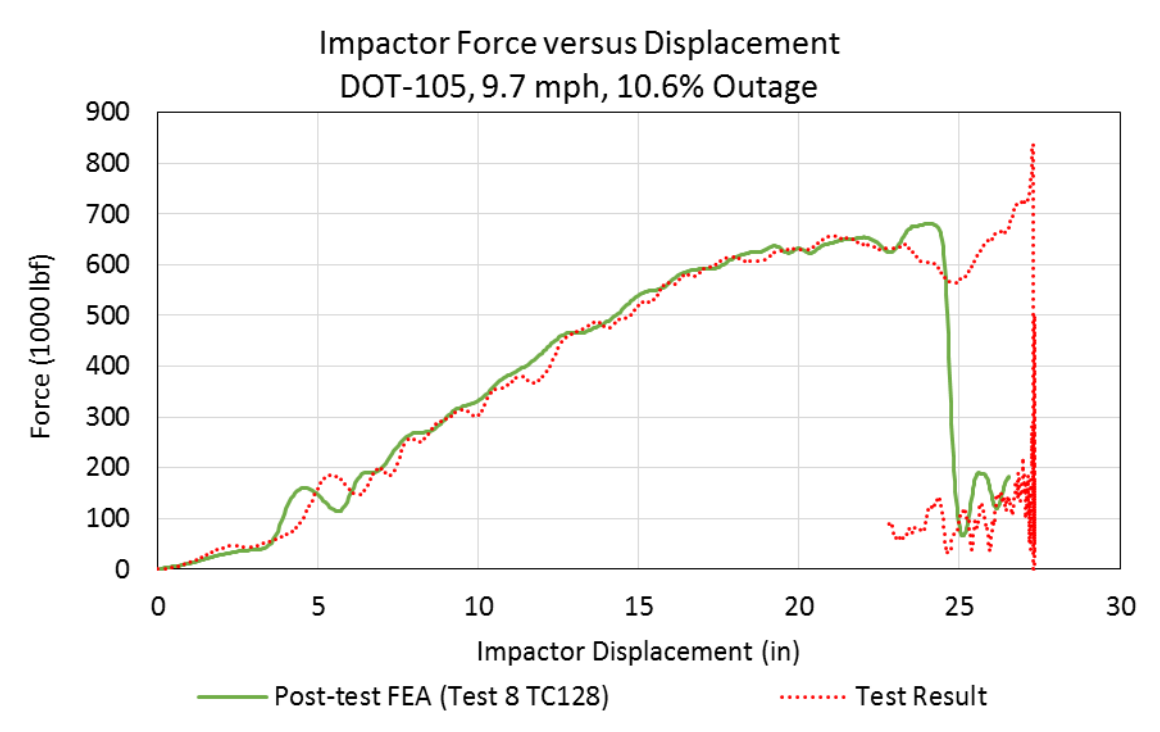

Figure 35. Post-Test FEA and Test Force-displacement Results

7.1 Deformation in Post-Test FE Model

Figure 36 displays a series of frames from a side view cut of the post-test FE model in 0.064-second increments up to the approximate point of puncture at 0.192 seconds. The reduction in volume of the outage (5 percent) was observed to be small.

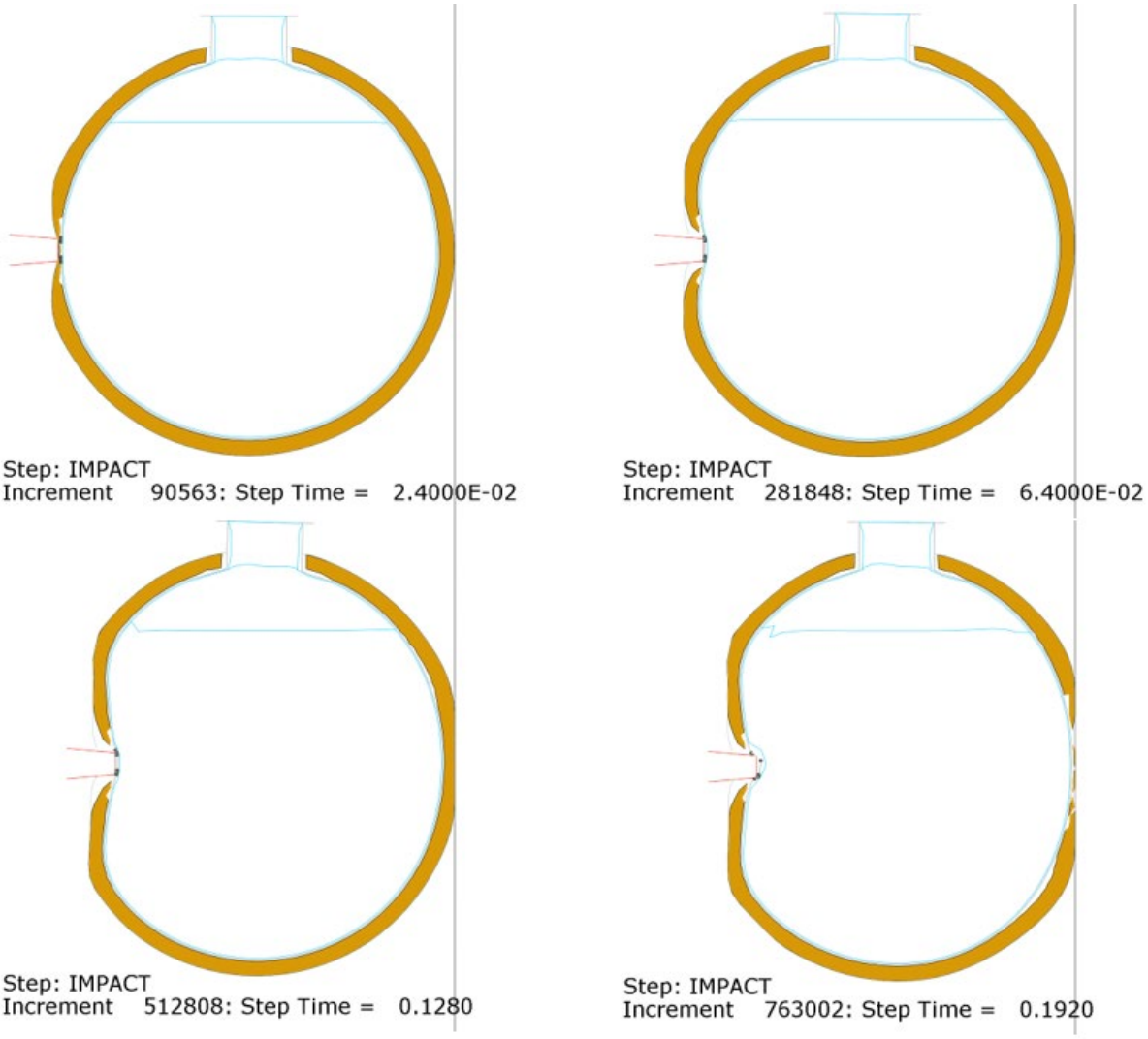

Figure 36. Side View Cuts of Impact Progression in Post-Test FE Model at Four Time Increments

Figure 37 shows the deformation of the tank, with the jacket and insulation hidden, in increments of 0.064 seconds up to the approximate time point of puncture at 0.192 seconds. Overlay contour plots of displacement are plotted on the tank and impactor. At the time of puncture, the impactor traveled approximately 25 inches. Note that this distance is measured starting from first contact with the exterior of the jacket; thus, the tank indentation at the time of puncture is less than the impactor travel distance.

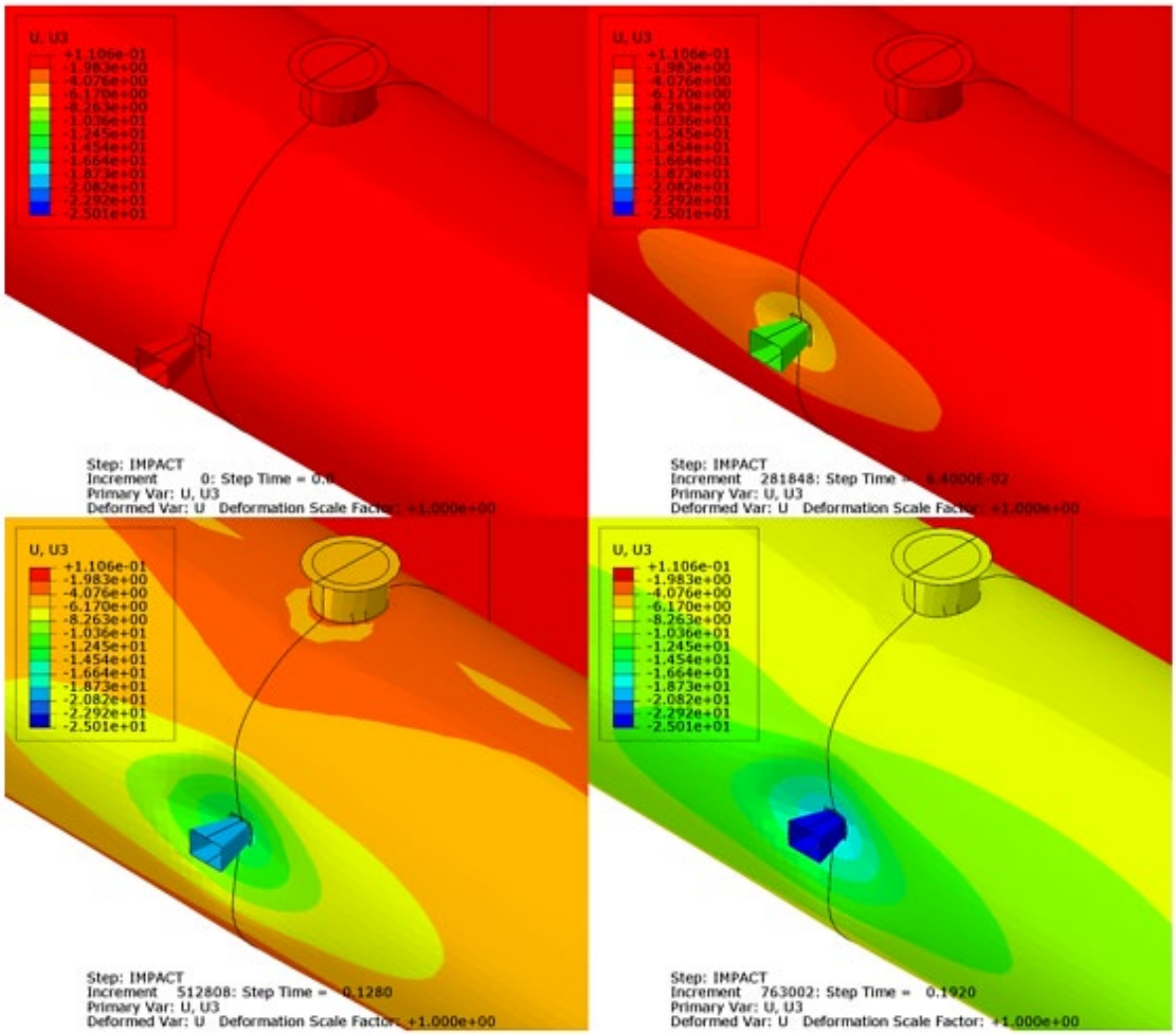

Figure 37. Isometric Views of Tank Deformation with Overlay Contour Plots of Displacement (inches) in Direction of Impactor Travel at Four Time Increments

7.2 Comparison of Air Pressure Results

Overall, the FE model captures the response of the fluid during the test. The model exhibits somewhat lower pressures compared to the test, particularly as the fluid displacement increases toward the end of the impact event. Figure 38 plots the average pressure-time history from the transducer in the manway within the air phase in the test and average air pressure within the outage in the FE model. The pressures correlate between the point where the model initially settles and the point where the model punctures.

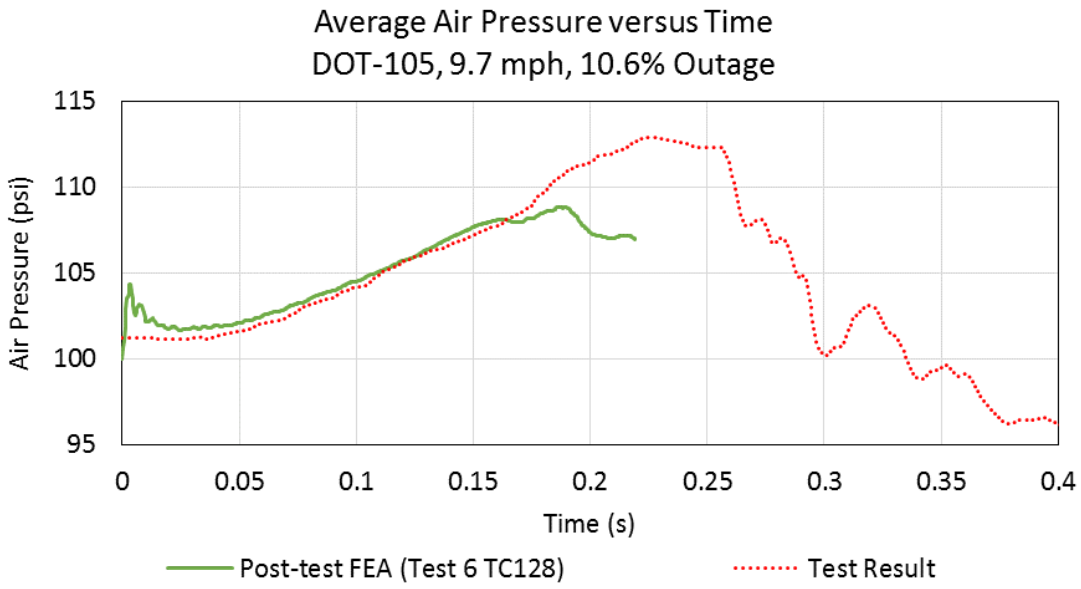

Figure 38. Average Air Pressure in Post-Test FEA and Test

7.3 Comparison of String Potentiometer Results

Figure 39 contains a plot of the A-end (TDASKID) and B-end (TDBSKID) skid displacements measured during the test and the skid displacement calculated in the post-test FE model. The overall shape of the skid displacement response in the model is similar to the A-end and B-end test curves and tends to fall within the same range. Note that because the model uses symmetry, a desirable outcome is a model result that is somewhere between the two measured skid displacements.

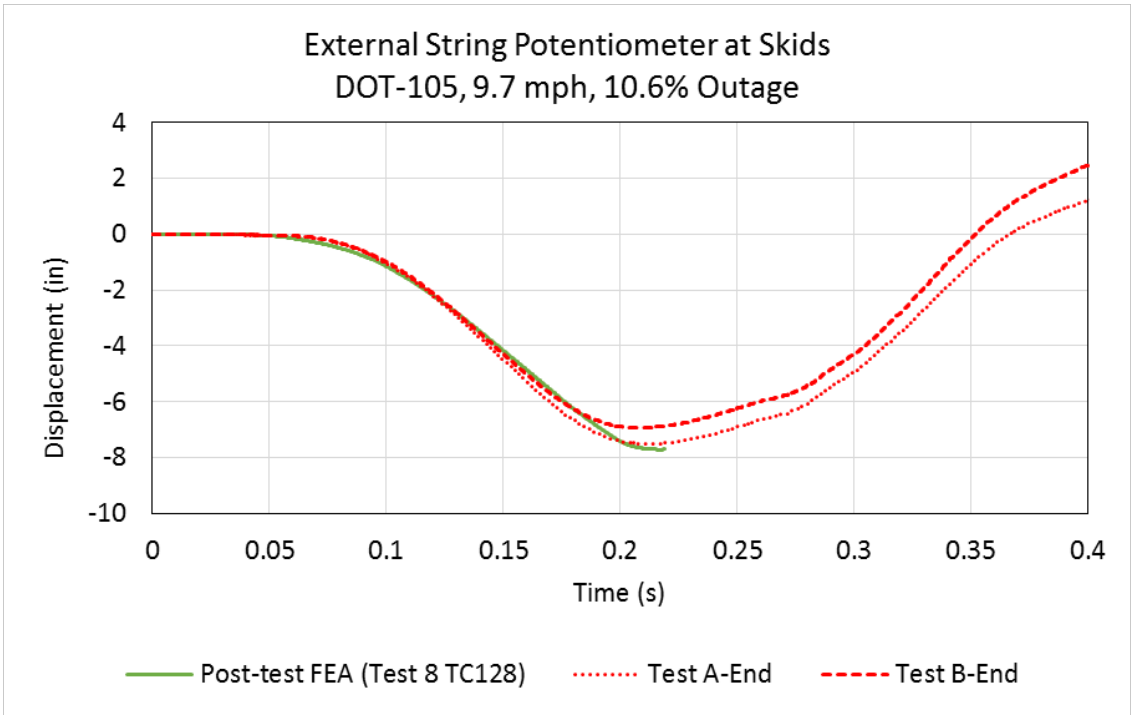

Figure 39. Skid Displacement in Post-Test Model and Test

The deformation within the DOT-105 tank car's tank was measured by string potentiometers in the test and by analogous soft springs in the FE model. Figure 40 plots the test results for the center of the tank, which was in line with the indenter with the post-test model results for comparison. The model and the test are in good agreement up to the time point where the model terminated at 0.22 seconds.

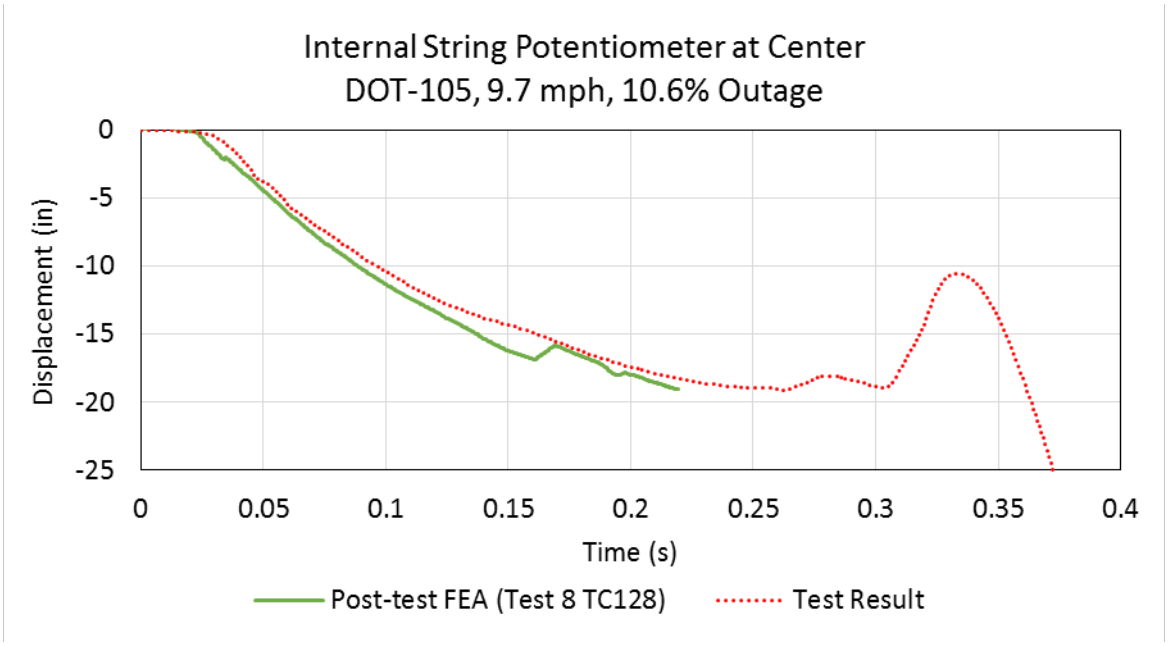

Figure 40. Internal String Potentiometer Measurement at Center of Tank in Post-Test Model and Test

7.4 Summary of Post-Test FEA Comparison

Table 16 contains a comparison between the peak measurements from the test and the corresponding peak value calculated for each output in the post-test FE model. This table also includes a column indicating the difference between the test measurement and FE calculations. The post-test model exhibited agreement that is consistent with the agreement obtained between the pre-test FEA and the test measurements. Overall, the post-test FE results are within 20 percent of the test measurements for nearly every measurement. Only one of the 48-inch offset string potentiometers has worse than 20 percent agreement. In general, the post-test FE model exhibited equal agreement with the test results compared to the pre-test model using Test 6 TC128 steel (Table 15).

In an attempt to quantify how conservative the post-test model was at predicting puncture, the initial speed of the impactor was iteratively reduced until the residual speed of the model (i.e., speed at the time of puncture) matched the test result. In the post-test model, an initial speed of 9 mph resulted in a 0.5 mph residual speed, which approximately matched the test result. Comparing the initial kinetic energy of the ram car in the post-test model run at 9 mph (803 foot-kips) versus the actual test run at 9.7 mph (933 foot-kips) indicates that the post-test model under predicts the puncture resistance of the DOT-105 car by approximately 14 percent. Note that if the percentage difference is calculated using velocity instead of energy, the post-test model would be reported to under-predict the speed to cause puncture by 7 percent.

Table 16. Comparison of Peak Results from Post-test FE Model and Test Results

Peak Measurement	Test Result	Post-Test FEA (TC128 Test 8)	Post-Test FEA (TC128 Test 8)
	Value	Value	Percent Difference
Longitudinal Acceleration (g)	2.84	2.29	-19.2%
Impact Force (kip)	842.7	680.4	-19.3%
Displacement at Peak Force (in)	27.29	24.08	-11.7%
Energy Absorbed at Peak Force (ft-kip)	929.9	770.5	-17.1%
Center String Potentiometer (inches)	19.11	19.08	-0.2%
24" Offset String Potentiometer (inches)	12.62	11.04	-12.5%
24" Offset String Potentiometer (inches)	11.65	11.04	-5.3%
48" Offset String Potentiometer (inches)	9.98	7.83	-21.6%
48" Offset String Potentiometer (inches)	9.50	7.83	-17.6%
Vertical String Potentiometer (inches)	6.20	5.52	-10.9%
Skid String Potentiometer (inches)	7.51	7.71	2.7%
Skid String Potentiometer (inches)	6.94	7.71	11.1%
Head String Potentiometer (inches)	7.61	7.43	-2.3%
Head String Potentiometer (inches)	6.84	7.43	8.6%
Outage Pressure (psi)	112.9	108.9	-3.6%

8. Conclusion

This report documents the combined efforts of TTCI and Volpe to test and analyze the side impact puncture performance of a DOT specification 105A500W tank car on August 1, 2018. This research supports FRA's tank car research program to provide the technical basis for rulemaking on enhanced and alternative performance standards for tank cars.

The tank car was filled with water to approximately 89.5 percent of its volume. It was then sealed and pressurized to 100 psi. The intention of the test was to strike the tank car at a speed high enough to result in significant damage to the tank and possibly puncture the tank's shell. The tank car was impacted by a 296,775-pound ram car traveling 9.7 mph. A 6-inch by 6-inch ram head fitted to the ram car impacted the tank center. The impact punctured the tank shell after slowing the ram car to less than 1 mph.

Pre-test FE modeling was used to estimate the overall response of the tank to the impact, including the force-displacement response. The model estimated the puncture range between 8.5 and 11 mph. The test outcome of puncture after nearly stopping the car from a 9.7 mph impact was in agreement with the pre-test modeling. The pre-test models exhibited good agreement with the measured force-displacement result from the test. Additionally, the internal pressure-time response and the displacements of the tank measured by string potentiometers were all in good agreement with the pre-test model estimates. The test delivered a successful impact at a measured speed that was close to the desired impact speed, as estimated by the pre-test models. The pre-test models allowed for a successful estimation of the speed range that would cause puncture of the tank without imparting an excess amount of kinetic energy.

Following the test, material coupons were cut from undamaged regions of the tested car. These coupons were used to generate a new material response, which researchers implemented in the post-test FE model. Additionally, the post-test model was run at the actual impact speed as measured during the test. When run at the test speed, the post-test model estimates puncture of the tank car using the actual material responses. The post-test model is conservative, as evidenced by the residual speed in the impactor at the time of puncture. In the post-test model, the impactor has slowed to approximately 3 mph, while the test measurements indicate that the impactor had slowed to 0.5 mph at the time of puncture. These results indicate that the test speed only slightly exceeded the puncture/non-puncture threshold speed. Post-test FE modeling showed that if the simulated impact speed were lowered from the measured speed by 7 percent, the model would puncture with a residual speed approximately the same as that measured in the test. Thus, the model estimates puncture at a slightly lower impact speed than would be expected to puncture the tank car if a future test were to be run at exactly the puncture/non-puncture threshold speed.

The FE modeling performed in this effort used simplified hydraulic and pneumatic cavity modeling techniques to simulate the water and air responses, respectively. These modeling simplifications resulted in a puncture-capable model with an improved runtime compared to previously used explicit lading representations. The test measurements confirmed that these modeling simplifications provided a reasonable representation of the fluid behaviors in the tank car. However, it should be noted that this test featured a relatively small tank car having a relatively large outage at an initially elevated pressure. Further work is necessary to ascertain whether the cavity simplifications are appropriate for larger capacity tank cars, small outage volumes, and outages that are initially at a lower pressure.

One intent of this test was to produce test data that could be used by other entities wishing to model tank car impacts during their model validation activities. Currently, FRA does not have agreed-upon model validation criteria or procedures for models used to simulate tank car impacts. However, establishing that a complex computational model has a sound basis in physics is a fundamental part of any modeling or simulation activity. Developing a set of criteria and procedures for validating tank car impact and puncture response models should be considered as a future activity if new or innovative tank cars are to be developed in the future that may be evaluated using modeling.

9. References

Abaqus Example Problems Manual. (2014). *Example Problem 2.1.12 - Cask drop with foam impact limiter*. Providence: Dassault Systemes Simulia Corp.

Association of American Railroads. (1978). Specification M-1002, Manufacture of Tank Cars. In *Manual of Standards and Recommended Practices.* Washington, DC.

Bao, Y., & Wierzbicki, T. (2004). On fracture locus in the equivalent strain and stress triaxiality space. *International Journal of Mechanical Sciences, 46*(1), 81-98.

Carolan, M. E., et al. (2013, April). *Application of Welded Steel Sandwich Panels for Tank Car Sheel Impact Protection*. Technical Report No. DOT/FRA/ORD-13/19. Washington, DC: U.S. Department of Transportation, Federal Railroad Administration.

Carolan, M., & Rakoczy, P. (2019, May). *Side Impact Test and Analyses of a DOT-105 Tank Car*. Technical Report No. DOT/FRA/ORD-19/12. Washington DC: U.S. Department of Transportation, Federal Railroad Administration.

Dassault Systemes Simulia Corp. (2014). *Abaqua 6.14-2.* Providence: Dassault Systemes Simulia Corp.

Elkins, A. (2017). *Field Guide to Tank Cars*. Third Edition. Washington, DC: Association of American Railroads/Bureau of Explosives. Retrieved from Association of American Railroads.

Engineering ToolBox. (2003). *Air - Altitude, Density and Specific Volume*. Engineering ToolBox.

Engineering ToolBox. (2003). *Water - Density, Specific Weight and Thermal Expansion Cooefficient*. Engineering ToolBox.

Engineering ToolBox. (2004). *Air - Molecular Weight and Composition*. Engineering ToolBox:

Engineering ToolBox. (2004). *Universal and Individual Gas Constant*. Engineering ToolBox.

Engineering ToolBox. (2004). *Velocity of Sound in Water*. Engineering ToolBox.

Goods, S. H., Neuschwanger, C. L., Whinnery, L. L. (1998, Apr 01). *Mechanical Properties of a Structural Polyurethane Foam and the Effect of Particulate Loading*. Technical Report No. SAND-98-8549C; CONF-980405-ON. Livermore, CA: Sandia National Laboratories. doi:10.2172/650182

Kirkpatrick, S. W. (2010, January). *Detailed Puncture Analyses of Various Tank Car Designs: FInal Report - Revision 1*. Mountain View, CA: Applied Research Associations, Inc. Retrieved from Applied Research Associates.

Kirkpatrick, S., Rakoczy, P., MacNeill, R. A., & Anderson, A. (2015). *Side Impact Test and Analyses of a DOT-111 Tank Car*. Technical Report No. DOT/FRA/ORD-15/30. Washington, DC: U.S. Department of Transportation, Federal Railroad Administration.

Lee, Y.-W. (2005). *Fracture Prediction in Metal Sheets*. Boston, MA: Massachusetts Institute of Technology.

Lee, Y.-W., & Wierzbicki, T. (2004, August). *Quick Fracture Calibration for Industrial Use.* Impact & Crashworthiness Laboratory, Report No. 115.

McKeighan, P., Jeong, D. Y., & Cardinal, J. W. (2008). *Mechanical Properties of Tank Car Steels Retired from the Fleet*. *Proceedings of 2009 ASME Joint Rail Conference.* Report No. JRC2009-63060. Pueblo, CO: U.S. Department of Transportation, Federal Railroad Administration.

Paredes, M., Sarzosa, D., Savioli, R., Wierzbicki, T., Jeong, D., & Tyrell, D. (2018). Ductile tearing analysis of TC128 tank car steel under mode I Loading Condition. *Theoretical and Applied Fracture Mechanics, 96*, 658-675.

Pipeline and Hazardous Materials Safety Administration, U.S. Department of Transportation. (2015). *Tank-head puncture-resistance systems.* Retrieved from Title 49 Code of Federal Regulations Section 179.16.

Rakoczy, P., & Carolan, M. (2016, December). *Side Impact Test and Analyses of a DOT-112 Tank Car.* Technical Reports, DOT/FRA/ORD-16/38. Washington, DC: U.S. Department of Transportation.

Rakoczy, P., Carolan, M., Gorhum, T., & Eshraghi, S. (2019, May). *Side Impact Test and Analyses of a DOT-117 Tank Car.* Technical Report No. DOT/FRA/ORD-19/13. Washington, DC: U.S. Department of Transportation, Federal Railroad Administrationo.

SAE International. (2007). *SAE J211/1 Standard. 1995. Instrumentation for Impact Test - Part 1: Electronic Instrumentation.* Warrendale.

Smits, A. (2000). *A Physical Introduction to Fluid Mechanics.* New York: John Wiley & Sons, Inc.

Tang, Y. H., Yu, H., Gordon, J. E., Jeong, D. Y., & Perlman, A. B. (2008). *Analysis of Railroad Tank Car Shell Impacts Using Finite Element Method*. *Proceedings of the 2008 IEEE/ASME Joint Rail Conference.* Report No. JRC2008-63014. Wilmington, DE: U.S. Departmentment of Transportation, Federal Railroad Administration.

Transportation Technology Center, Inc. (2016). *Test Implementation Plan for FRA Tank Car Side Impact, Revision 1.* Pueblo: Association of American Railroads/TTCI.

U.S. Climate Data version 3.0. (2019). Climate Pueblo - Colorado and Weather Averages Pueblo.

U.S. Geologic Survey. (2019). *GNIS Detail -- Pueblo Memorial Airport*. USGS Geographic Names Information System.

Urieli, I. (2008). Specific Heat Capacities of Air. Ohio University.

Yu, H., Jeong, D. Y., Gordon, J. E., & Tang, Y. H. (2007). Analysis of Impact Energy to Fracture Un-Notched Charpy Specimens Made from Railroad Tank Car Steel. *Proceedings of the 2007 ASME Rail Transportation Division Fall Technical Conference* (p. 8). Report No. RTDF2007. Chicago, IL: U.S. Department of Transportation, Federal Railroad Administration.

Yu, H., Tang, Y.H. Gordon, J. E., & Jeong, D. Y. (2009). Modeling the Effect of Fluid-Structure Interaction on the Impact Dynamics of Pressurized Tank Cars. *Proceedings of 2009*

ASME International Mechanical Engineering Congress and Exposition IMECE2009-11926. Lake Buena Vista, FL: U.S. Department of Transportation, Federal Railroad Administration.

Appendix A.
Camera and Target Positions

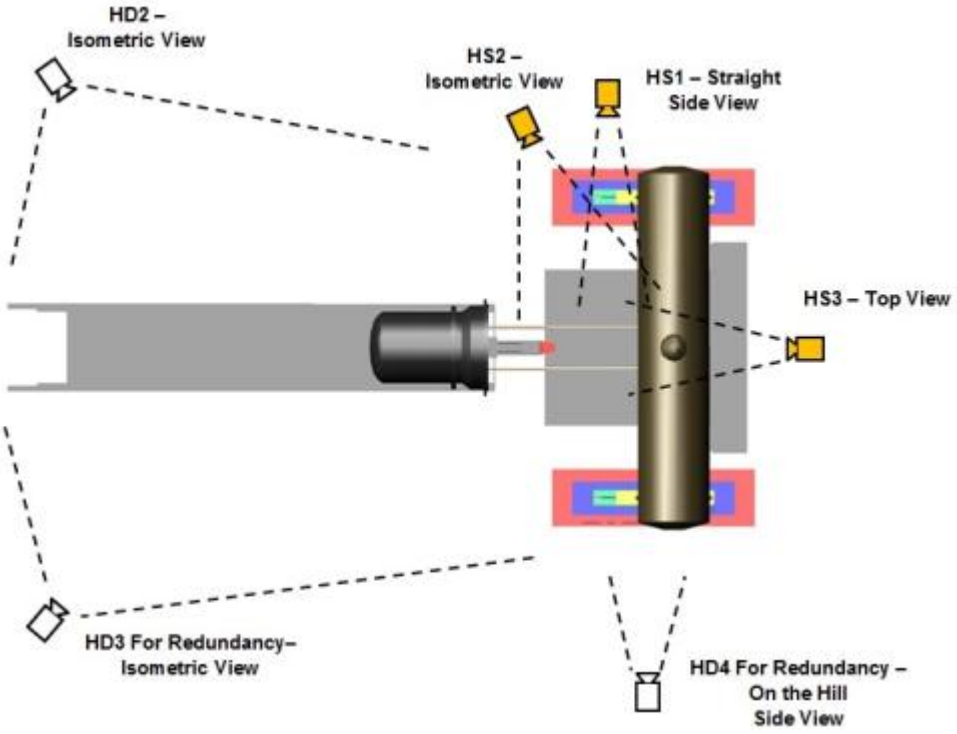

Figure A1. Camera Positions (top) — High Speed (HS), High Definition (HD)

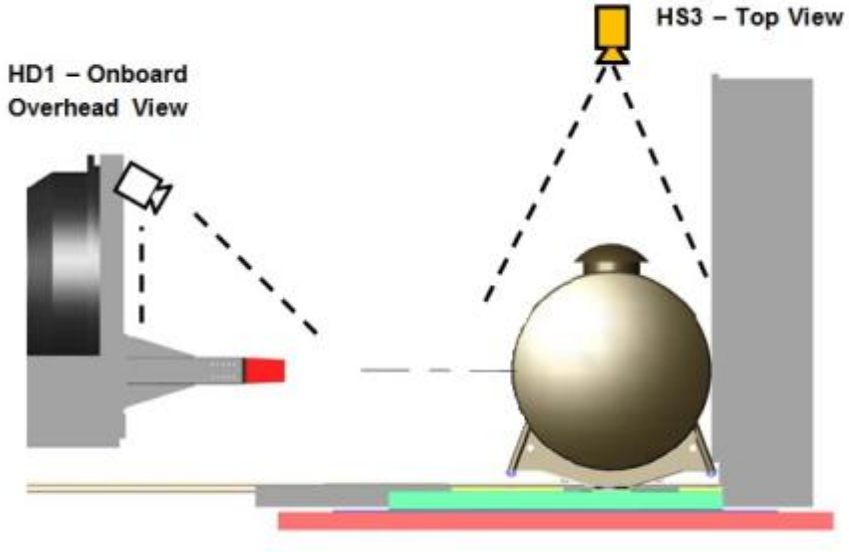

Figure A2. Camera Positions (side) — High Speed (HS), High Definition (HD)

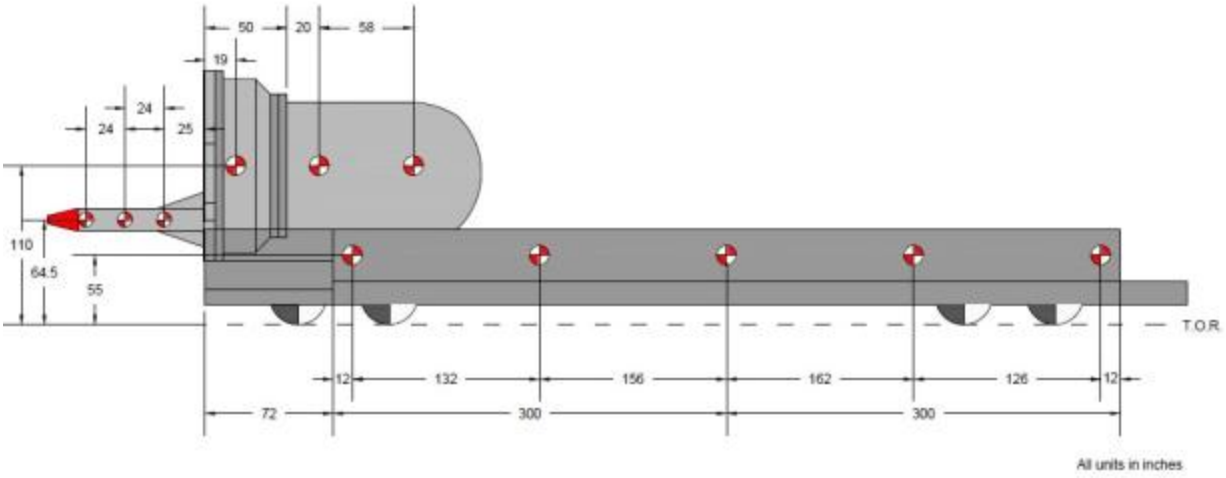

Figure A3. Ram Car Target Positions

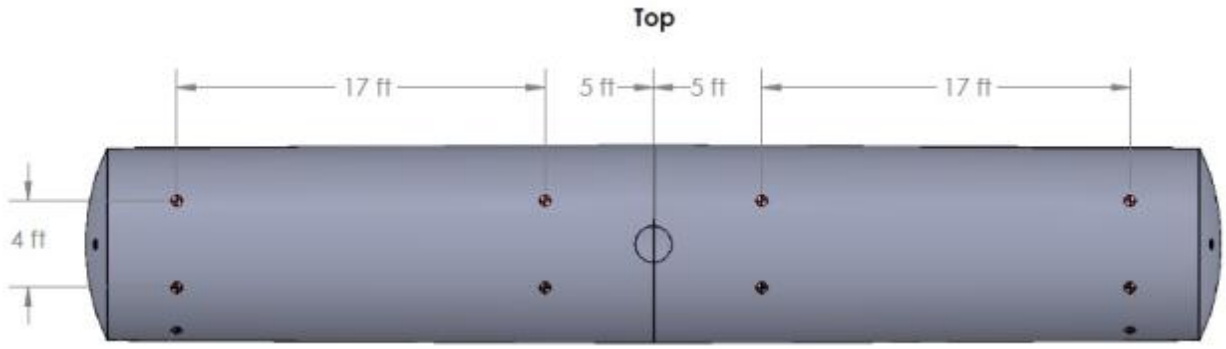

Figure A4. Tank Car Target Positions (top)

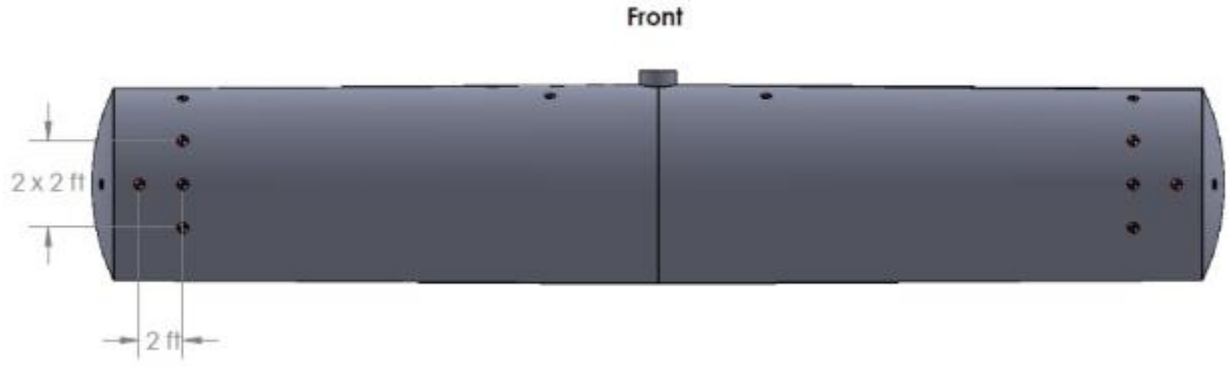

Figure A5. Tank Car Target Positions (front)

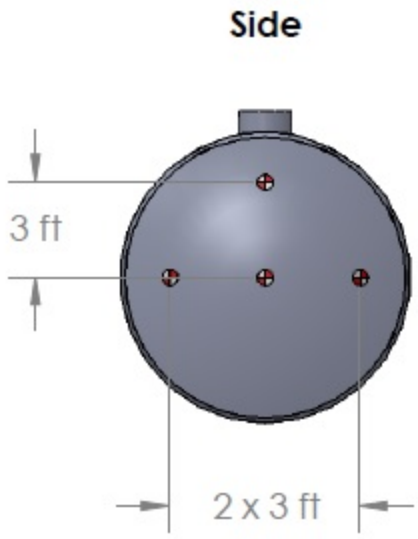

Figure A6. Tank Car Target Positions (side)

Appendix B.
Test Data

This contains raw and filtered test data. The raw accelerations and internal pressures measured on different locations on the impact cart were processed as follows. The test data from -1 to -0.1 seconds on each channel were averaged, and this value was subtracted from the test measurements to remove any initial offsets in the data. Each channel was then filtered to channel frequency class (CFC) 60, using the procedures given in 8SAE J211 (SAE International, 2007). Displacement data did not require any filtration.

B1 – Accelerations

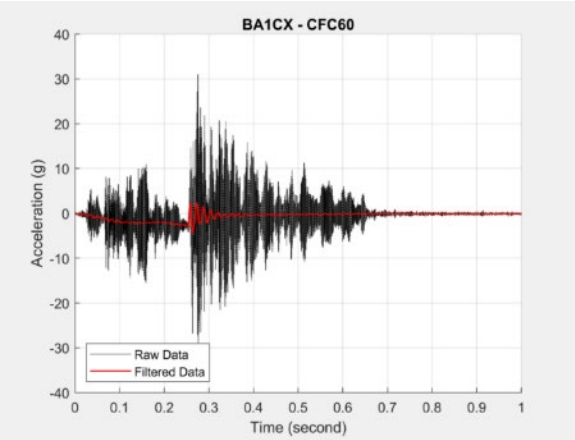

Figure B1. Raw and CFC60 Filtered Acceleration-Time Data from BA1CX

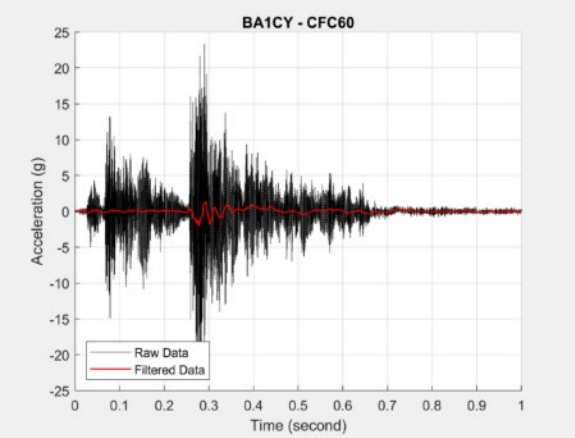

Figure B2. Raw and CFC60 Filtered Acceleration-Time Data from BA1CY

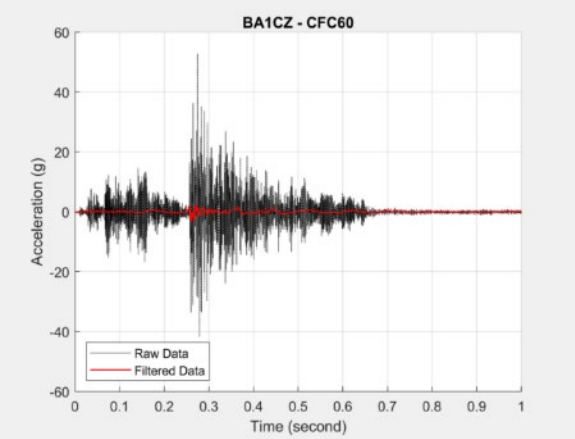

Figure B3. Raw and CFC60 Filtered Acceleration-Time Data from BA1CZ

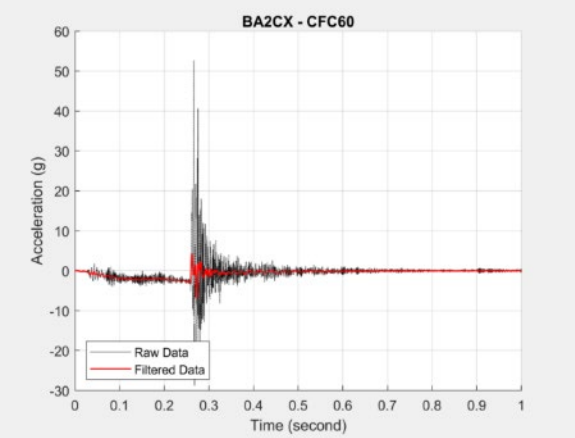

Figure B4. Raw and CFC60 Filtered Acceleration-Time Data from BA2CX

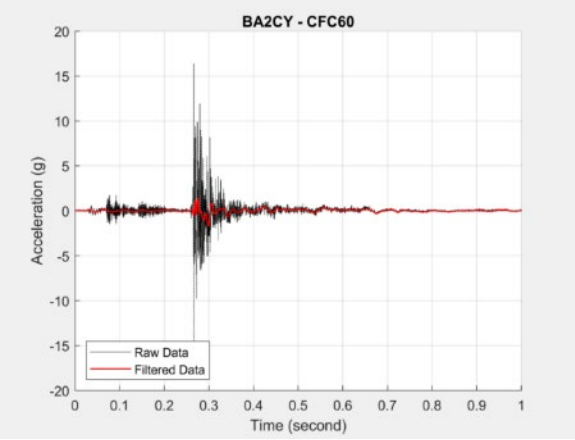

Figure B5. Raw and CFC60 Filtered Acceleration-Time Data from BA2CY

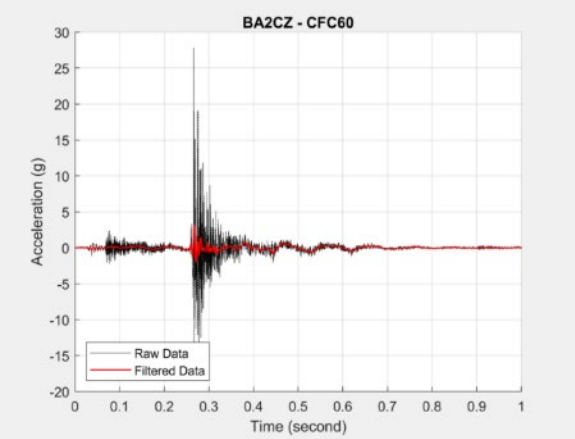

Figure B6. Raw and CFC60 Filtered Acceleration-Time Data from BA2CZ

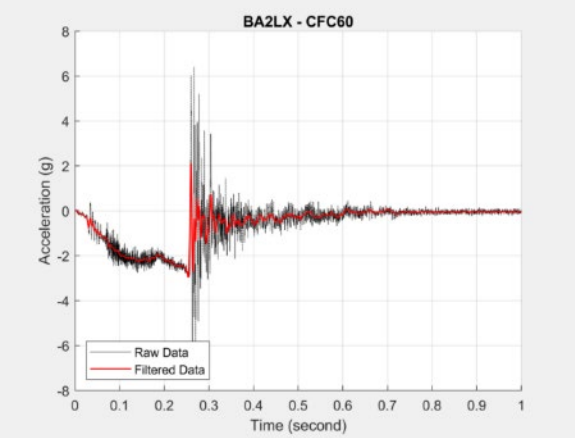

Figure B7. Raw and CFC60 Filtered Acceleration-Time Data from BA2LX

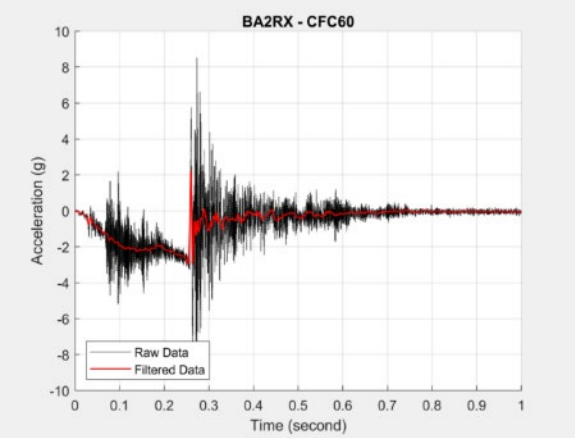

Figure B8. Raw and CFC60 Filtered Acceleration-Time Data from BA2RX

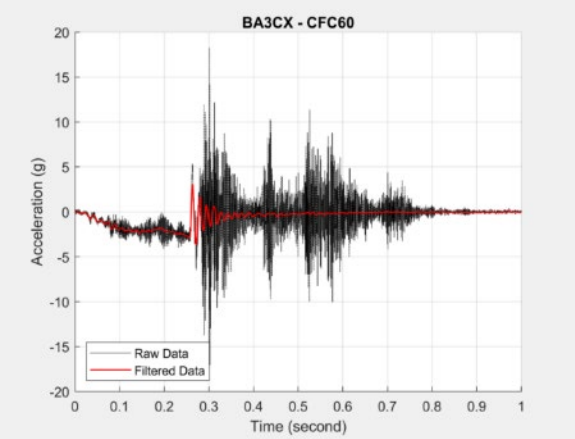

Figure B9. Raw and CFC60 Filtered Acceleration-Time Data from BA3CX

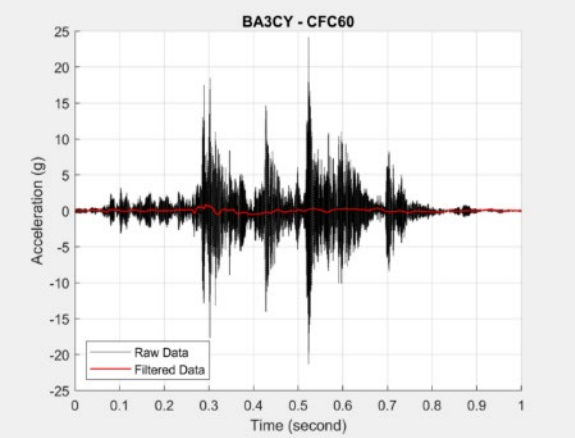

Figure B10. Raw and CFC60 Filtered Acceleration-Time Data from BA3CY

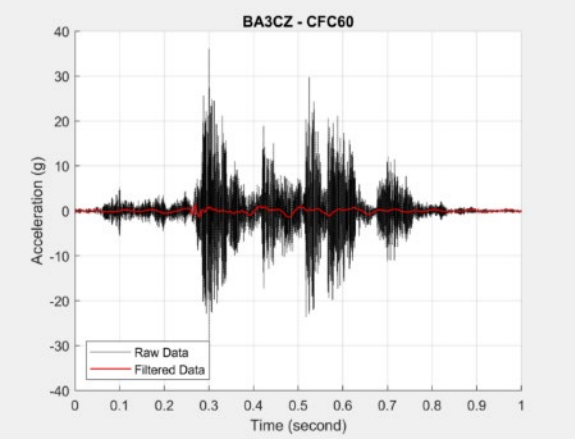

Figure B11. Raw and CFC60 Filtered Acceleration-Time Data from BA3CZ

B2 – Pressures

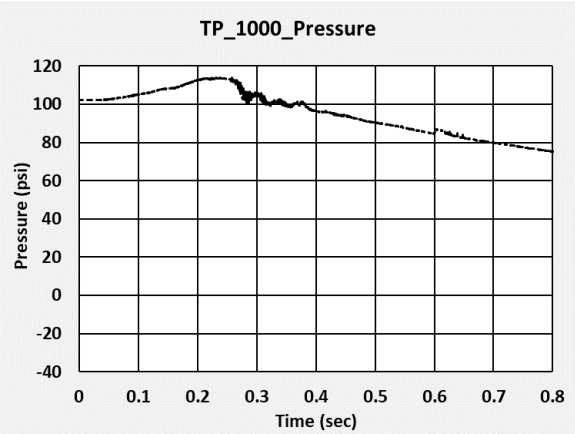

Figure B12. Raw Pressure-Time Data from TP1000

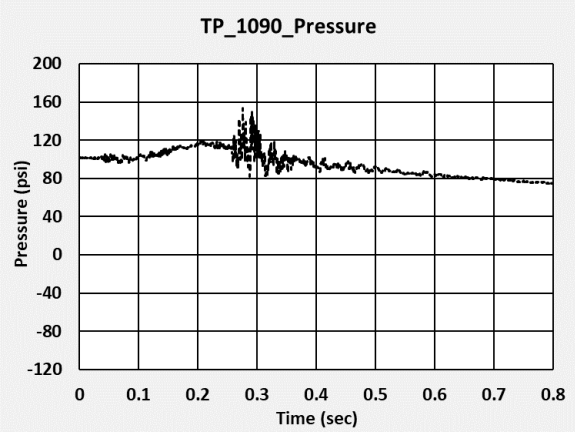

Figure B13. Raw Pressure-Time Data from TP1090

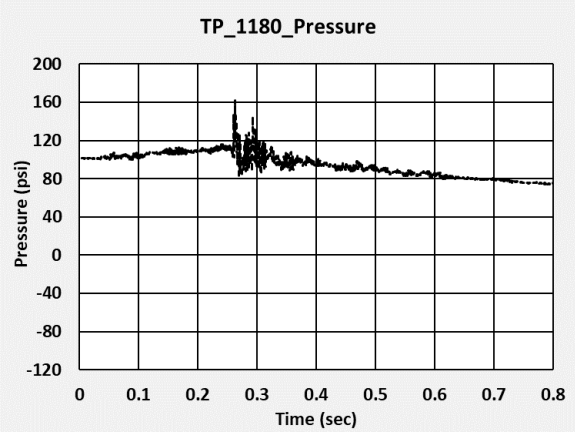

Figure B14. Raw Pressure-Time Data from TP1180

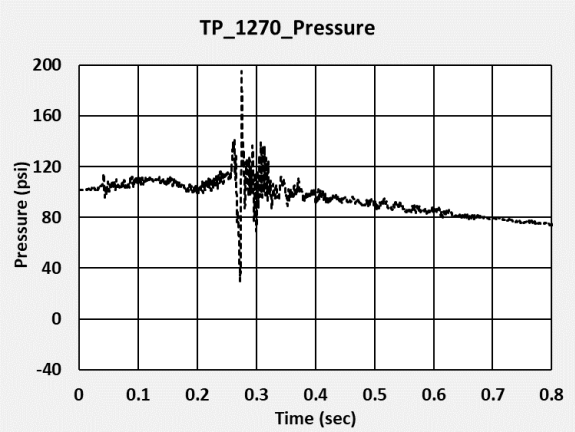

Figure B15. Raw Pressure-Time Data from TP1270

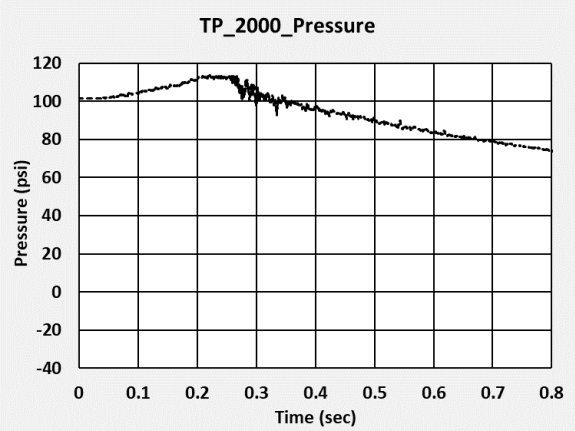

Figure B16. Raw Pressure-Time Data from TP2000

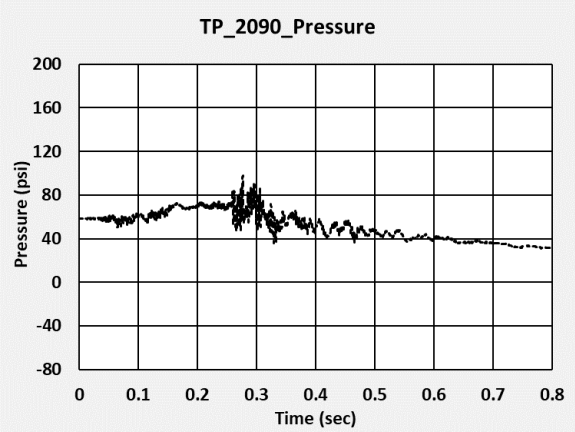

Figure B17. Raw Pressure-Time Data from TP2090

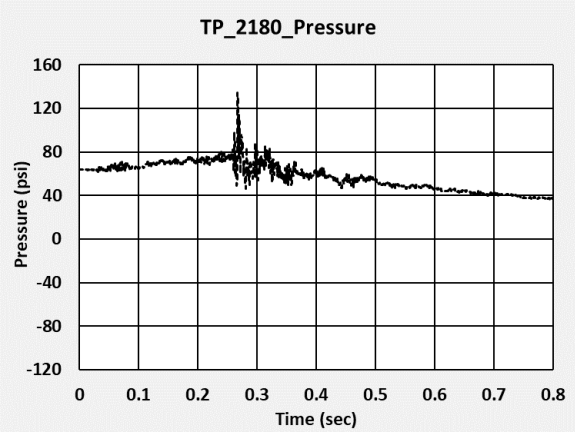

Figure B18. Raw Pressure-Time Data from TP2180

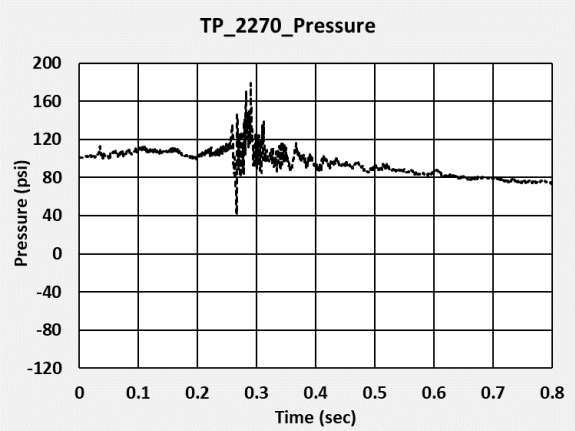

Figure B19. Raw Pressure-Time Data from TP2270

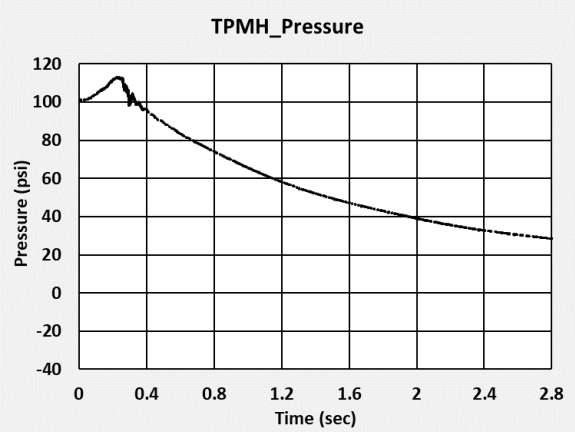

Figure B20. Raw Pressure-Time Data from TPMH

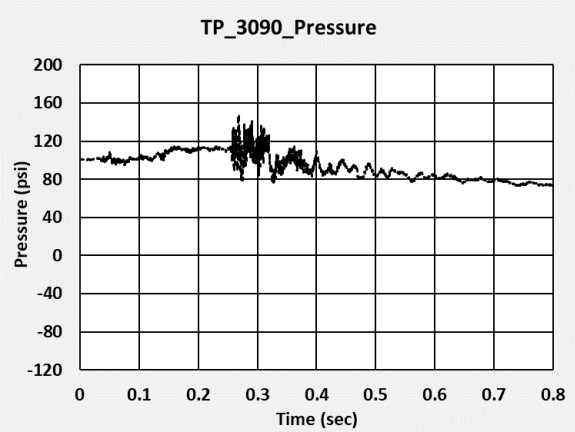

Figure B21. Raw Pressure-Time Data from TP3090

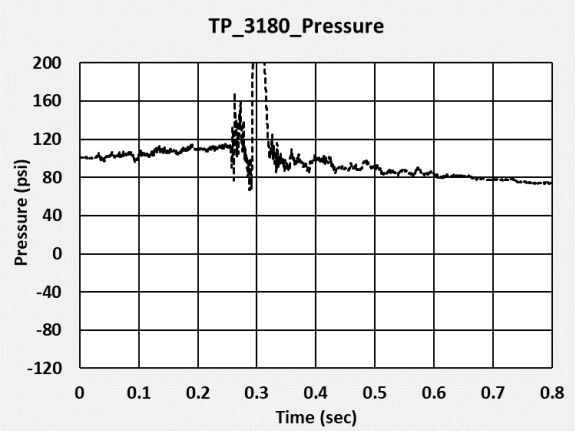

Figure B22. Raw Pressure-Time Data from TP3180

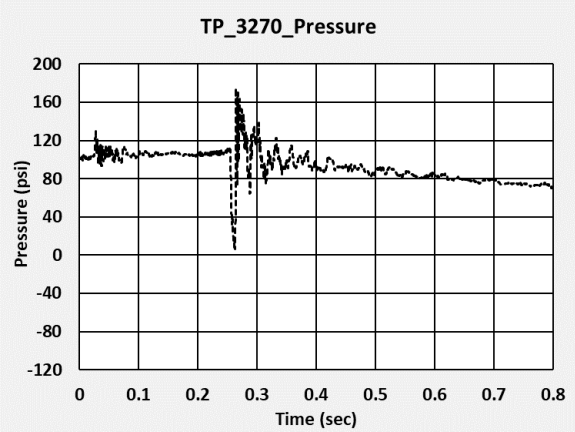

Figure B23. Raw Pressure-Time Data from TP3270

B3 – Displacements

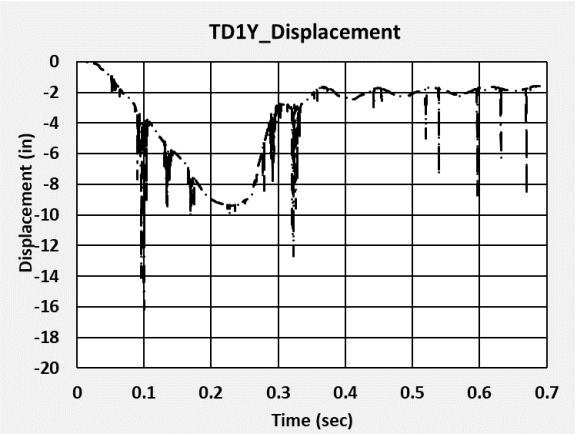

Figure B24. Raw Displacement-Time Data from TD1Y

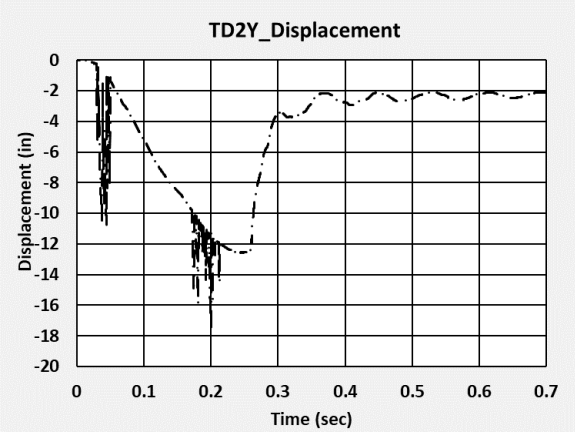

Figure B25. Raw Displacement-Time Data from TD2Y

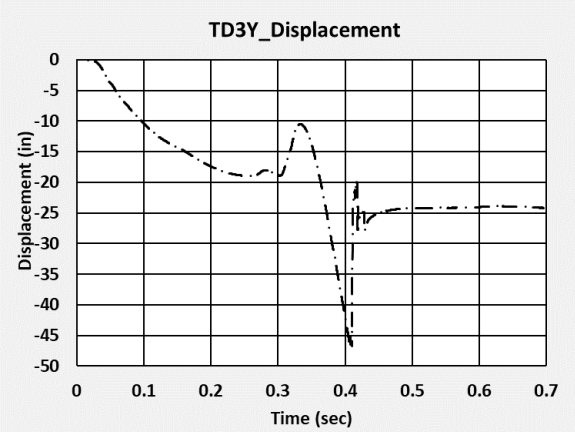

Figure B26. Raw Displacement-Time Data from TD3Y

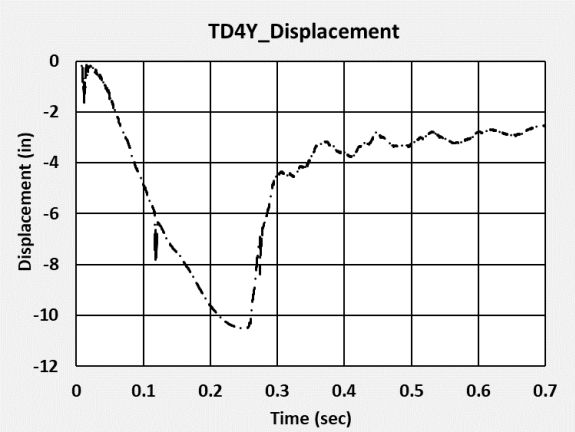

Figure B27. Raw Displacement-Time Data from TD4Y

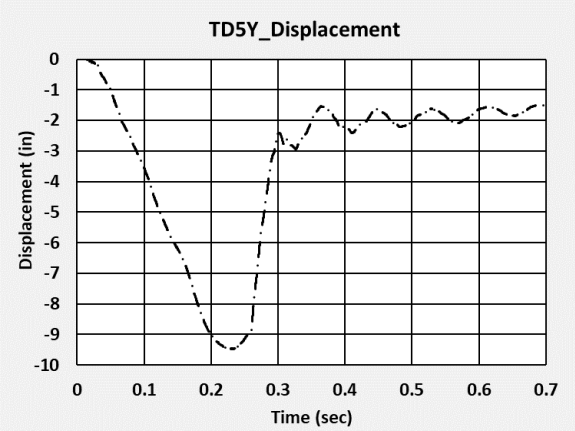

Figure B28. Raw Displacement-Time Data from TD5Y

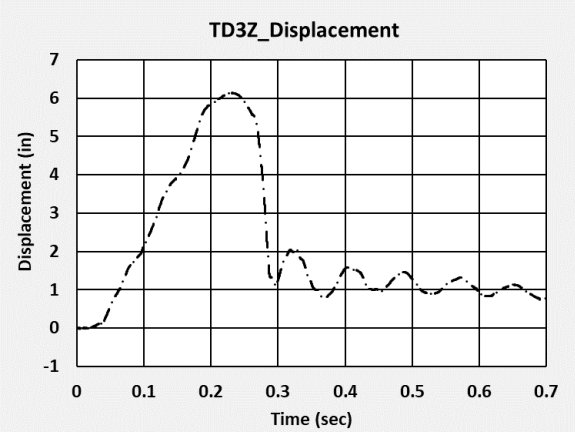

Figure B29. Raw Displacement-Time Data from TD3Z

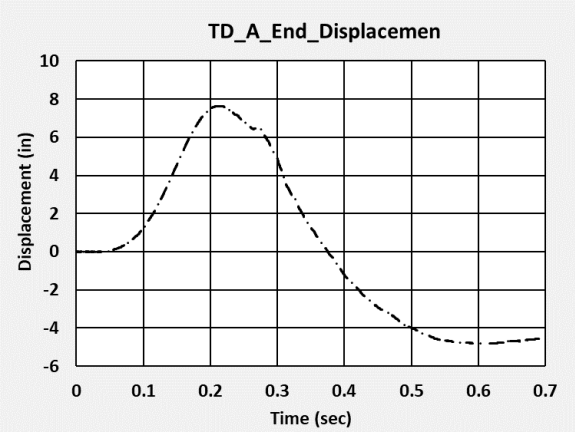

Figure B30. Raw Displacement-Time Data from Displacement Transducer on A-End Head

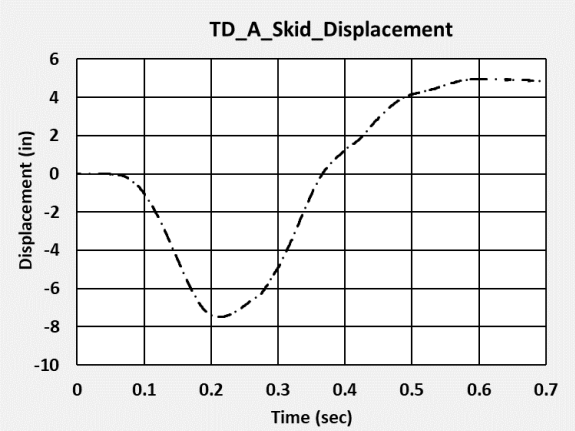

Figure B31. Raw Displacement-Time Data from Displacement Transducer on A-End Skid

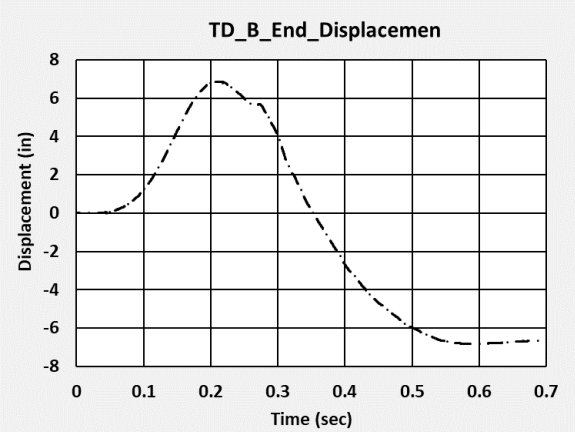

Figure B32. Raw Displacement-Time Data from Displacement Transducer on B-End Head

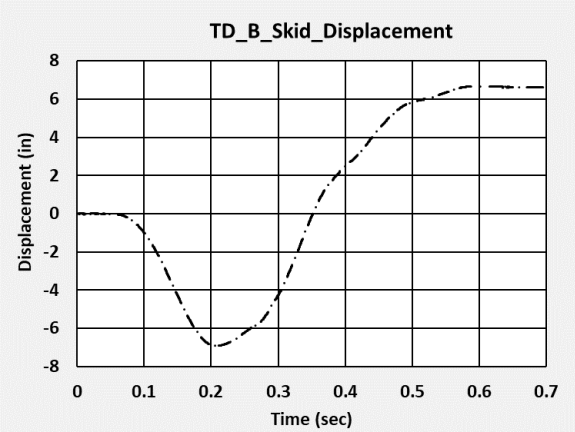

Figure B33. Raw Displacement-Time Data from Displacement Transducer on B-End Skid

B4 – Material Characterization Results

Westmoreland Mechanical Testing & Research, Inc.
P.O.Box 388; 221 Westmoreland Drive
Youngstown, PA 15696-0388 U.S.A.
Telephone: 724-537-3131 Fax: 724-537-3151
Website: www.wmtr.com E-Mail: admin@wmtr.com
WMT&R is a technical leader in the material testing industry.

ACCREDITED
TESTING CERT 621-01 & 621-02

Accredited Nadcap Materials Testing Laboratory

Corrected Dates
April 5, 2019
April 12, 2019

CERTIFICATION

Section 1 of 3

April 2, 2019
Transportation Technology Center Inc.
55500 DOT Road
P.O. Box 11130
Pueblo, CO 81001

WMT&R Report No. 9-52868
P.O. No. 60288
WMT&R Quote No. QN190450
Requisition No. 1908249

Attention: Shawn Trevithick

Subject: All processes, performed upon the material as received, were conducted at WMT&R, Inc. in accordance with the WMT&R Quality Assurance Manual, Rev. 11, dated 12/03/2008.
The following tests were performed on this order: TENSILE

TENSILE RESULTS: ASTM E8-16a
SPEED OF TESTING: 0.005 in./in./min.
MATERIAL: TC 128 Gr. B
DISPOSITION: Report

SID	TestLog Number	Temp.	UTS ksi	0.2% YS ksi	Elong %	RA %	Modulus Msi	Ult. Load lbf	0.2% YLD. lbf	Orig. Dia. (in.)	Final Dia. (in.)	4D Orig GL (in.)	4D Final GL (in.)	Orig. Area (sq. in.)	Machine Number	A\U\R
Tank Car 8-1	887HHH	Room	94.1	70.2	25	49	51.9	18676	13936	0.5027	0.3574	2.00	2.49	0.19847584	M10	R
Tank Car 8-2	888HHH	Room	94.1	70.6	26	48	39.0	18705	14031	0.5030	0.3624	2.00	2.52	0.19871280	M10	R
Tank Car 8-3	889HHH	Room	94.0	70.1	25	49	36.5	18680	13931	0.5029	0.3605	2.00	2.49	0.19863380	M10	R

A\U\R: A=ACCEPTABLE, U=UNACCEPTABLE, R=REPORT

WESTMORELAND MECHANICAL TESTING & RESEARCH, Inc

Stress vs. Strain

Phone: (724)537-3131

Customer: Transportation Technology Center Inc.
WMT&R Report: 9-52868

P.O. No.: 60288
WMT&R Quote No.: QN190450
Requisition No.: 1908249

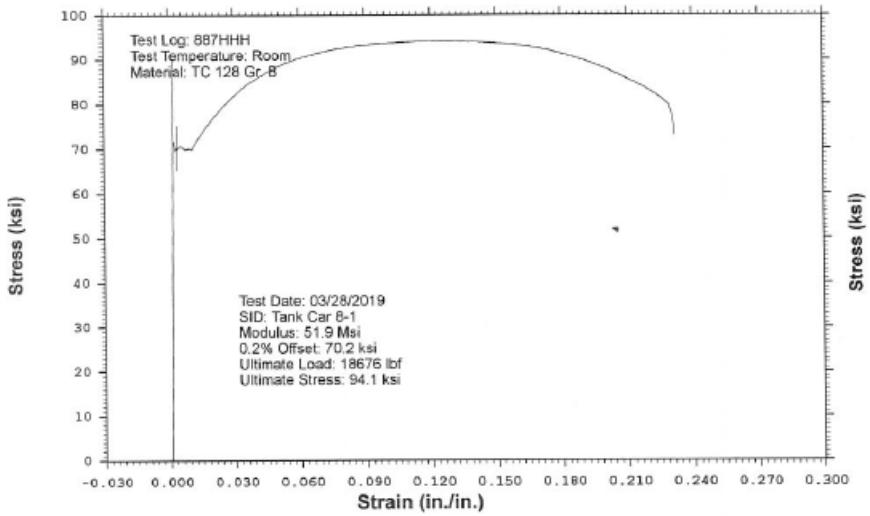

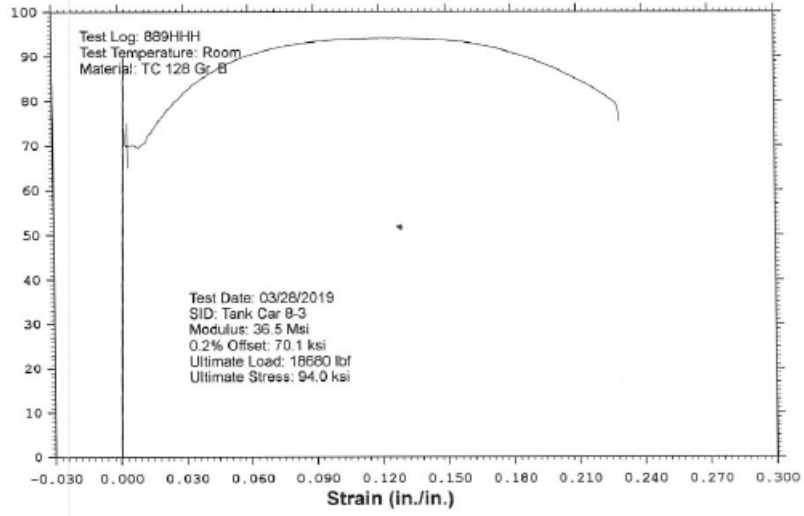

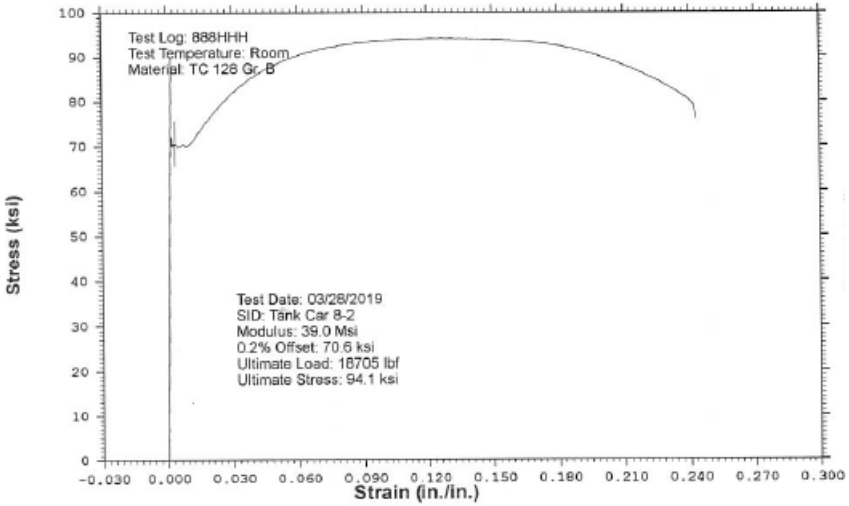

Appendix C.
Finite Element Analysis and Test Results

A CFC60 filter has been applied to the FEA and test acceleration data in accordance with SAE J211 (SAE International, 2007).

C1 – Pre-test FEA at Varied Speeds

Pre-test FEA was used to estimate the puncture range of the DOT-105 tank car used in this test. Because the actual material properties of the TC128 shell were unknown before the test, the pre-test models used TC128 material definitions based on DOT-105 tank cars used in two previous side impact tests (Test 2 and Test 6) (Kirkpatrick, S. W, 2010) (Carolan, M., & Rakoczy, P., 2019).

The impactor velocity initial condition in the simulations was incrementally changed in 0.5 mph increments for both the Test 2 TC128 model and the Test 6 TC128 model to estimate the puncture range for each material behavior. The Test 2 TC128 material definition resulted in an estimated puncture range of 10.5 to 11 mph, and the same FE model with a Test 6 TC128 material definition assigned to the shell resulted in an estimated puncture range of 8.5 to 9 mph.

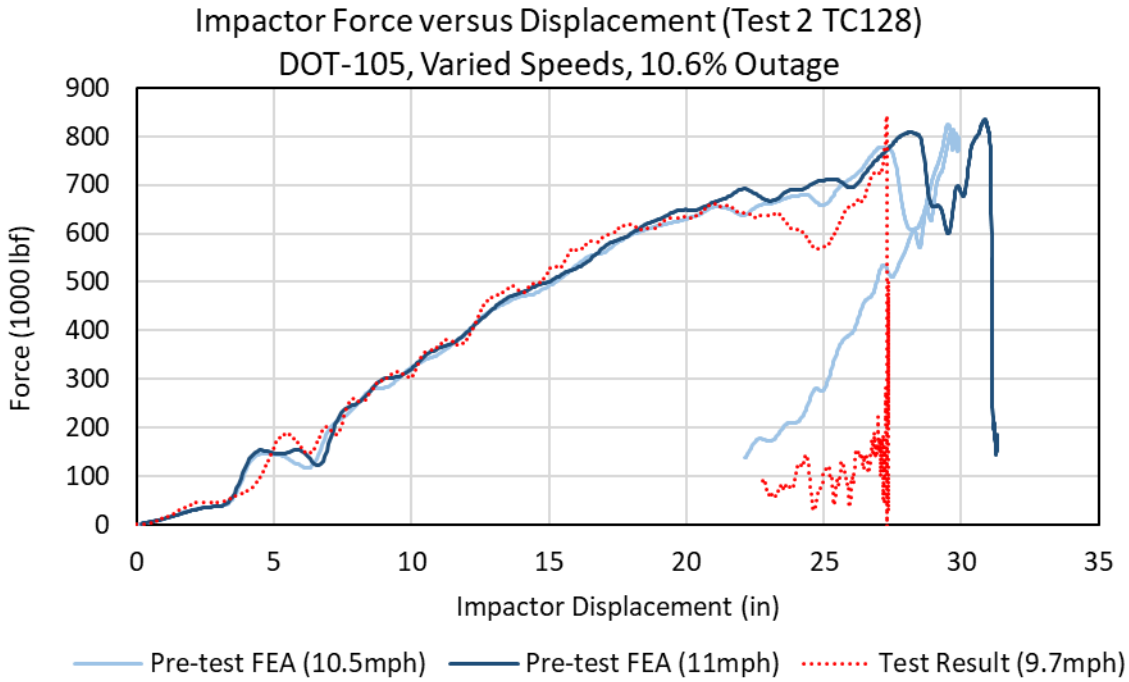

Figure C1. Impactor Force versus Displacement; Pre-test FEA (Test 2 TC128) and Test Results

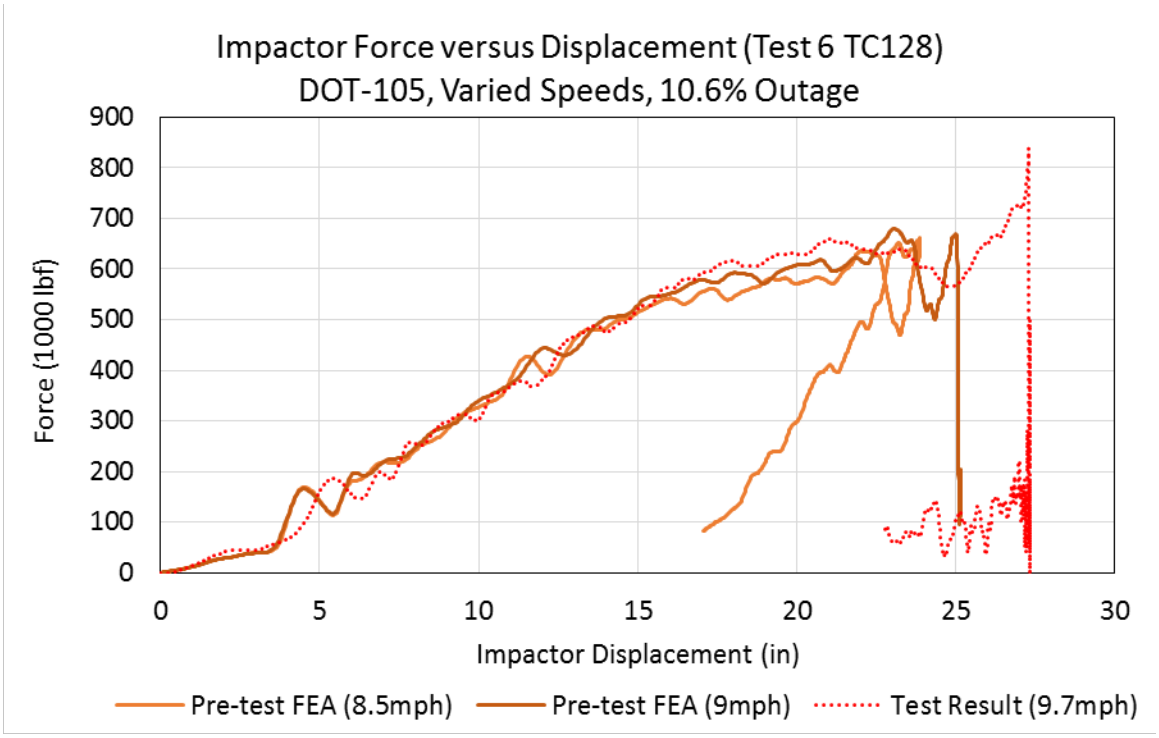

Figure C2. Impactor Force versus Displacement; Pre-test FEA (Test 6 TC128) and Test Results

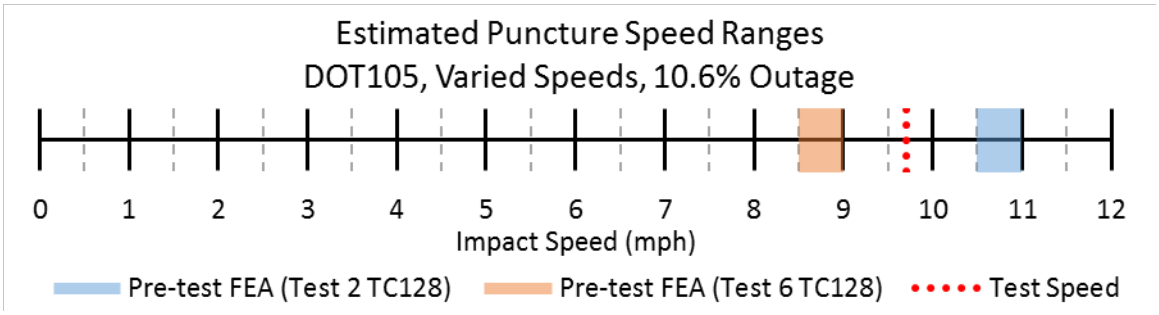

Figure C3. Estimated Puncture Speed Ranges from Pre-test FEA

C2 – Pre-Test FE Models Updated with Measured Test Speed

The initial impactor velocity in the pre-test FE models was updated with the measured test speed of 9.7 mph after the test. Because the actual material properties of the TC128 shell were unknown before the test, the pre-test models used TC128 material definitions based on two previous tests (Test 2 and Test 6). The simulation using the Test 6 TC128 material model experienced puncture and subsequently terminated at 0.225 seconds; subsequently, all the plots labeled as "Pre-test FEA (Test 6 TC128)" in this section are truncated at that time while the other results are shown up to a time of 0.4 seconds.

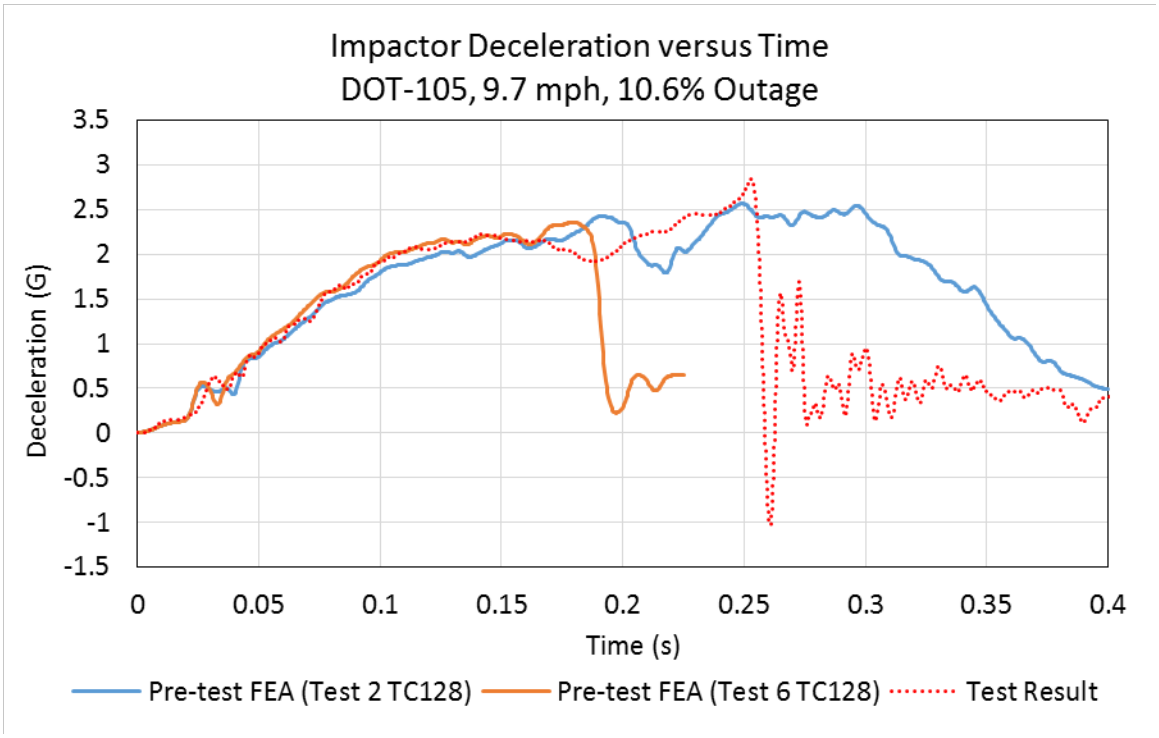

Figure C4. Impactor Deceleration versus Time; Pre-test FEA and Test Results

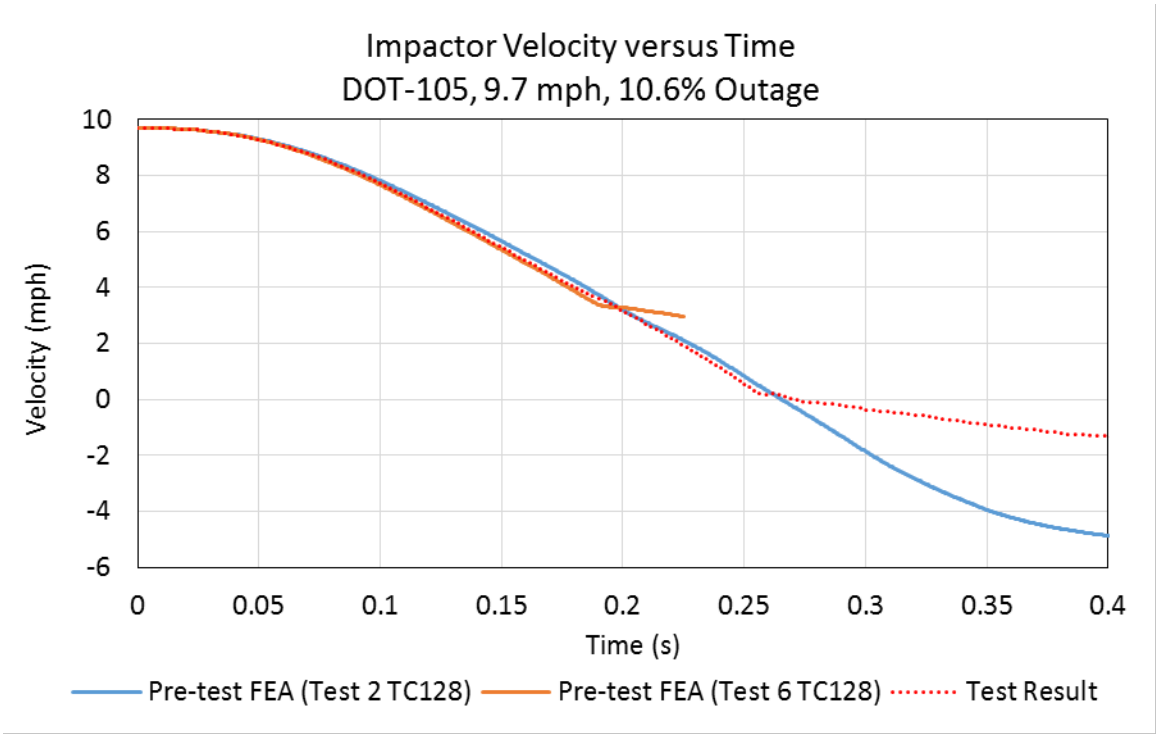

Figure C5. Impactor Velocity versus Time; Pre-test FEA and Test Results

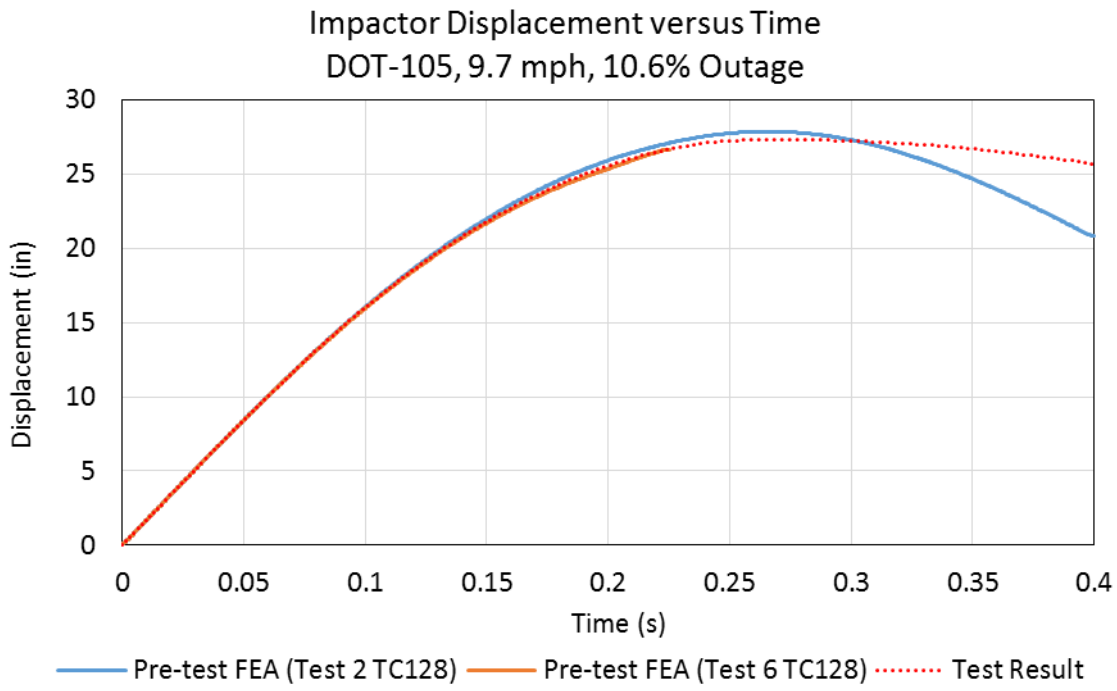

Figure C6. Impactor Displacement versus Time; Pre-test FEA and Test Results

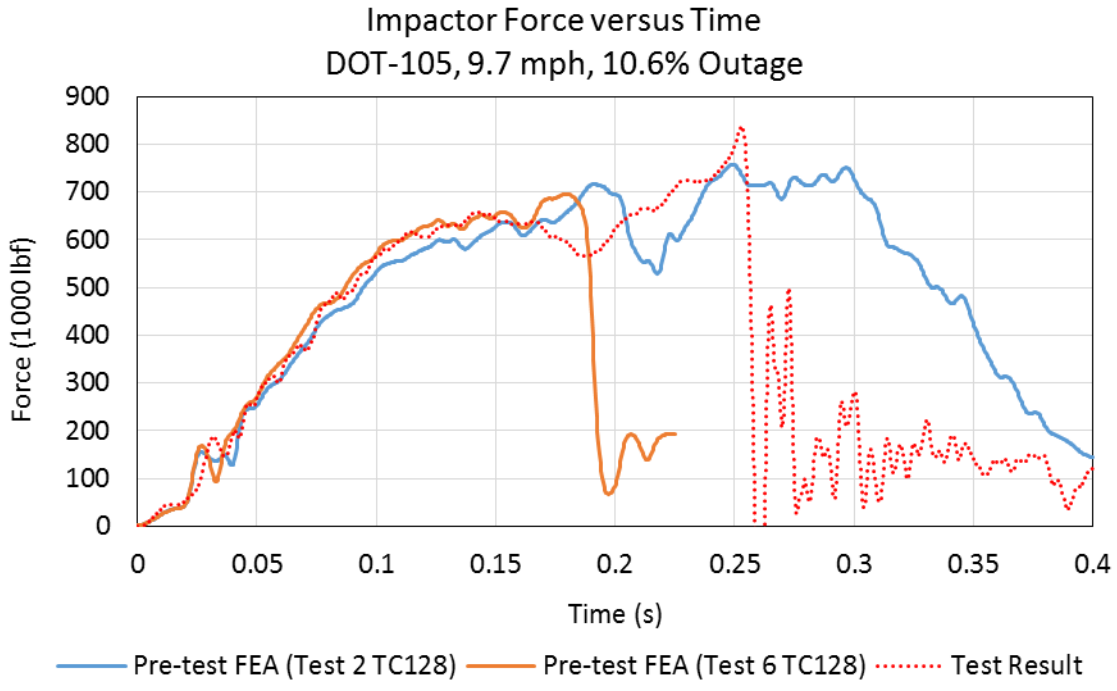

Figure C7. Impactor Force versus Time; Pre-test FEA and Test Results

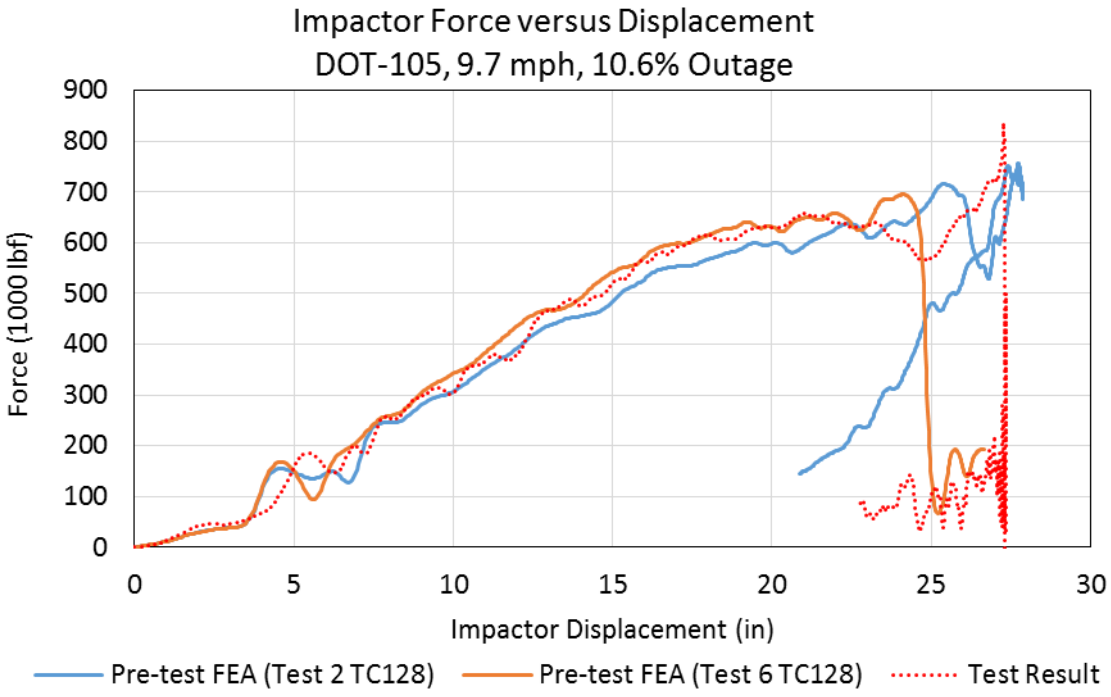

Figure C8. Impactor Force versus Displacement; Pre-test FEA and Test Results

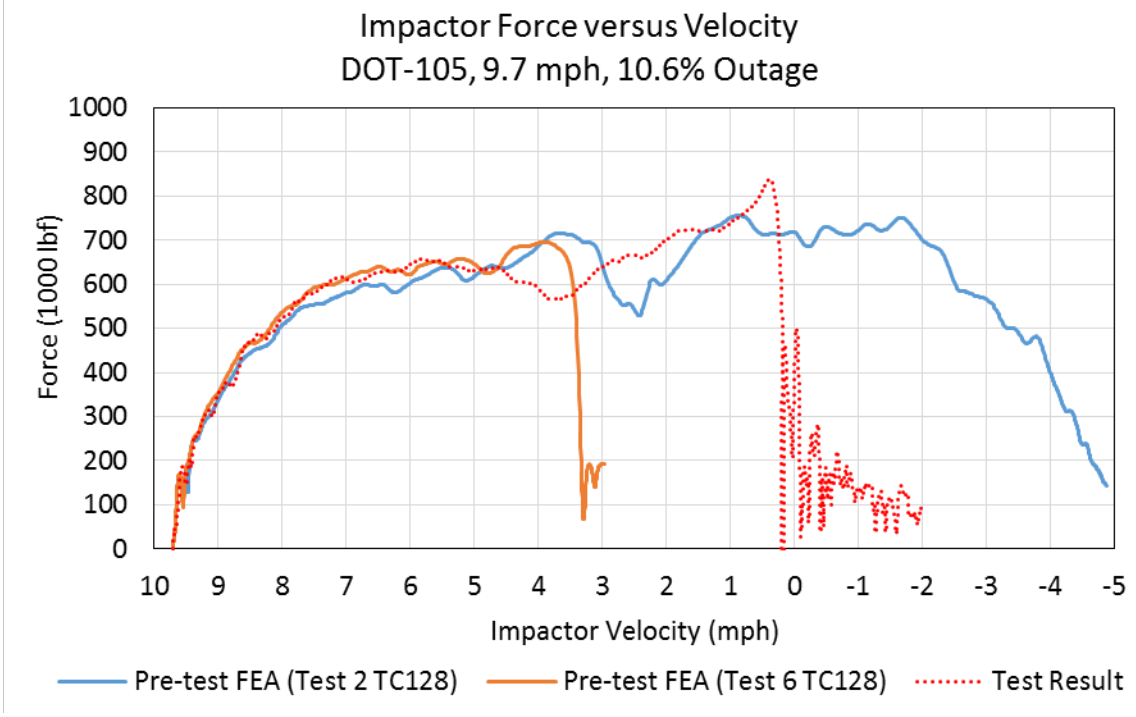

Figure C9. Impactor Force versus Velocity; Pre-test FEA and Test Results

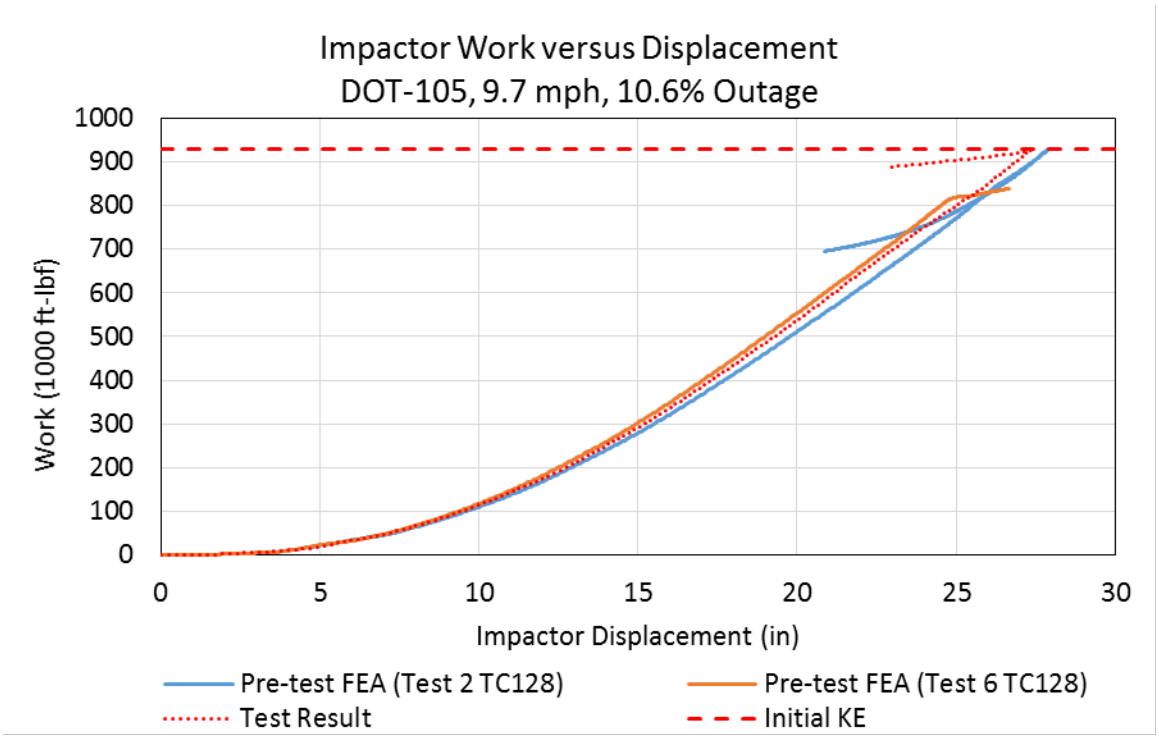

Figure C10. Impactor Work versus Displacement; Pre-test FEA and Test Results (initial kinetic energy (KE) of impactor in model is 9.3×10^5 ft-lbf)

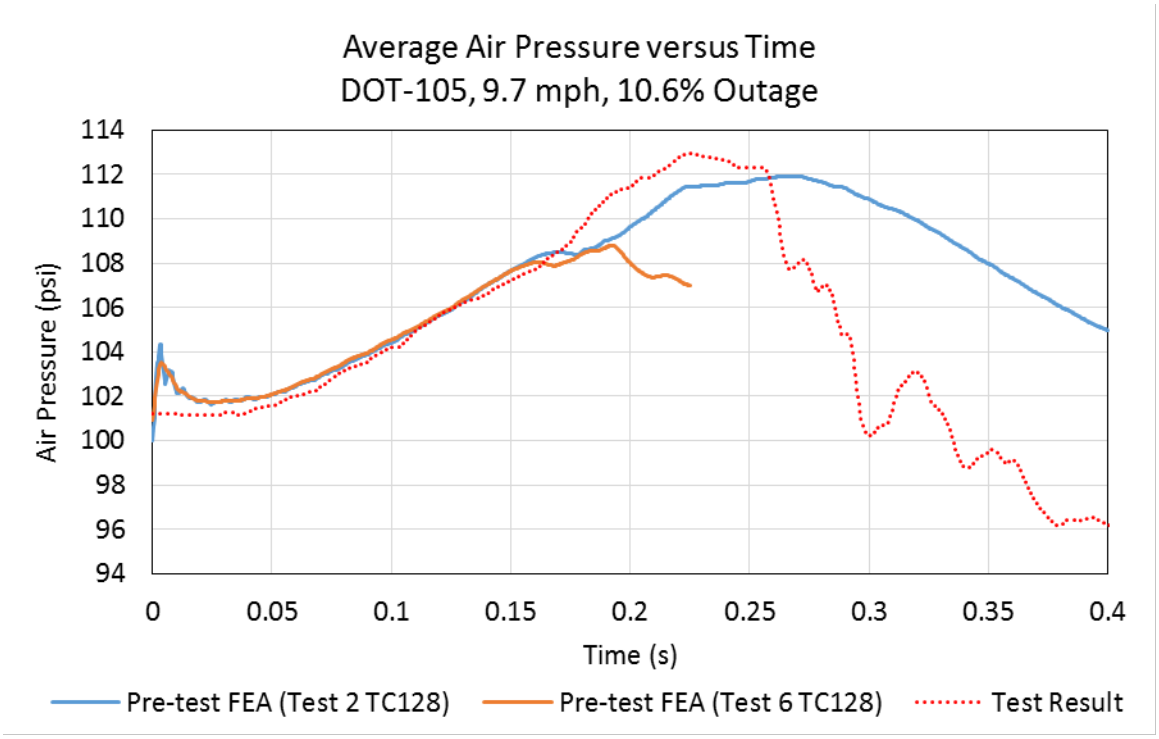

Figure C11. Average Air Pressure versus Time; Pre-test FEA and Test Results

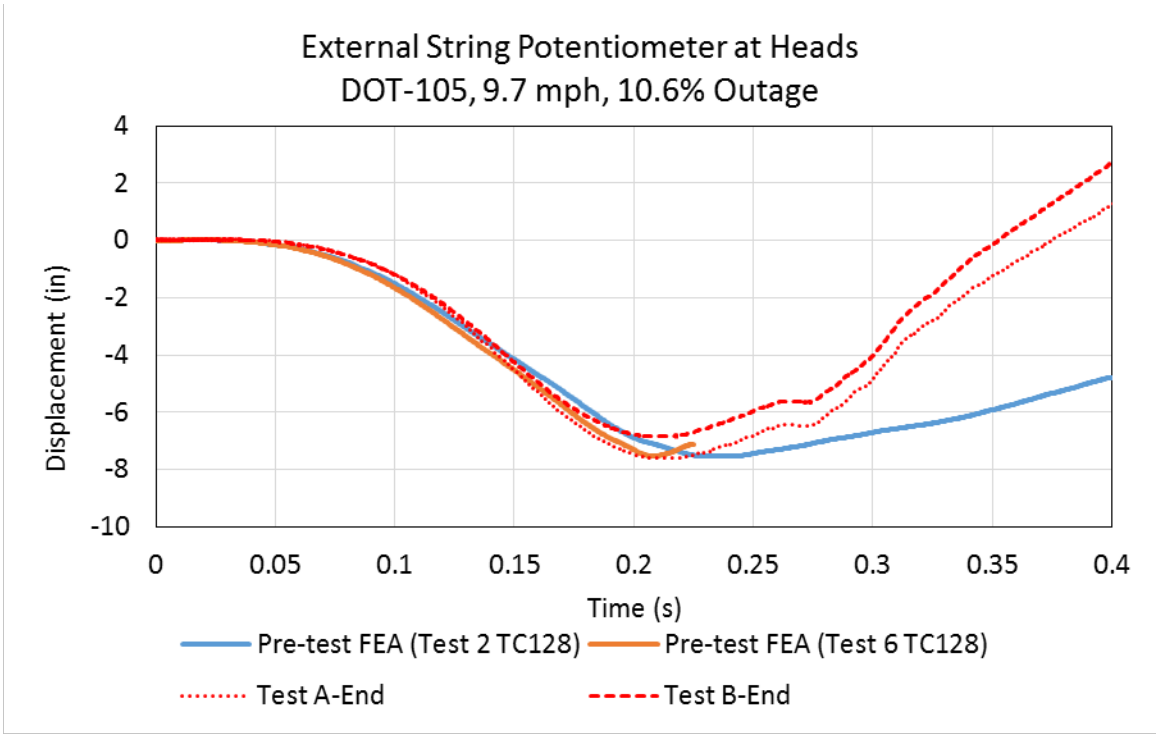

Figure C12. External String Potentiometers at Heads; Pre-test FEA and Test Results

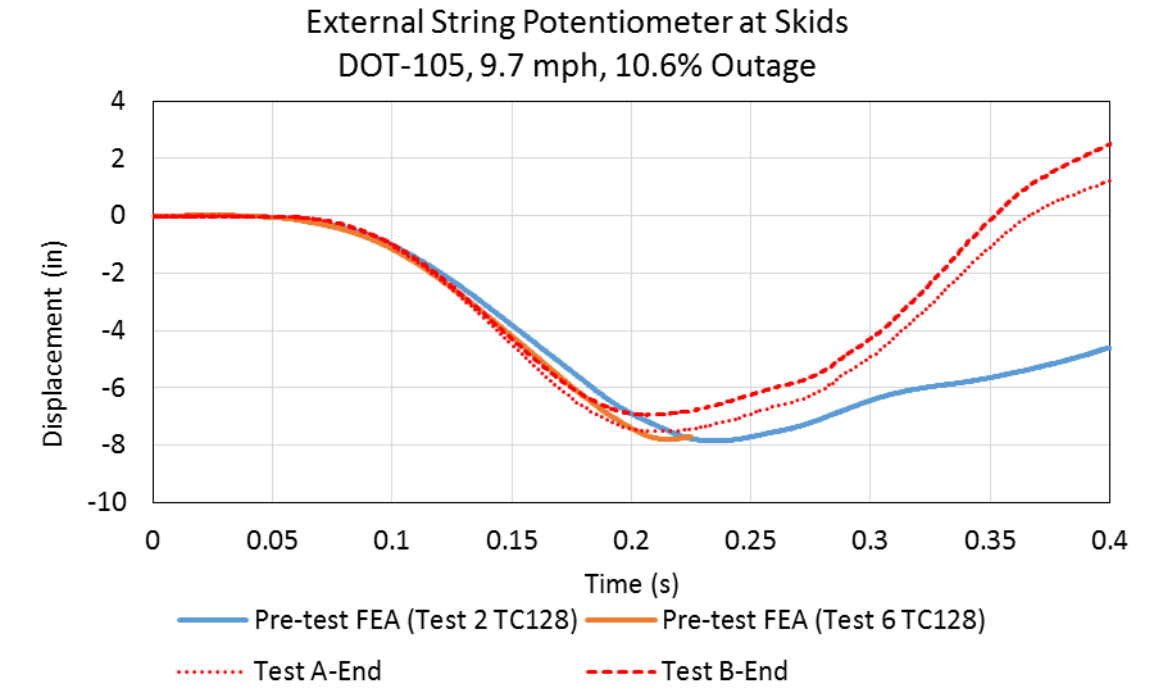

Figure C13. External String Potentiometers at Skids; Pre-test FEA and Test Results

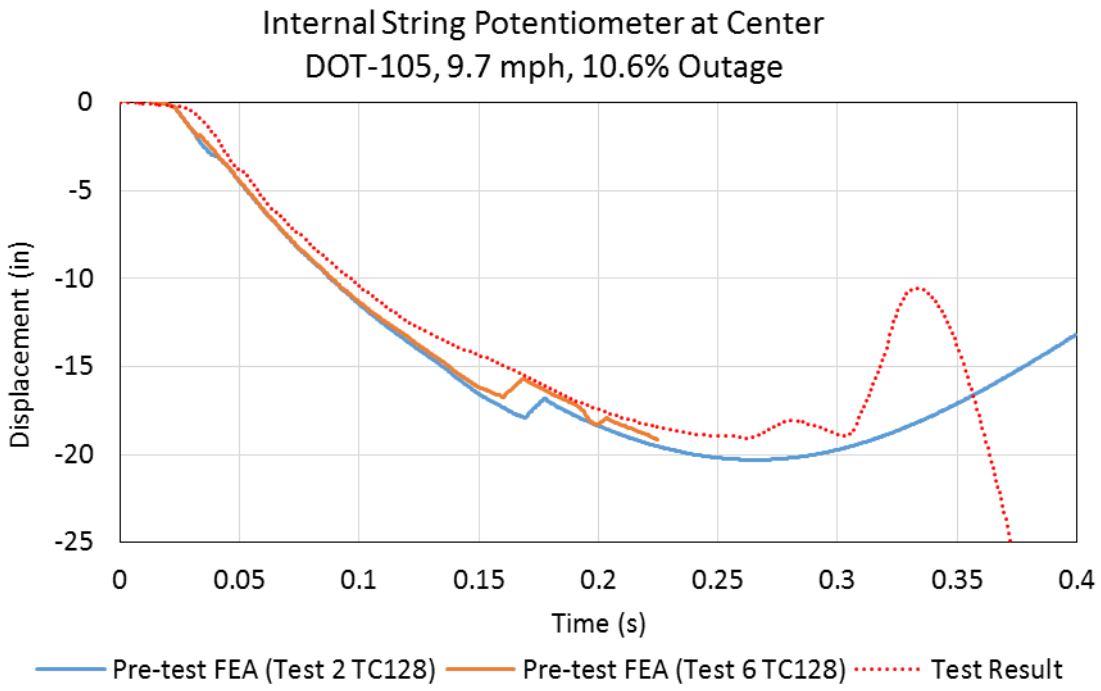

Figure C14. Internal String Potentiometer at Center of Tank; Pre-test FEA and Test Results

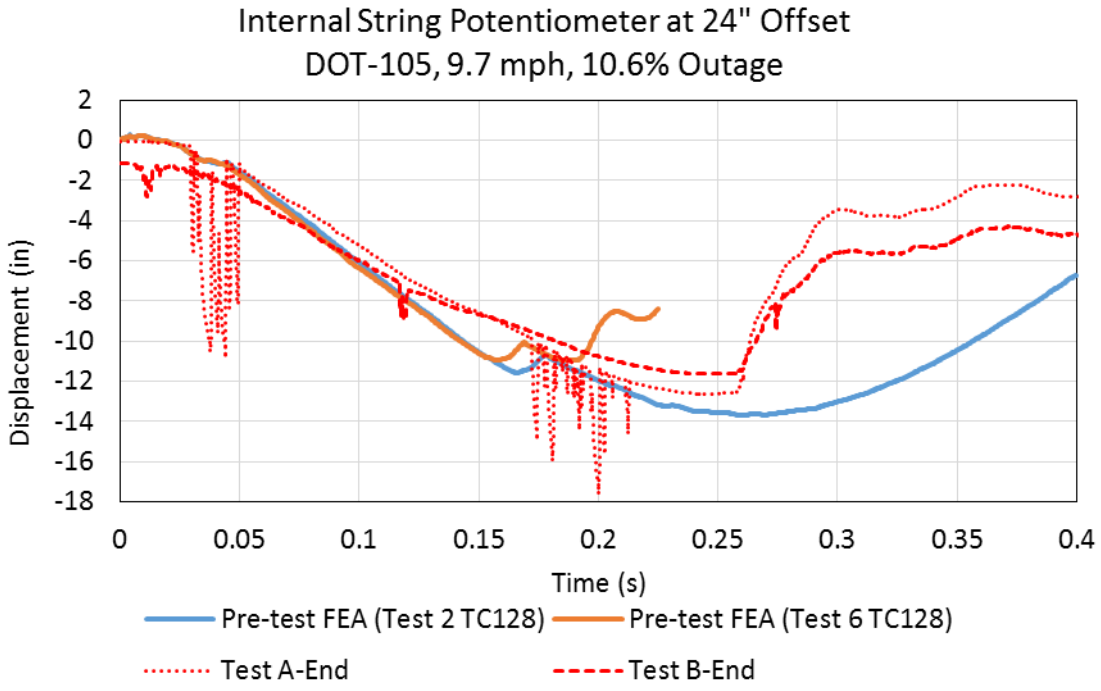

Figure C15. Internal String Potentiometers at 24-inch Offset; Pre-test FEA and Test Results

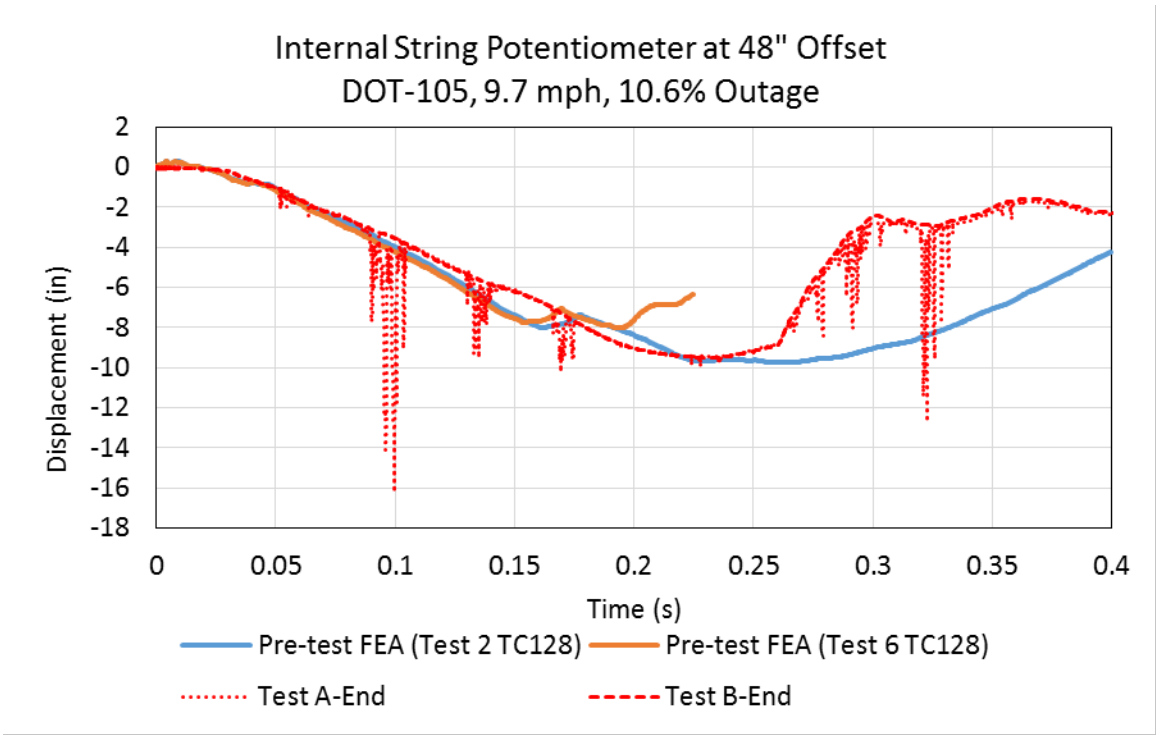

Figure C16. Internal String Potentiometers at 48-inch Offset; Pre-test FEA and Test Results

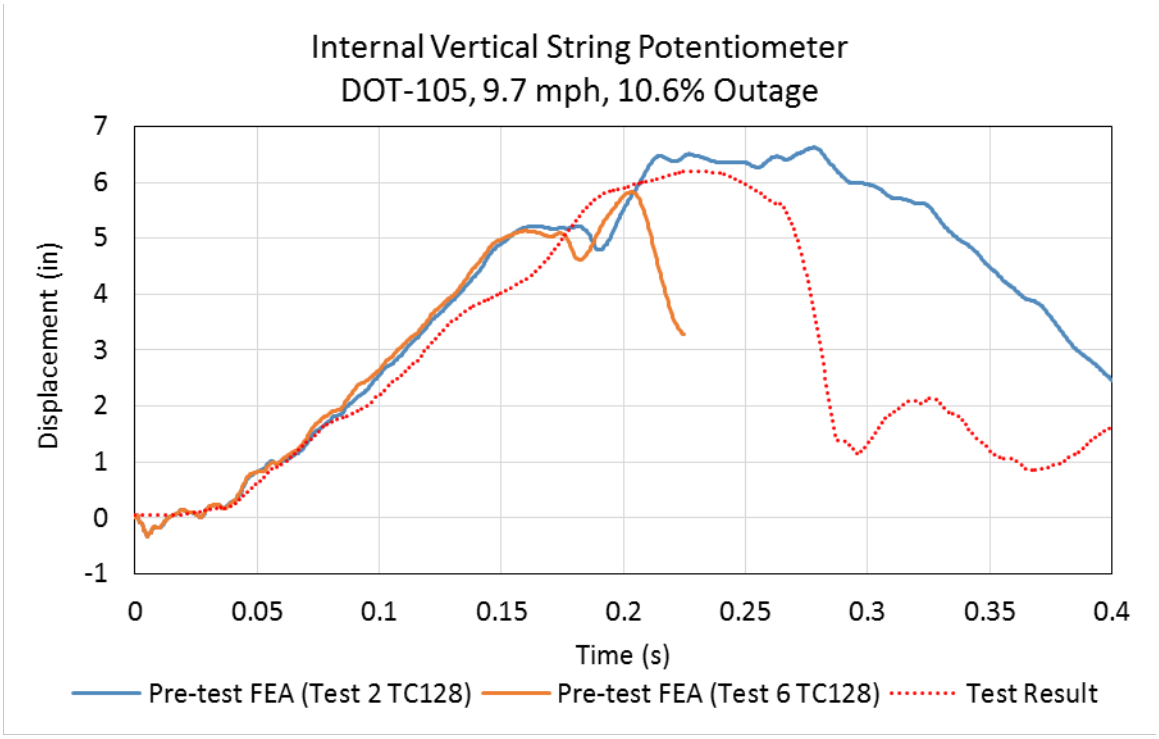

Figure C17. Internal Vertical String Potentiometer; Pre-test FEA and Test Results

C3 – Post-Test FEA and Test Results

Post-test FEA was run at the speed determined from the speed traps during the test, 9.7 mph. The post-test FE model was updated with the material behavior of the TC128 steel in the tank shell and the weight of the ram car was increased from the pre-test estimated value of 295,000 pounds to the measured test value of 296,775 pounds.

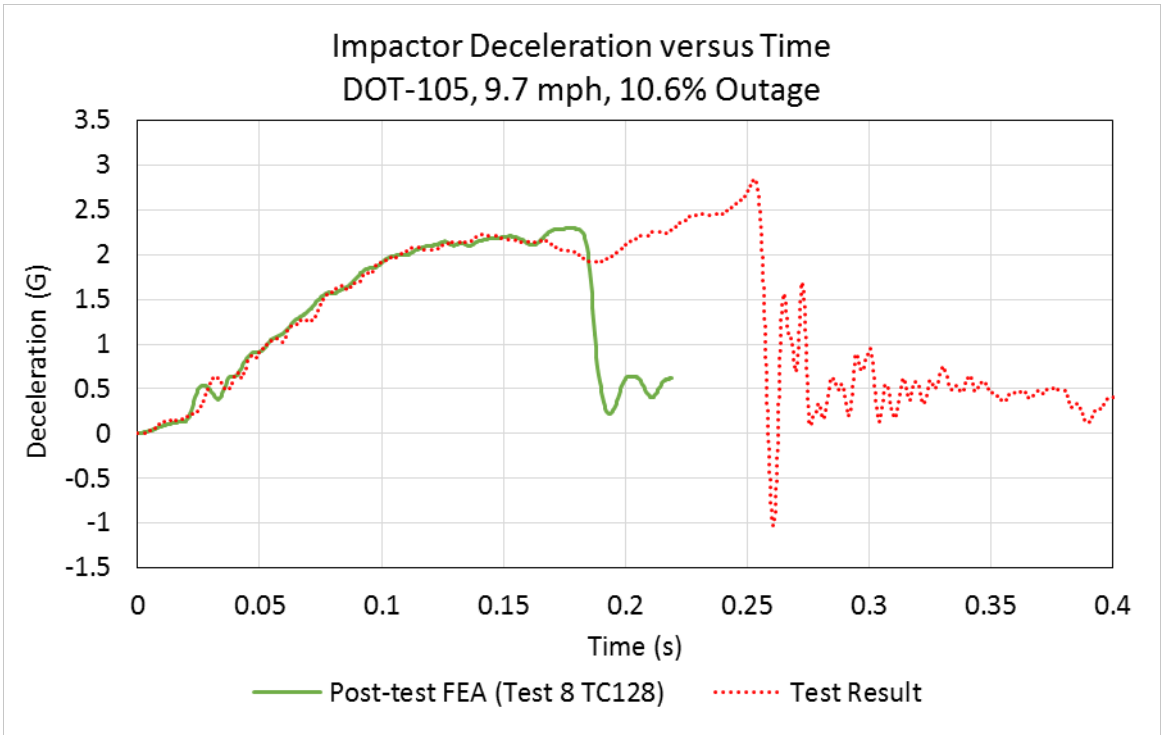

Figure C18. Impactor Deceleration versus Time; Post-Test FEA and Test Results

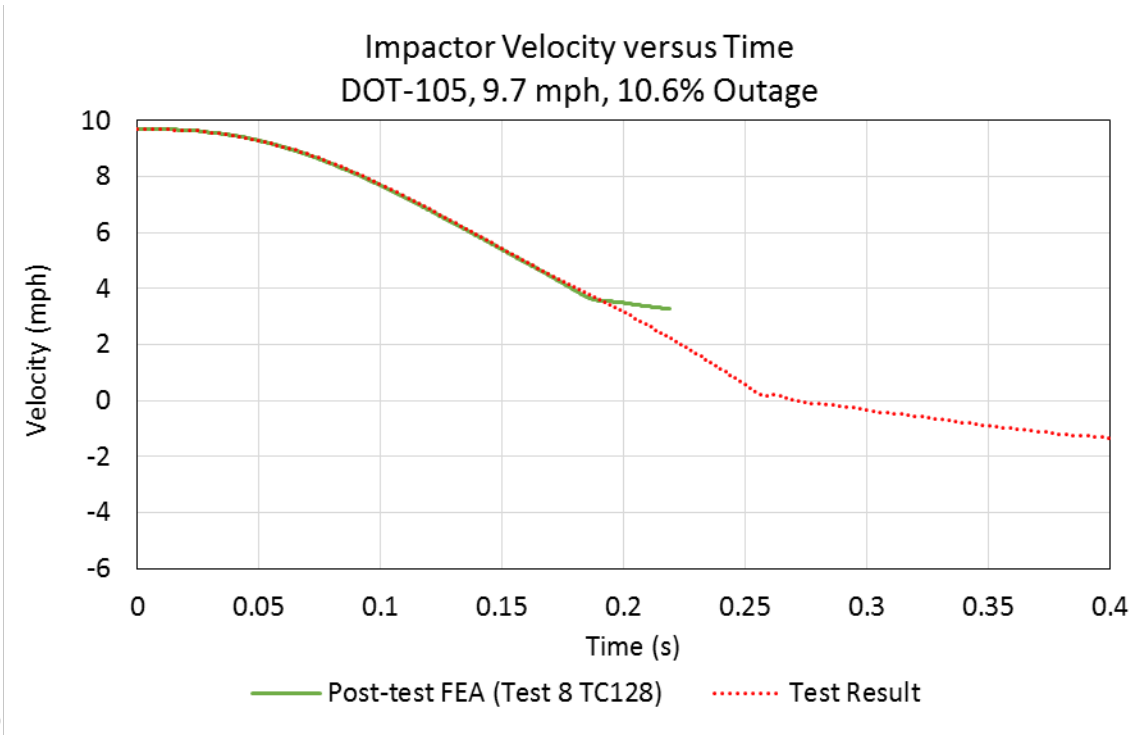

Figure C19. Impactor Velocity versus Time; Post-Test FEA and Test Results

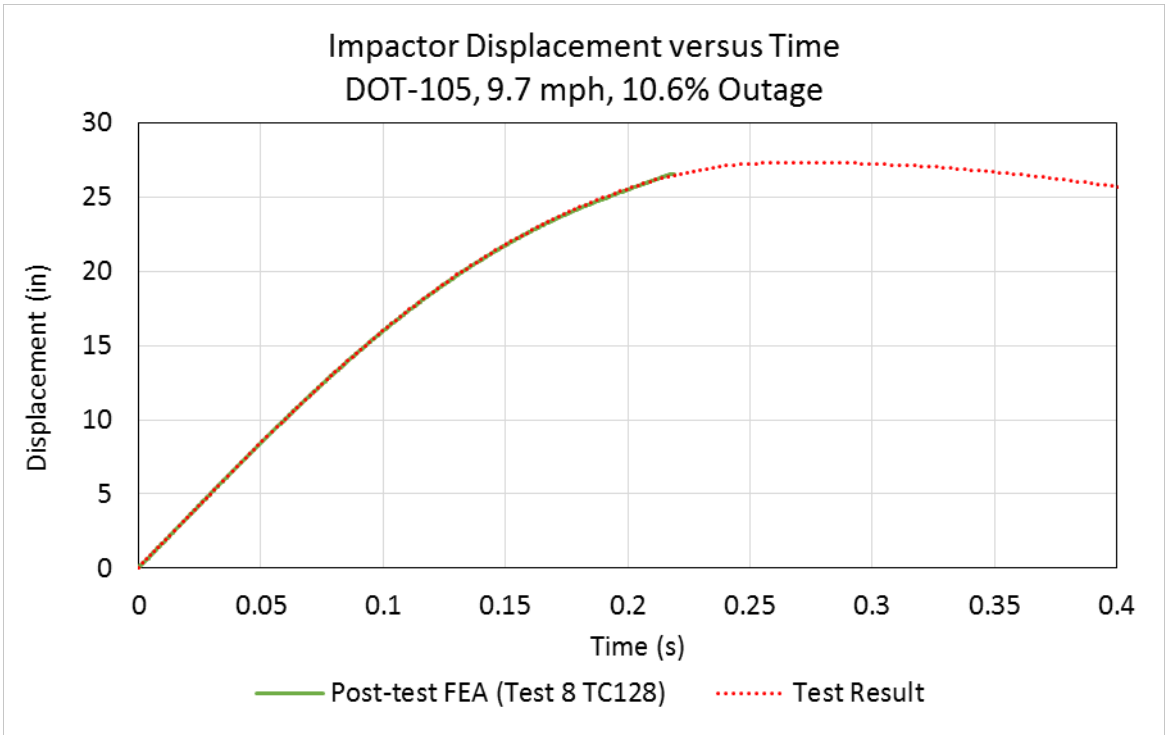

Figure C20. Impactor Displacement versus Time; Post-Test FEA and Test Results

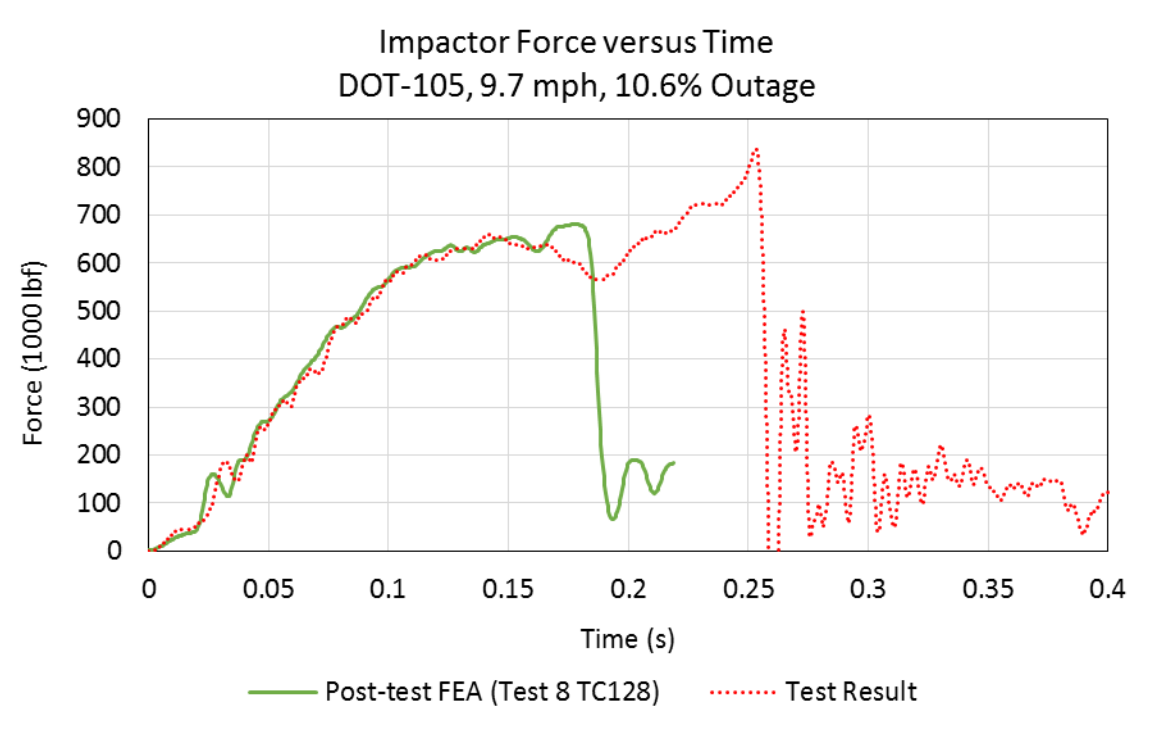

Figure C21. Impactor Force versus Time; Post-Test FEA and Test Results

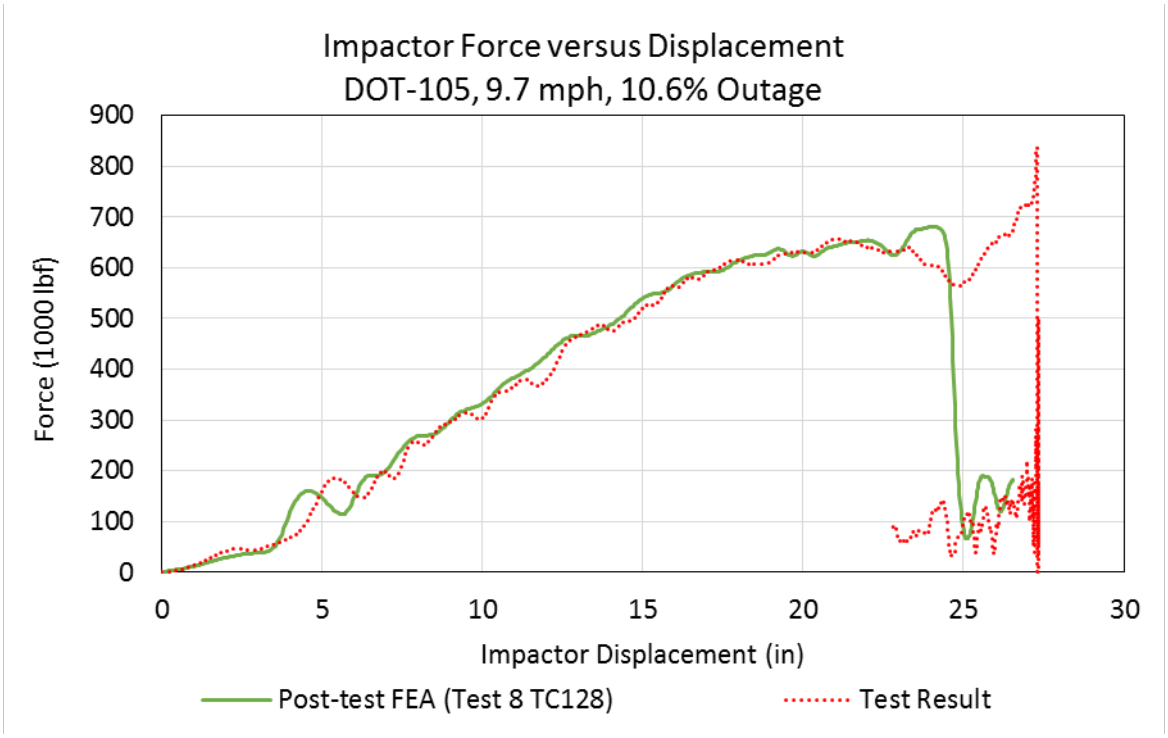

Figure C22. Impactor Force versus Displacement; Post-Test FEA and Test Results

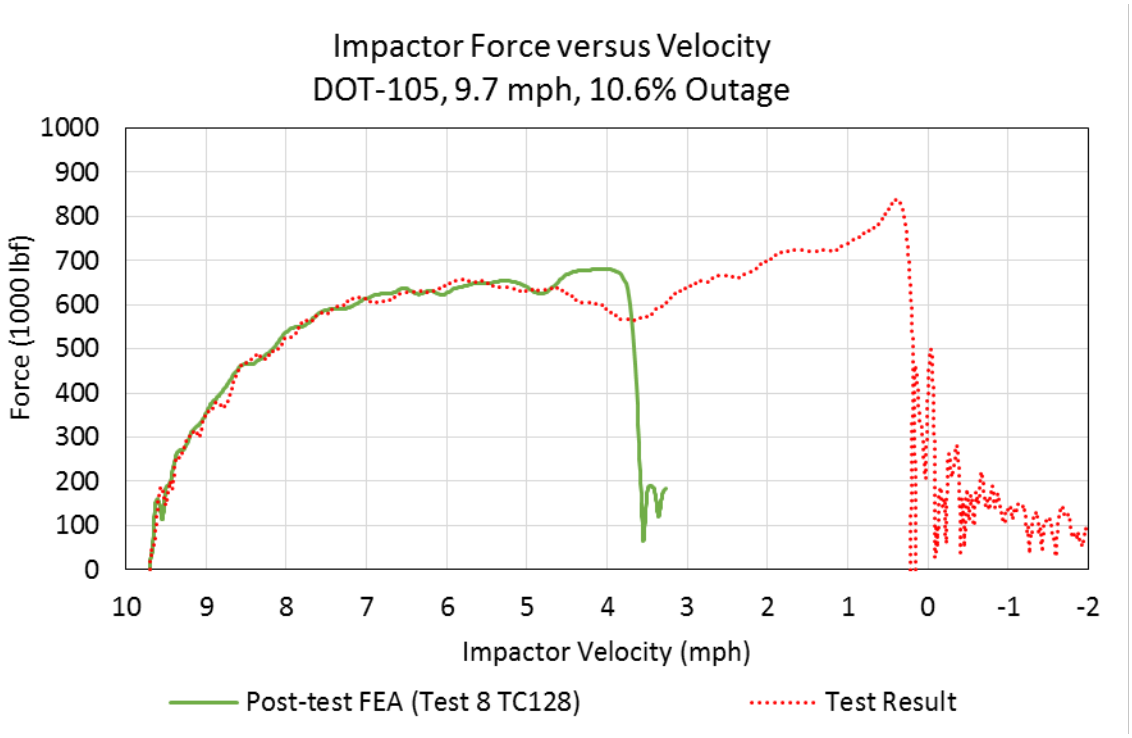

Figure C23. Impactor Force versus Velocity; Post-Test FEA and Test Results

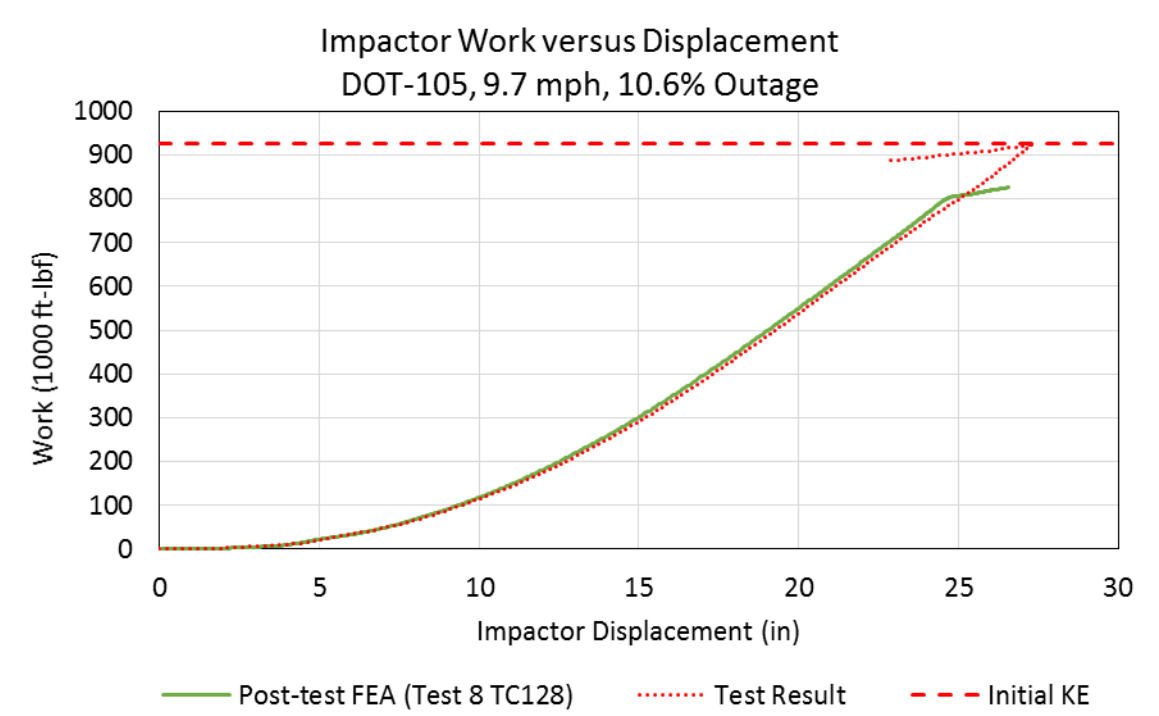

Figure C24. Impactor Work versus Displacement; Post-Test FEA and Test Results (initial KE of impactor in model is 9.3×10^5 ft-lbf)

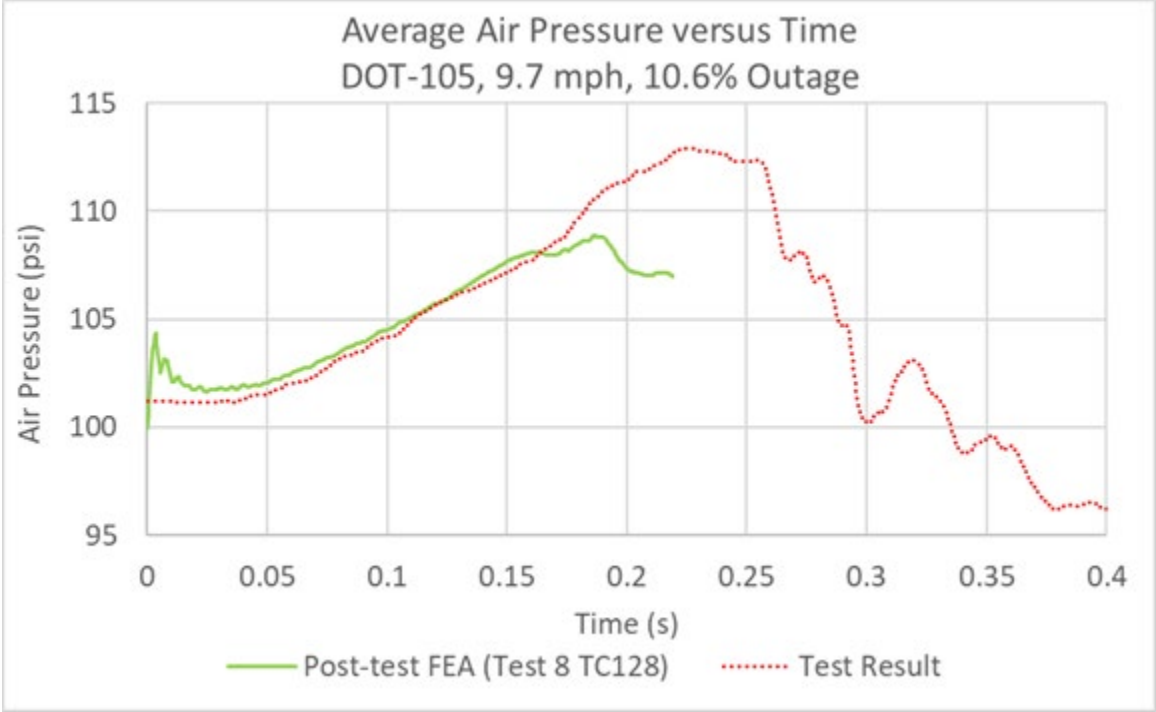

Figure C25. Average Air Pressure versus Time; Post-Test FEA and Test Results

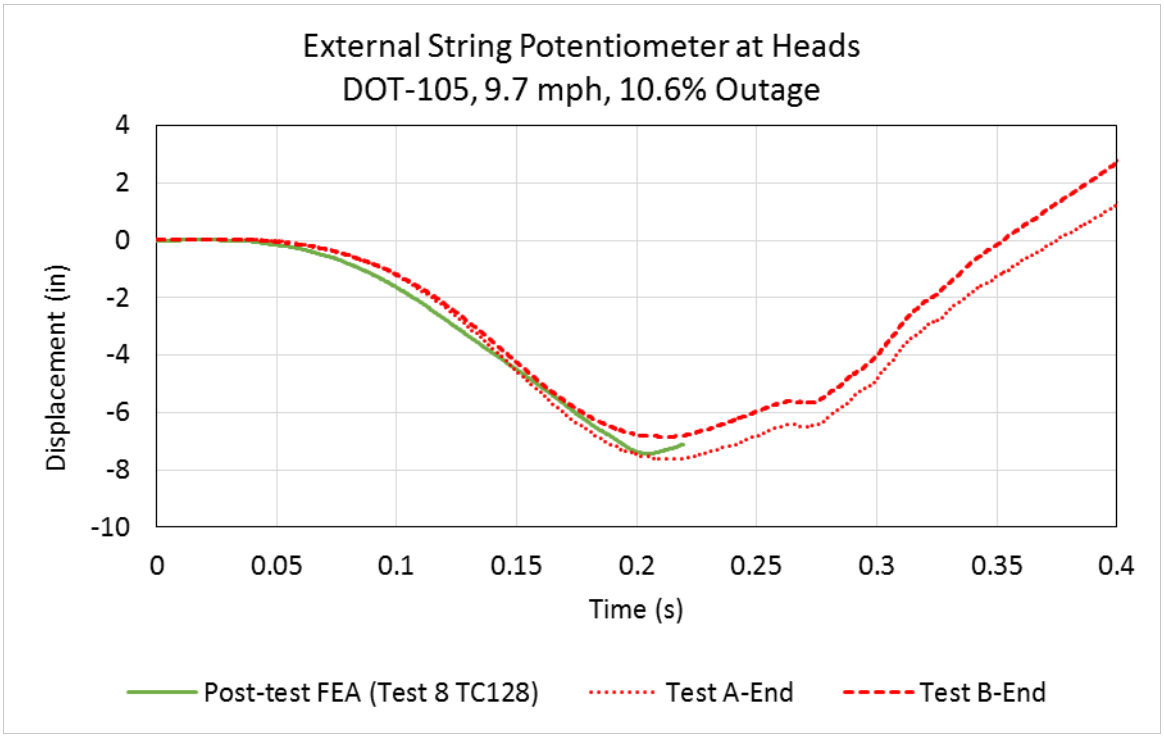

Figure C26. External String Potentiometers at Heads; Post-Test FEA and Test Results

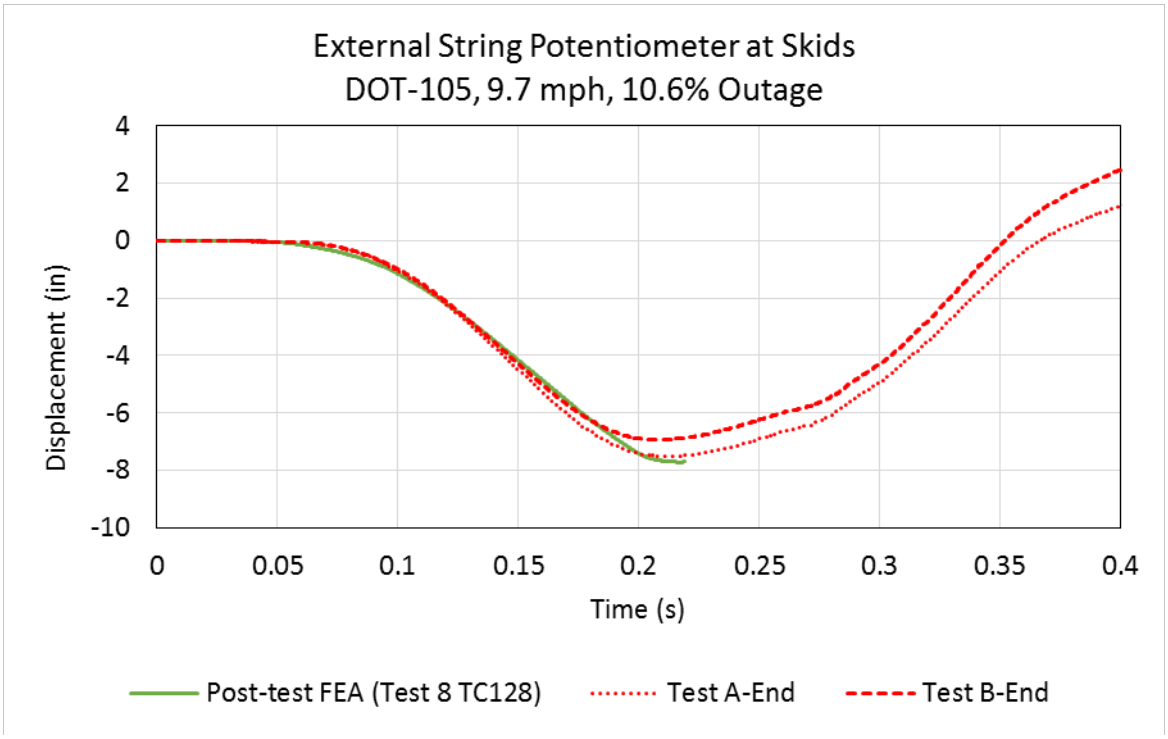

Figure C27. External String Potentiometers at Skids; Post-Test FEA and Test Results

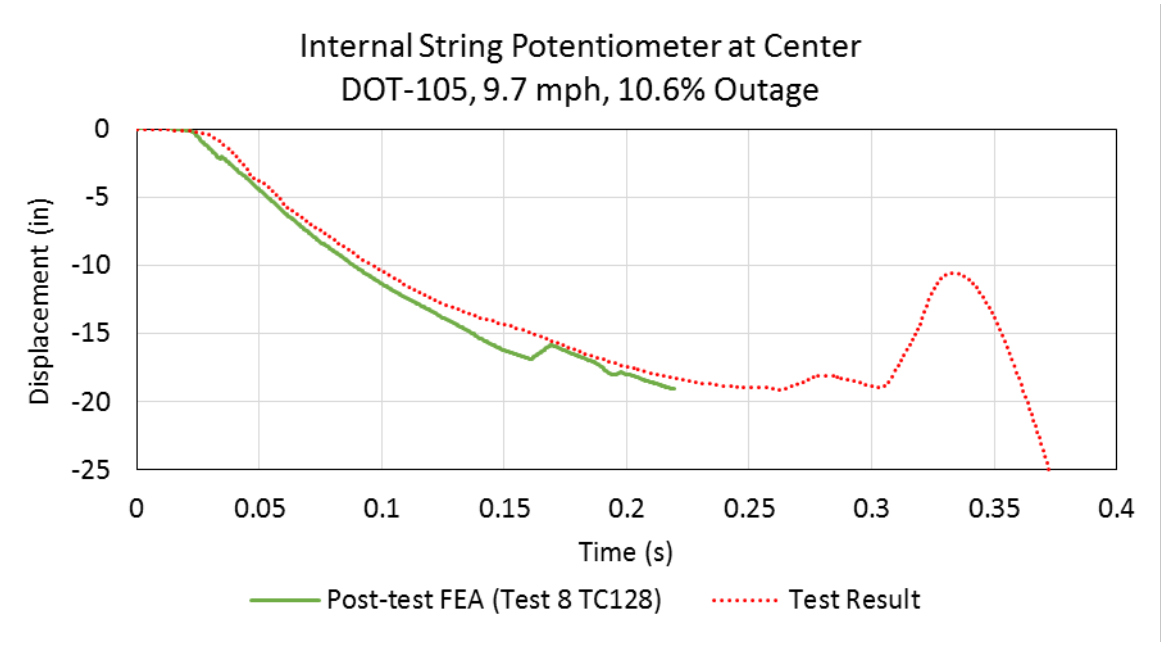

Figure C28. Internal String Potentiometer at Center of Tank; Post-Test FEA and Test Results

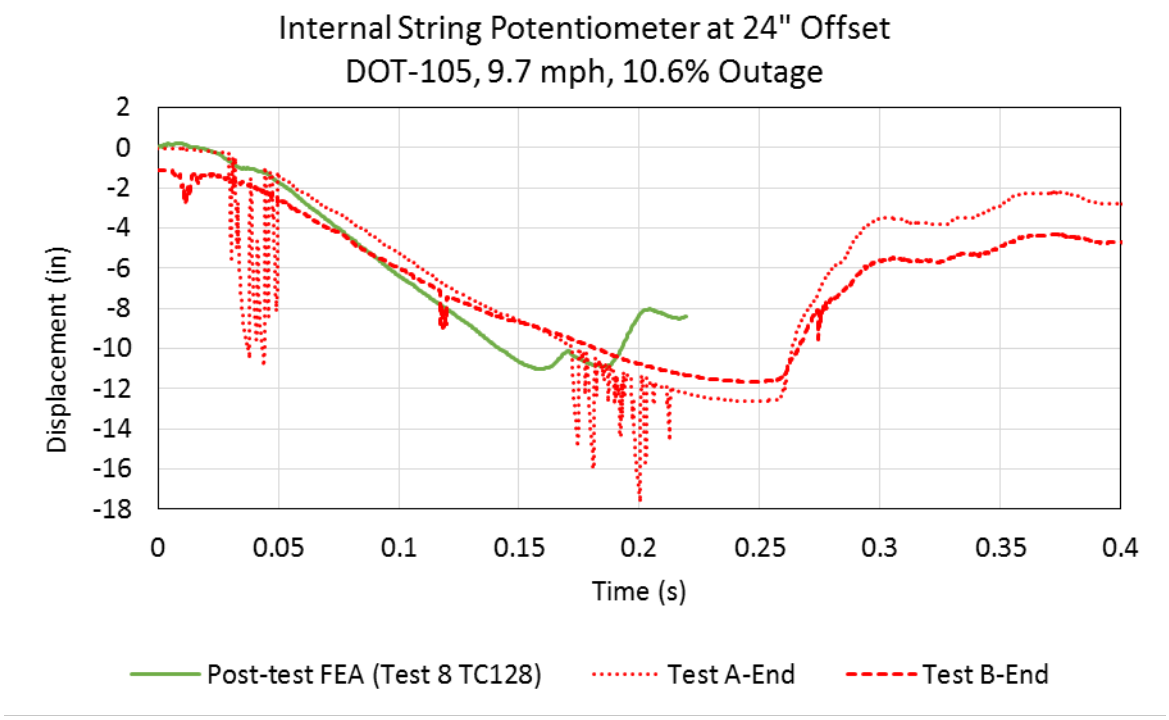

Figure C29. Internal String Potentiometers at 24-inch Offset; Post-Test FEA and Test Results

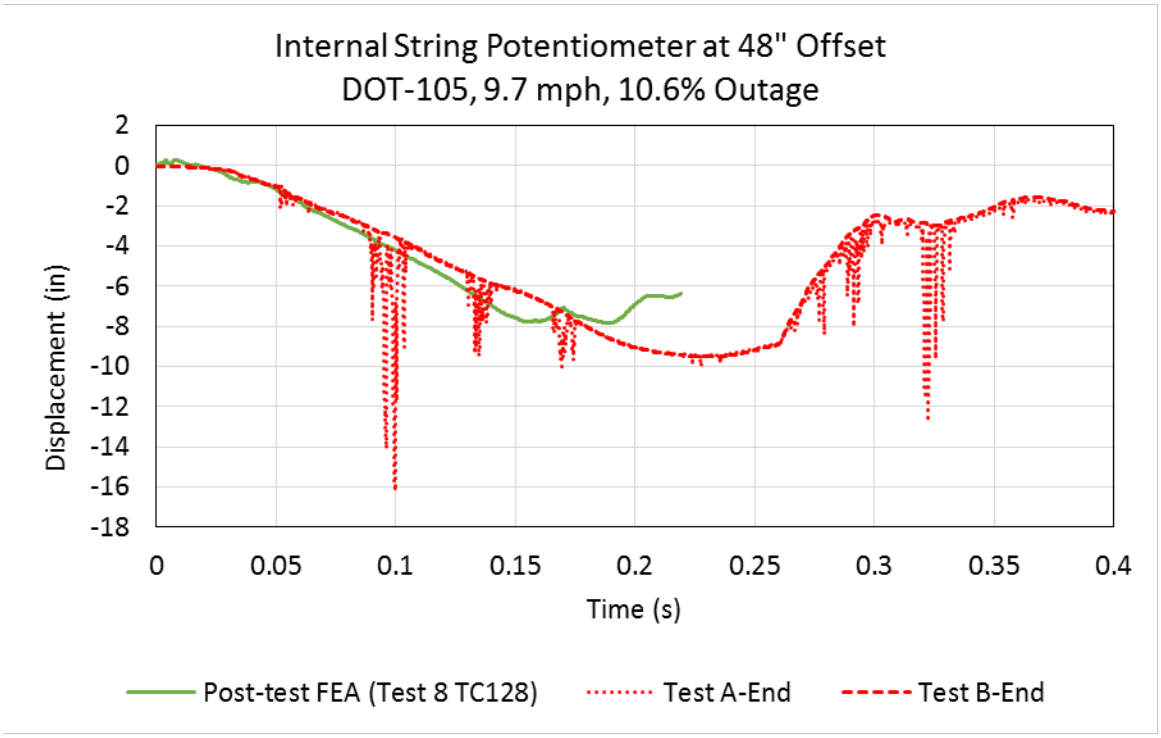

Figure C30. Internal String Potentiometers at 48-inch Offset; Post-Test FEA and Test Results

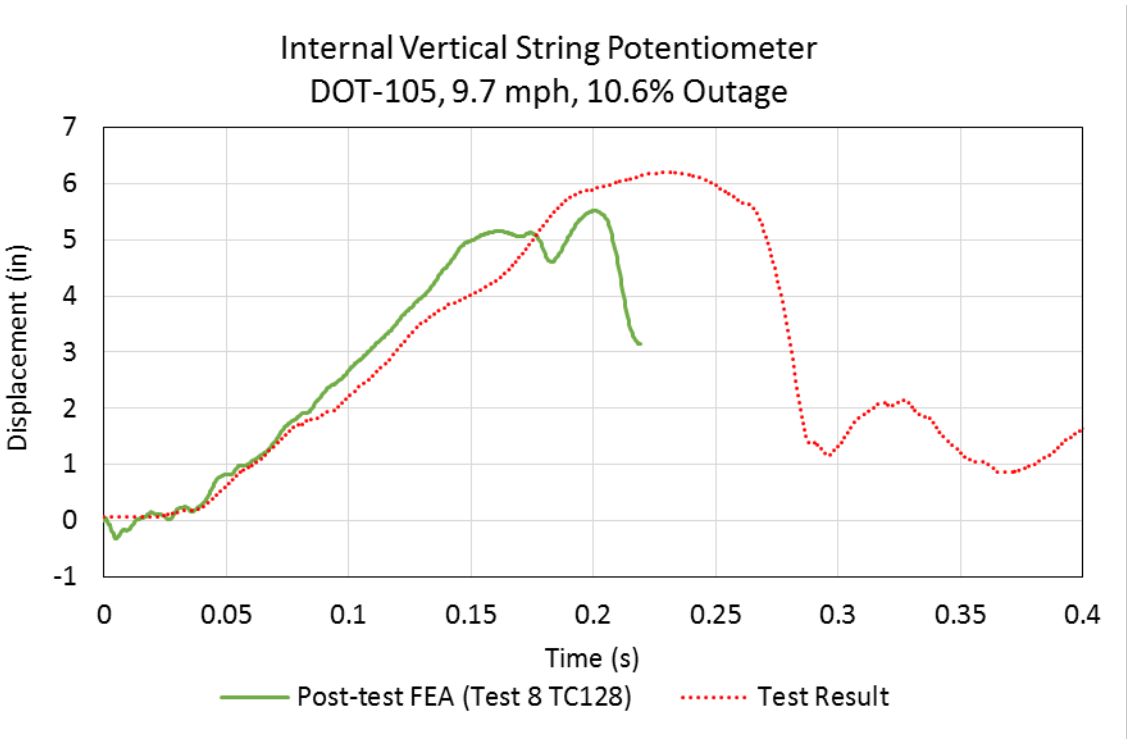

Figure C31. Internal Vertical String Potentiometer; Pre-Test FEA and Test Results

Appendix D.
Geometry in Pre-Test and Post-Test Finite Element Models

The following information discusses each of the parts making up each FE model. Note that for parts that are bisected by the symmetry plane, the values reported in the following tables for mass and number of elements correspond to what was included in the FE model (i.e., half the mass and half the size of the physical body during the test).

Rigid parts were used when it was important to include a part for its inertia or for its interaction through contact, but where the deformation of the part could be neglected in the calculations. Four parts were modeled as rigid bodies. The remaining bodies were modeled as deformable bodies.

A summary of the element types used to mesh the model assembly is provided in Table D1.

Table D1. Summary of Abaqus Explicit Element Types (Dassault Systemes Simulia Corp, 2014)

Element Name	Description
C3D8	8-node linear brick element for stress and displacement modeling
CONN3D2	Connector element between two nodes or ground and a node
DCOUP3D	Three-dimensional distributing coupling element
M3D3	3-node triangular membrane element
M3D4R	4-node quadrilateral membrane element (reduced integration)
MASS	Point mass
R3D3	3-dimensional, 3-node triangular facet rigid element
R3D4	3-dimensional, 4-node bilinear quadrilateral rigid element
RNODE3D	3-dimensional reference node
S3R	3-node triangular general-purpose shell, finite membrane strains (identical to element S3)
S4	4-node general-purpose shell, finite membrane strains
S4R	4-node general-purpose shell, reduced integration with hourglass control, finite membrane strains
SPRINGA	Axial spring between two nodes, whose line of action is the line joining the two nodes. This line of action may rotate in large-displacement analysis.

D1 – Rigid Impactor

The impactor was modeled as a rigid body in the side impact puncture simulations with the DOT-105 tank car. The simulations used a 6-inch by 6-inch square impactor with 0.5-inch radii edges around the impact face. The geometry included the impact face and the tapered cone back to the portion of the impactor where the impactor attached to the ram car. Because only the impactor itself was modeled and this model used one-half symmetry, half of the mass of the entire ram car was assigned to the reference node on the impactor. Figure D1 shows the geometry and mesh of the impactor, and its properties are given in Table D2.

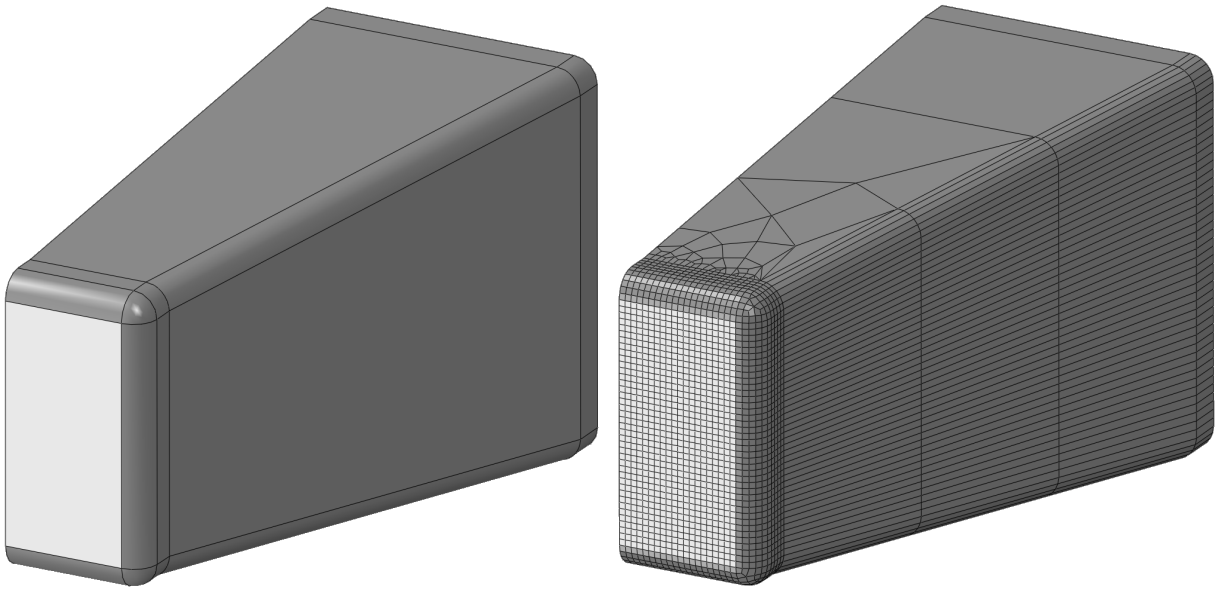

Figure D1. Impactor Geometry (left) and Mesh (right)

Table D2. Properties of Impactor in FE Model

	Pre-Test Model	Post-Test Model
Type of Part	Rigid	Rigid
Number of Elements	R3D4: 1,981	R3D4: 1,981
Number of Elements	R3D3: 26	R3D3: 26
Number of Elements	MASS: 1	MASS: 1
Part Weight	147,563 lbf	148,507 lbf

D2 – Rigid Wall

The rigid wall was modeled as a rigid body in the side impact puncture simulations with the DOT-105 tank car. Because the wall was constrained against motion in any direction, no mass needed to be defined for this part. Figure D2 shows the geometry and mesh of the rigid wall, and its properties are given in Table D3.

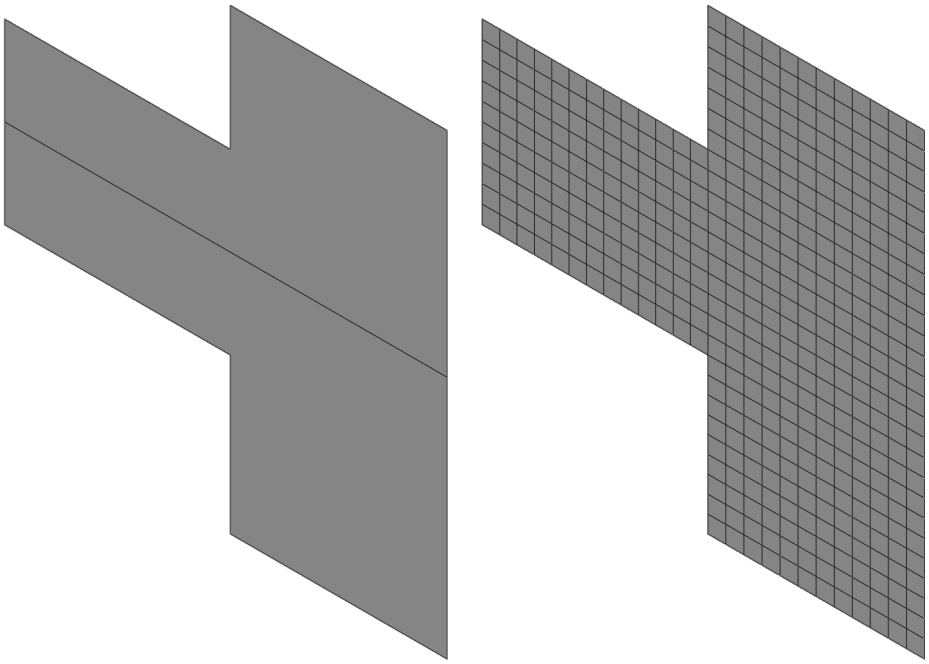

Figure D2. Rigid Wall Geometry (left) and Mesh (right)

Table D3. Properties of Rigid Wall in FE Model for Pre- and Post-Test Models

Type of Part	Rigid
Number of Elements	R3D4: 442

D3 – Rigid Skid

The trucks of the tank car were removed prior to the test. The bolster of the car rested directly upon a set of skids, which themselves rested upon steel plates (see Section 2.2). The skids were designed to inhibit rigid-body roll of the tank car following rebound from the rigid wall during a test. Figure D3 shows the skid geometry and mesh. Note that since this part exists entirely to one side of the symmetry plane, the mass and geometric properties correspond to the actual mass and geometry of one full skid. Table D4 is a summary of the properties of the skid used in the FE model.

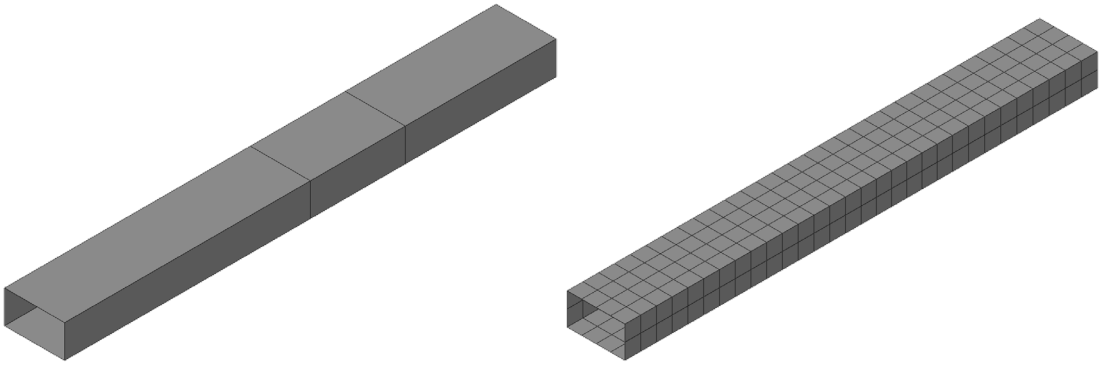

Figure D3. Skid Geometry (left) and Mesh (right)

Table D4. Properties of Skid in FE Model for Pre- and Post-Test Models

Type of Part	Rigid
Number of Elements	R3D4: 360
Number of Elements	MASS: 2

The skids used in the test weigh approximately 3,500 pounds each. This mass was included in the model through the use of a point mass at the rigid body reference node of each skid. Since the FE model is a simplified representation of the tank, the model does not include such geometric details as the bolsters, draft sills, draft gear, or couplers, as these features are not expected to play a significant role in the puncture response for an impact near the center of the shell. The masses of these components are included as a second point mass on the skid. For this tank car, the additional structure at each end of the car was assumed to have a weight of approximately 7,700 pounds. These additional point masses were added to both the pre-test and post-test models without adjustment. Table D5 is a summary of the added point masses.

Table D5. Point Masses Added to Skid Reference Point in Models

Component	**Approximate Weight** *lbf*	**Added Mass in Model** *lbf·s²/in*
Skid	3,497	9.06
Draft Sill, Draft Gear, Coupler, Bolster, etc.	7,722	20

D4 – Jacket

The jacket was modeled entirely with deformable shell elements. The diameter of the jacket part was 110.13 inches, representing the mid-plane of the actual jacket. The jacket featured a semicircular cutout at its 12 o'clock position to allow the manway to pass through. The majority of the jacket was meshed with quadrilateral, reduced integration (S4R) elements with a 3.5-inch mesh seed. A small number of triangular, reduced elements (S3R) were used to mesh the head. In the area of the jacket that would be contacted by the impactor, the mesh was made up of quadrilateral, full integration (S4) elements with a 0.04-inch mesh seed. The region of refined mesh was C-shaped in the FE model, as the jacket puncture was assumed to initiate around the perimeter of the impactor. Thus, the fine mesh intended to capture puncture only needed to extend around the region that would contact the perimeter of the impactor. A transition zone between the fine mesh and the coarse mesh also used full integration elements. Because only half the jacket is included in the FE model due to symmetry, the mass of the jacket in the FE model corresponds to half the mass of the physical jacket. Figure D4 shows the geometry and mesh of the jacket, and Figure D5 shows a close-up of the mesh near the impact zone. Table D6 summarizes the properties of the jacket in the FE model.

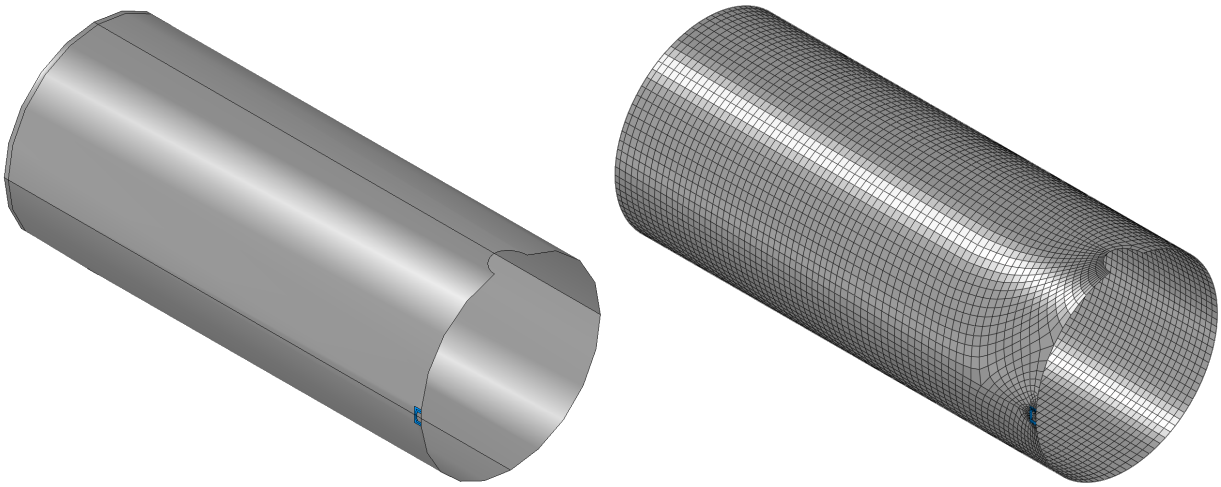

Figure D4. Jacket Geometry (left) and Mesh (right)

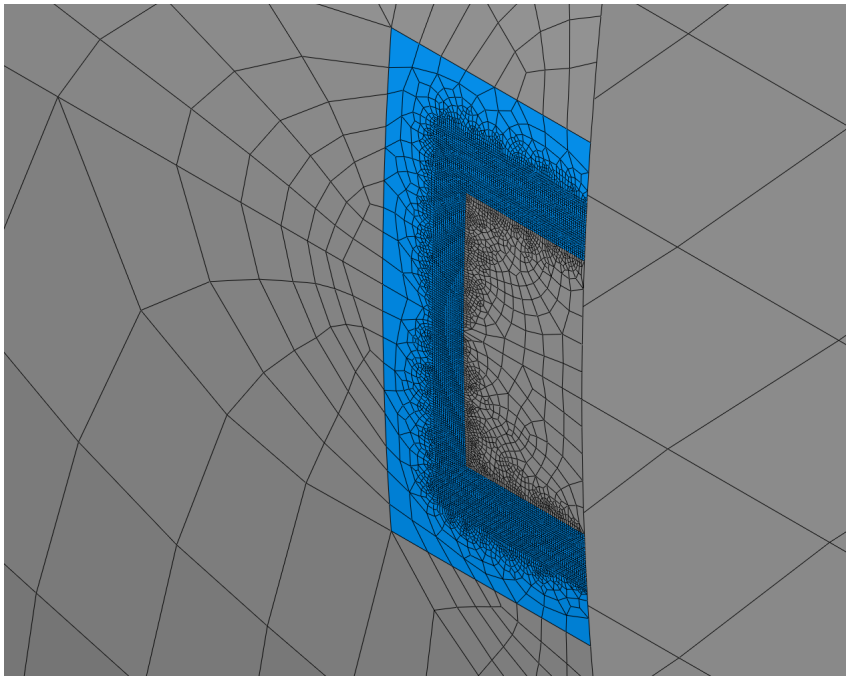

Figure D5. Jacket Mesh in Impact Zone

Table D6. Properties of Jacket in FE Model

	Pre- and Post-test Model
Type of Part	Deformable, Shell
Number of Elements	S4R: 10,021
Number of Elements	S4: 6,402
Number of Elements	S3R: 19
Shell Thickness	0.1196 inch (11 gauge)

	Pre- and Post-test Model
Head Thickness	0.1196 inch (11 gauge)
Material(s)	A1011
Part Weight	3,320 lbf

D5 – Tank (Shell Elements)

The commodity tank was modeled using two different techniques. In the impact zone, the tank was modeled using solid "brick" elements. This part is discussed in Appendix D6. Away from the impact zone, the tank was modeled using shell elements. The shell portion of the tank is described in this section. Because only half the tank is included in the FE model due to symmetry, the mass of the tank in the FE model corresponds to half the mass of the physical tank.

Figure D6 shows the shell portion of the tank. This part was globally meshed using quadrilateral reduced integration (S4R) elements with a 3.5-inch mesh seed. Figure D7 shows the edges of the impact zone. The impact zone mesh was seeded such that each shell element edge (0.17-inch) would span exactly two solid elements on the impacted solid patch. The mesh in the region of attachment to the solid plate was meshed using quadrilateral fully integrated (S4) elements. A technique referred to as shell-to-solid coupling (see Appendix E6) was used to attach the solid patch to the edges of the shell mesh on the tank. The shell part of the tank represents the mid-plane surface of the tank. The shell part has a mid-plane diameter of 101.225 inches in the model. The models include a small number of S3R elements in the head. Figure D6 shows the geometry and mesh of the tank modeled with shell elements.

Table D7 is a summary of the properties of the tank modeled with shell elements.

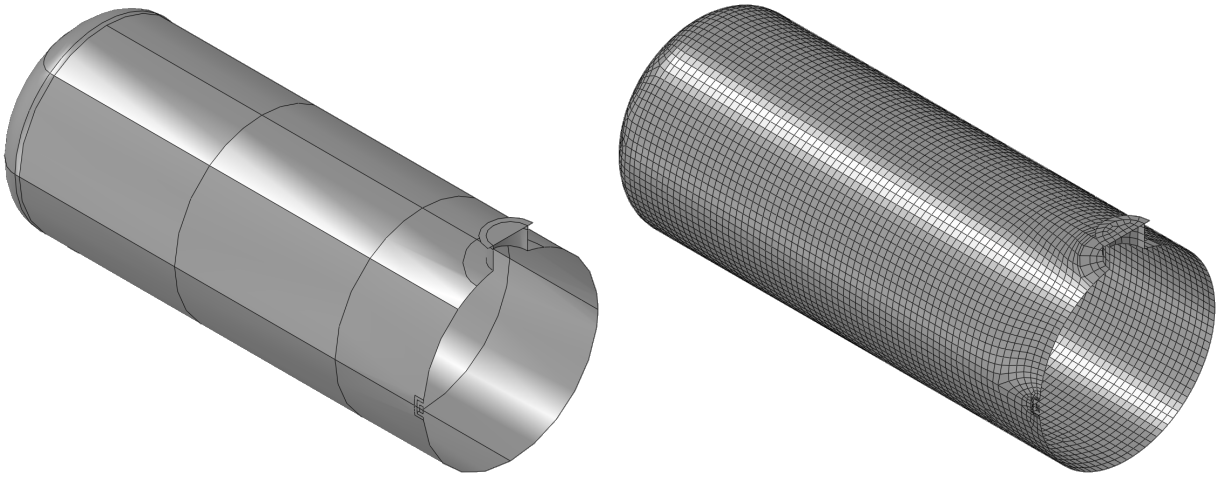

Figure D6. Shell Tank Geometry (left) and Mesh (right)

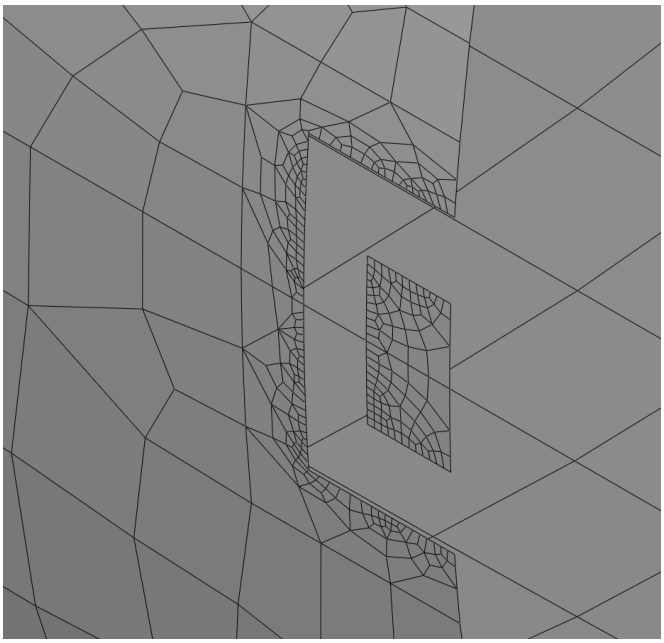

Figure D7. Tank Shell Mesh in Impact Zone

Table D7. Properties of Tank (shell elements)

	Pre-test Model	Post-test Model
Type of Part	Deformable, Shell	Deformable, Shell
Number of Elements	S4R: 7,625	S4R: 7,625
Number of Elements	S4: 319	S4: 319
Number of Elements	S3R: 20	S3R: 20
Shell Thickness	0.775 inch	0.775 inch
Head Thickness	0.8125 inch (13/16”)	0.8125 inch (13/16”)
Material(s)	Test 2 TC128 Test 6 TC128	Test 8 TC128
Part Weight	19,409 lbf	19,409 lbf

D6 – Tank (Solid Elements)

The commodity tank was modeled using two different techniques. Away from the impact zone, the tank was modeled using shell elements. This part is discussed in Appendix D5. In the impact zone, a portion of the tank was modeled using solid brick elements. The solid part of the tank can be described as a solid patch and is detailed in this section. Because only half the tank is included in the FE model due to symmetry, the mass of the solid portion of the tank in the FE model corresponds to half the mass of the corresponding portion of the physical tank.

Figure D8 shows the solid portion of the tank. The outer height of the part measures approximately 7.05 inches high by 3.5 inches wide. The inner cutout measures approximately 3.5 inches high by approximately 2 inches wide. The part was meshed using a 0.085-inch mesh seed,

resulting in 9 elements through the thickness of the tank shell. The solid portion of the tank was meshed using 8-noded hexahedral "brick" (C3D8) elements. The solid tank mesh was attached to the shell tank mesh along the outer and inner edges using shell-to-solid coupling (see Appendix E6). Table D8 is a summary of the properties of the tank modeled with solid elements.

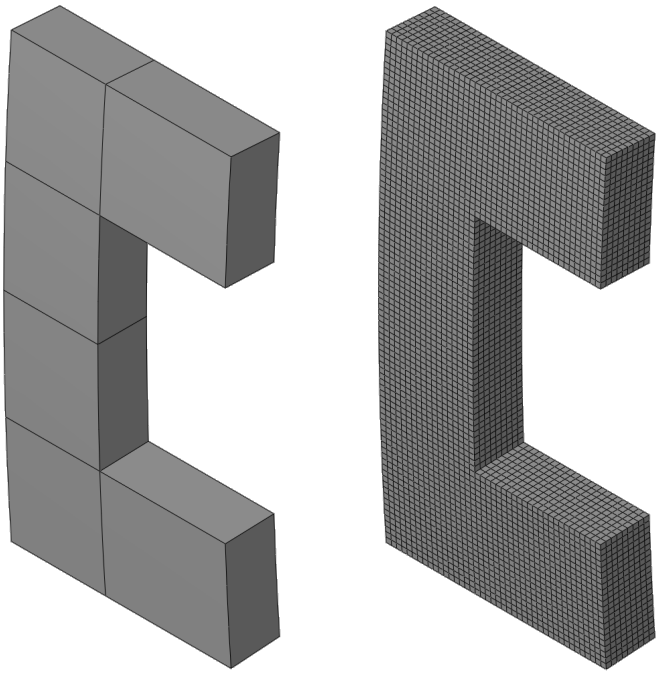

Figure D8. Solid Tank Geometry (left) and Mesh (right)

Table D8. Properties of Tank (solid elements)

	Pre-Test Model	Post-Test Model
Type of Part	Deformable, Solid	Deformable, Solid
Number of Elements	C3D8: 23,760	C3D8: 23,760
Material(s)	Test 2 TC128 Test 6 TC128	Test 8 TC128
Part Weight	3.85 lbf	3.85 lbf

D7 – Membrane

The FE model of the DOT-105 tank car included a deformable membrane part that represented the extents of the lading. The liquid and gas phases of the contents of the tank were modeled within the tank using a hydraulic and a pneumatic cavity, respectively. The material properties used to describe the behavior of the air are described in Section 5.2.1, and the material properties used to describe the water are described in Section 5.2.2. In the FE model, the outage volume was filled with air.

Hydraulic and pneumatic cavity modeling techniques are simplified approaches to capturing the inertial and pressure effects of the liquid lading and the pressure response of the air in the outage. For either cavity, geometry within the model that encloses the limits of the fluid is used to define

the volume of the cavity. For the hydraulic cavity, the water in the tank is bounded by the shell of the tank itself and by its free surface in contact with the outage. For the pneumatic cavity, the outage is bounded by the interior of the tank and the free surface of the water. Thus, the membrane part's geometry represents the interior of the tank, with a horizontal plane to represent the boundary between the air and the water.

For each cavity defined within the membrane, the solver calculates the average pressure and temperature in each time increment during the impact. As the tank deforms from the impact, the hydraulic cavity changes shape. Because the water is highly incompressible, the indentation of the tank reduces the volume of the air in the outage. The pneumatic cavity models the air as an ideal gas with user-defined initial pressure and temperature, and a universal gas constant. Thus, as the volume of the tank is reduced, the volume of the outage decreases and the pressure within the pneumatic cavity increases.

Because the pneumatic and hydraulic cavities only calculate the average pressures and temperatures within the cavity, and not the fluid pressure or temperature at discretized points throughout the volume of the lading, this technique reduces the simulation runtime compared to techniques that represent the fluid explicitly as a mesh or collection of particles. However, the average-behavior simplification may not be well suited to all conditions, such as an impact that features an extremely large tank, or a significant variation in pressure over the volume of either the air or liquid.

Both the hydraulic and pneumatic cavity models require a geometric surface to be defined within the model that defines the boundary of each cavity. Each cavity is also required to have a reference point defined within the volume of the cavity. This reference point is used to define the interior of the cavity and is also the point to which initial temperatures and pressures are defined for each cavity. Because the tank car model is a half-symmetric model, the cavity is not entirely enclosed within the membrane. In the case of a cavity bisected by a symmetry plane, it is necessary to place the cavity's internal reference point on the symmetry plane.

As discussed in Appendix D5, the shell geometry of the tank represents the mid-plane geometry of the tank. If this geometry was used to define the outer surfaces of the pneumatic or hydraulic cavities, the cavity volumes would be too large, since the volume enclosed was based on the mid-plane surface and not the inner surface of the tank. The membrane part was defined to correspond to the inner surface of the tank's geometry. Because the membrane represents geometry that is not physically present within the tank, the membrane was chosen to be as thin and flexible as practical within the model, without causing the model to terminate due to excessively distorted membrane elements. The membrane typically had a thickness of 0.05 inch.

The membrane includes a horizontal plane at the transition between the gas phase of the outage and the liquid phase of the lading. In this way, the horizontal plane is used to define both the surface enclosing the water and the surface enclosing the air. The height of this horizontal plane (i.e., measured from the top of the membrane, as shown in Figure D9) was adjusted to give the desired outage for this tank.

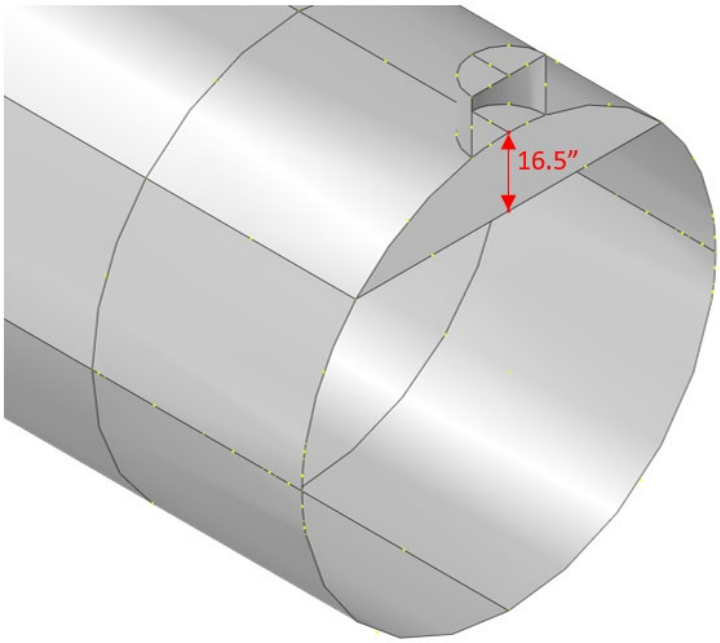

Figure D9. Outage Vertical Height Measurement within Membrane

The relationship between outage height and outage volume for this model is shown in Figure D10. This figure also includes a quadratic regression equation for the volume versus height relationship. For the desired outage of 10.6 percent, the model used an outage height of approximately 16.5 inches below the top of the membrane.

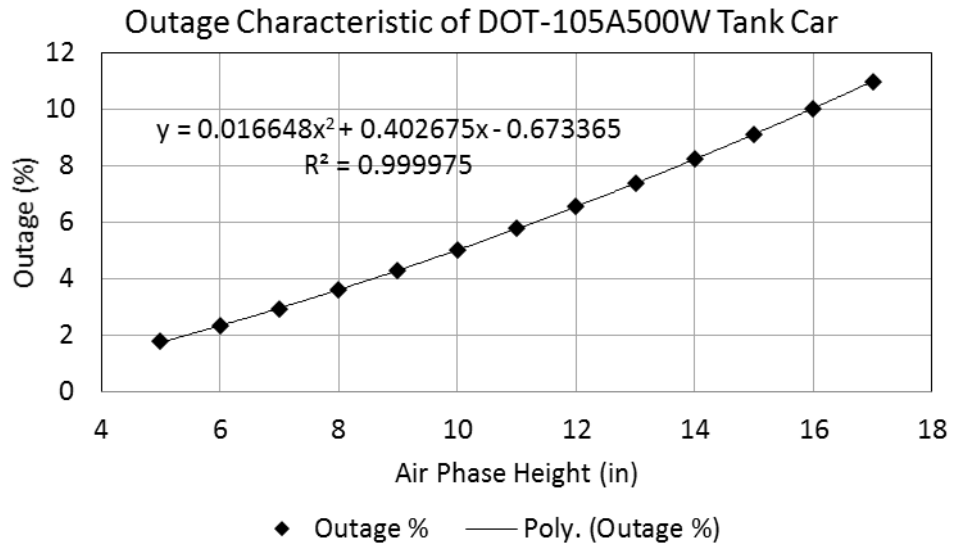

Figure D10. Outage Height versus Outage Volume for DOT-105 Tank Car Model

In addition to representing the surface of the interior of the tank, the membrane was also used to represent the mass of the water lading within the tank. This was done through the use of a “nonstructural mass” feature in Abaqus. The total mass of the water was calculated using the density of water and the volume enclosed by the membrane. This mass was then distributed

through the membrane, including the horizontal portion of the membrane dividing the water and air phases.

The full geometry and mesh of the membrane is shown in Figure D11 and the properties are summarized in Table D9 for the pre-test and post-test models.

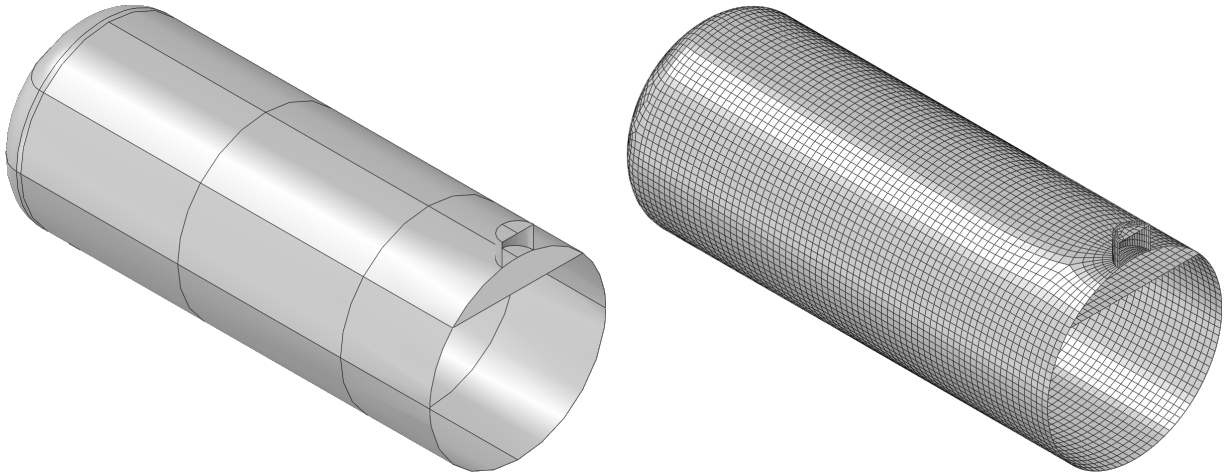

Figure D11. Membrane Geometry (left) and Mesh (right)

Table D9. Properties of Membrane Mesh

	Pre-Test and Post-Test Models
Type of Part	Deformable, Membrane
Number of Elements	M3D4R: 9,540 M3D3: 20
Thickness	0.05 inches
Material(s)	Membrane
Part Weight	Membrane: 1,486.4 lbf Added Weight of Water: 65,162.5 lbf

D8 – Foam Insulation

The FE models of the DOT-105 tank car included a deformable solid part representing the foam insulation between the tank and jacket. Appendix F5 describes the development of the material properties used to define the foam.

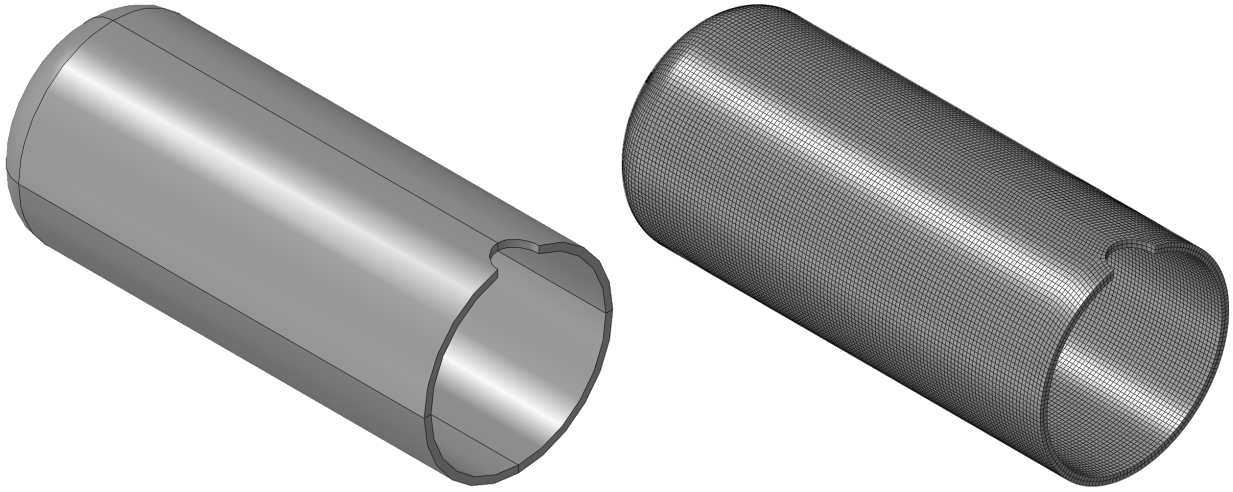

Figure D12. Foam Insulation Geometry (left) and Mesh (right)

Table D10 summarizes the properties of the foam insulation part.

Table D1. Properties of Foam Insulation Mesh

	Pre- and Post-test Model
Type of Part	Deformable, Solid
Number of Elements	C3D8R: 44,498
Material(s)	Insulation
Part Weight	420.8 lbf

Appendix E.
Finite Element Modeling Techniques

This document describes the boundary conditions, initial conditions, constraints, and contact definitions within the FE model.

E1 – Symmetry Conditions

During the impact test, the test plan called for the impactor to strike the DOT-105 tank car at its longitudinal center. To facilitate computational efficiency, a half-symmetric model was used to simulate the test. A symmetry boundary condition was applied to the tank (solid and shell element portions), the jacket, and the membrane defining the outer limits of the water and air within the tank.

E2 – Rigid Impactor Boundary Conditions

The rigid impactor was constrained against all motion except for longitudinal displacement. The impactor was given an initial velocity corresponding to the simulated impact speed. The pre-test models were run at various speeds to determine an estimated range for puncture. After the test, the pre-test models were run at the measured test speed of 9.7 mph. The post-test model which incorporated a calibrated material based on tensile coupon testing was run at the test speed of 9.7 mph.

E3 – Rigid Wall Boundary Conditions

The rigid wall was constrained against motion in all degrees-of-freedom (DOF).

E4 – Jacket-to-Tank Tie

The jacket and tank were attached to one another using a “tied constraint” acting over the region of the bolster in the physical tank car. Standoffs between the tank and jacket were not included in this model, so this tied constraint represented the only direct connection between the tank and jacket. A tied constraint was defined between the arc representing the bolster on both the tank and the jacket parts. Figure E1 shows the tied constraint between the jacket and tank with a 4.5-inch gap where the insulation exists.

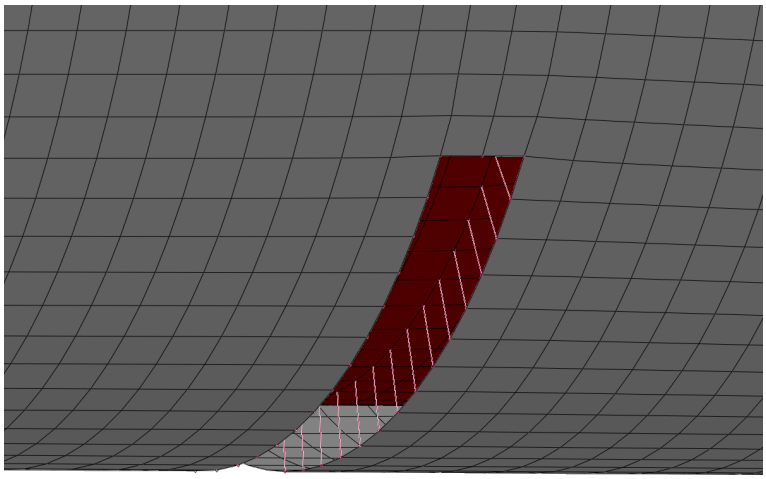

Figure E1. Jacket-to-Tank Tie Constraint with 4.5-inch Offset (insulation not shown)

E5 – Tank-to-Skid Coupling

The tank was connected to the rigid skid through a kinematic coupling. This coupling applied to all six DOF. The coupling was defined between the arc of nodes on the tank representing the bolster and the rigid body reference point of the skid, as shown in Figure E2.

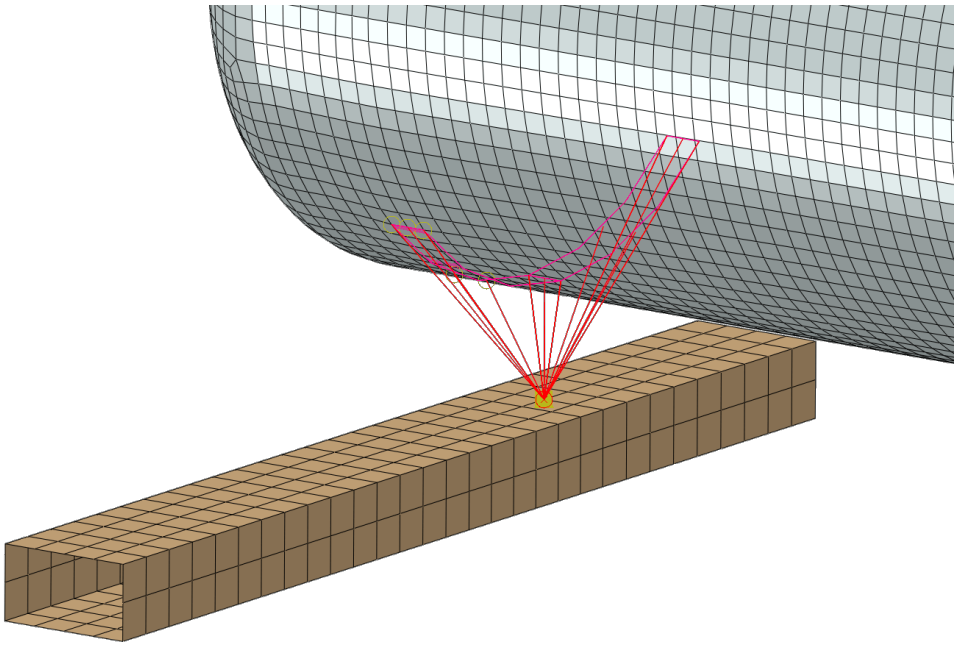

Figure E2. Tank-to-Skid Coupling (jacket and insulation not shown)

Additionally, a "Cartesian" type of connector was used to constrain the motion of the skid in both the vertical and the longitudinal (in the direction of impactor travel) directions. A nonlinear damper was defined between the skid and ground to constrain longitudinal motion. This damper defined the longitudinal resistance force as a function of skid speed, such that the skid had to overcome an initially high force when it was moving slowly. Once this initial peak was overcome, the resistance offered to skid motion diminished as the skid moved more quickly. This

simplified model was intended to approximate the effect of static friction being overcome as the skid initially begins its motion, followed by a reduced resistance from kinetic friction. The longitudinal relationship used in the Cartesian connector is shown in Table E1. Due to an input error, the longitudinal skid behavior was inadvertently applied in the vertical direction in the pre-test models; however, the longitudinal motion of the skids was still in good agreement with the test results for the pre-test (see Figure C13) and post-test (see Figure C27) simulations.

Table E1. Longitudinal Skid Behavior

Skid Velocity *in/s*	**Reaction Force** *lbf*
-10	-100
-1	-38,000
0	0
1	38,000
10	100

In the vertical direction, the skid used a "Stop" behavior assigned to a connector between skid and ground to limit its range of motion. In the vertical downward direction, the reference point of the skid was prevented from having any displacement. In the upward direction, a limit of 100 inches was used. This number is arbitrary but was chosen to be larger than any anticipated vertical motion of the skid. These two vertical stops approximated the behavior of the skid on the ground during the physical test, where the skid was prevented from moving downward through contact with the ground but free to lift upward if sufficient lifting forces overcame the weight resting on it.

E6 – Shell-to-Solid Coupling

A shell-to-solid coupling was used to attach the patch of solid elements in the vicinity of the impact zone to the rest of the shell-meshed tank. This type of constraint is necessary to ensure a smooth transition from solid elements, which possess only translational displacement DOF, and shell elements, which possess translational and rotational DOF. As previously described in Appendix D6, the meshes on the solid part and the shell part were defined so that every shell element (0.17-inch edge length) adjacent to the solid patch spanned two solid elements (0.085-inch edge length). Since the shell part corresponded to the mid-plane thickness of the tank, the shell part was aligned with the mid-plane of the solid patch. Figure E3 shows the interface between the nodes on the solid patch elements and the tank shell elements.

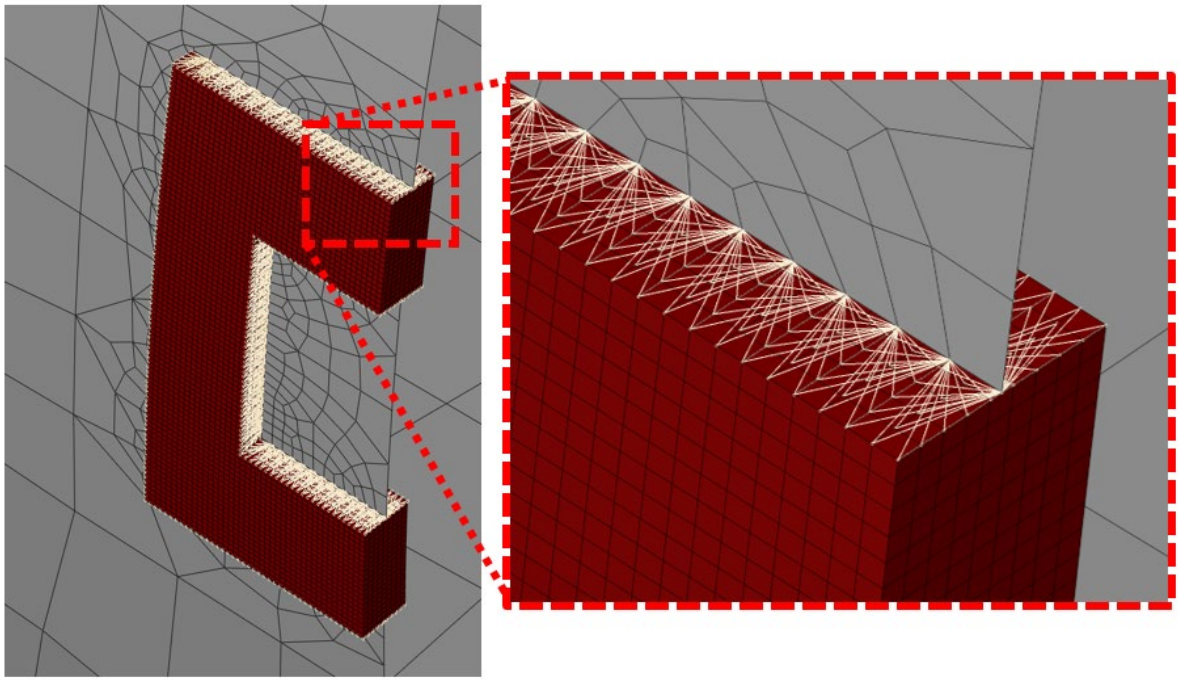

Figure E1. Shell-to-solid Coupling Region between Solid Patch Elements (red) and Shell Elements (grey) in Tank Model

The shell-to-solid coupling behavior was not adjusted between the pre- and post-test models.

E7 – Internal Pressures and Temperatures

The lading within the tank was given an initial pressure of 100 psi. As the surfaces describing the boundaries of the water and gas phases deformed, the pressure was free to change in response. The hydraulic cavity and pneumatic cavity definitions also require the definition of the ambient pressure outside of the cavity. A value of 12.3 psi (Engineering ToolBox, 2003), corresponding to atmospheric pressure in Pueblo, CO, altitude of approximately 4,700 feet (U.S. Geologic Survey, 2019), was used for ambient pressure. Thus, the air within the tank was initially modeled at an absolute pressure of 112.3 psi.

The fluid cavity approach of modeling liquids and gases required an initial temperature to be defined for the ladings. Based on average historical climate data around the planned date of the DOT-105 tank car test, an initial temperature of 70 °F was chosen for the models (U.S. Climate Data version 3.0, 2019). This value was not changed in post-test modeling, as the measured temperature of the lading at the time of the test was measured as approximately 75 °F.

E8 – Springs

Spring elements were placed within the model at locations corresponding to the string potentiometers installed within the tested tank (see Section 3.3). The use of springs allowed a direct comparison between the change-in-length of a string potentiometer during the test and the change-in-length of the corresponding spring in the FE model. The stiffness of the spring elements was set at a low value (1×10^{-6} lbf/in) to avoid force concentrations in the tank shell.

E9 – Mass Scaling

Variable mass scaling was used in the puncture-capable models. Because of the need for a refined mesh of solid elements in the impact zone, the puncture-capable models feature many very small elements. These two factors combine to create models with significant runtimes, even when executed on multiple CPU workstations. Variable mass scaling was employed in the FE models to decrease the runtime without decreasing either the span or the resolution of the refined meshes. Variable mass scaling is a technique in which the user sets a target time increment for a set of elements within the model (i.e., up to and including all elements within the model) and the Abaqus solver increases the mass of each element to attempt to bring the minimum time step up to the user-defined minimum. "Variable" refers to the software's ability to increase the mass of each element by a different amount, based on the material and geometry of each element. While mass scaling is an efficient way of reducing runtime without re-meshing a model, care must be exercised when using this technique with highly dynamic simulations. If an overly aggressive mass scaling is applied, the amount of artificial mass added to the model in the refined mesh area can significantly affect both the overall dynamic response as well as the puncture behavior of the model.

The material coupon models used variable mass scaling to achieve a target time of 1×10^{-6} seconds over the entire model. The pre-test and post-test puncture-capable FE models used a variable mass scaling to achieve a target time increment of 3×10^{-7} seconds over the entire model. The mass scaling factors were recalculated for the full-scale puncture models at 20 intervals during the simulation.

E10 – Contact

A general contact definition was used in this model. The global contact used frictionless contact, except for metal-on-metal contact. A coefficient of friction of 0.3 was defined for regions of metal on metal contact. Contact exclusions were defined between the jacket and itself, and between the shell tank and the solid tank patch.

Appendix F.
Material Behaviors in Finite Element Models

F1 – Introduction

Pre-test finite element (FE) models used TC128 (tank) and A1011 (jacket) material responses that were based on models developed during previous testing efforts. A full description of the processes used to develop these material models can be found in the Test 2 and Test 6 reports (Kirkpatrick, S. W, 2010) (Carolan, M., & Rakoczy, P., 2019).

Following the side impact test, material coupons were cut from the tested DOT-105 tank car and subjected to tensile coupon testing. The results of these material coupon tests were used to create a new TC128 material for post-test modeling. This appendix describes the processes used to create the pre-test and post-test material models.

F2 – Simulation of Coupon Tests

For both the A1011 jacket material and the TC128 tank material, FE simulations of tensile coupon tests were used to calibrate the material definitions in Abaqus. First, the plastic true stress-plastic equivalent strain (PEEQ) characteristic was specified. Then, the damage initiation envelope was calculated. Finally, a reasonable damage progression was empirically determined.

As the material responses developed using a coupon model were planned for implementation in the full-scale DOT-105 tank car model, modeling techniques for performing the coupon simulations were chosen deliberately to be similar to the modeling techniques planned for side impact analysis of the DOT-105 tank car. The same solver (Abaqus/Explicit), element types, and mesh sizes were chosen for each coupon model and the corresponding material in the DOT-105 tank car model. This was done to attempt to minimize the uncertainty associated with calibrating a material response using one set of techniques but using a different set of techniques to model puncture in the tank car impact simulation. If the tank car model was run using a different solver or different mesh size, it is expected that the material behaviors would need to be recalibrated using coupon simulations that used similar solvers and mesh density.

For all tensile coupons, a 2-inch gage length was used, as all the tensile coupon tests used that gage length. Within the tensile coupon FE models, a soft (1×10^{-6} lbf/in) spring was included in the model to represent an extensometer attached to the ends of the 2-inch gage. This spring was surrogate for an extensometer in the model and simplified the process of requesting the change-in-length of the gage section from the model.

The ASTM A1011 flat dog-bone tensile coupon model was meshed using 0.04-inch fully integrated quadrilateral shell elements (S4) in the gage section and reduced integration elements (S4R) outside of the gage region. The thickness of the shell elements was set to the nominal thickness of the DOT-105 jacket (11 gauge or 0.1196-inch). A symmetry plane was applied on the vertical-lateral plane to reduce the number of elements and simulation runtime. The geometry and mesh of the ASTM A1011 tensile coupon FE model are shown in Figure F1.

Figure F1. FE Model of ASTM A1011 Tensile Coupon

Because the tank shells of DOT-105 tank cars are constructed from thick TC128 steel plates (0.775 inch), cylindrical specimens having a 0.5-inch diameter were used in tensile tests. The FE models of the tensile coupons were meshed using hexahedral (brick) elements, with three to four elements across the radius of the coupon. The 2-inch gage region was meshed using fully integrated 8-node linear brick (C3D8) elements, while the regions outside of the gage were meshed using reduced integration brick (C3D8R) elements. Three symmetry planes were applied to the smooth round bar tensile coupon model to facilitate computational efficiency.

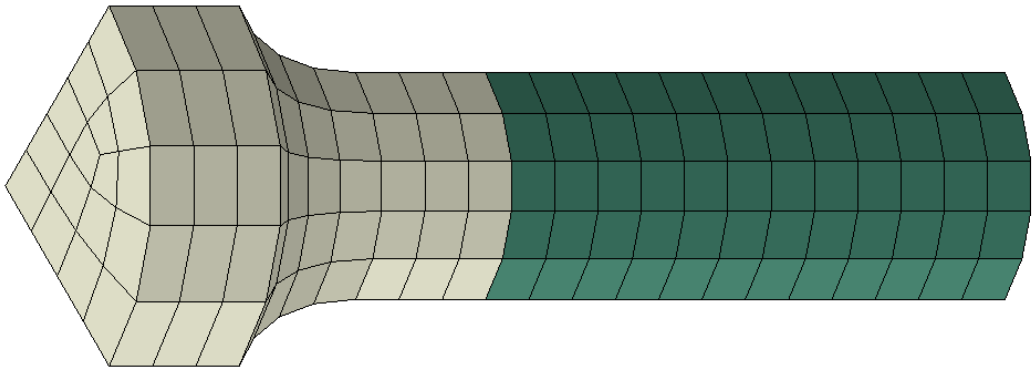

Figure F2. FE Model of TC128 Tensile Coupon

Abaqus/Explicit requires metal plasticity to be defined in terms of true stress and PEEQ. The plastic behavior of each steel was input to the Abaqus model as isotropic hardening using a discrete number of data points calculated from the nominal stress-strain tensile coupon data according to Equation F1.

Equation F1. True Stress-strain Transformation

$$\sigma_{true} = \sigma_{nom} \cdot (1 + \varepsilon_{nom})$$

$$\bar{\varepsilon}^{pl} = \ln(1 + \varepsilon_{nom}) - \frac{\sigma_{true}}{E}$$

σ_{nom} nominal (engineering) stress
ε_{nom} nominal (engineering) strain
σ_{true} true stress
$\bar{\varepsilon}^{pl}$ plastic equivalent strain (PEEQ)

Because necking dominates the nominal stress-strain response of the tensile coupon characteristic after the max force is achieved, the true stress-PEEQ relationship was extrapolated for strains beyond the strain at maximum force.

Figure F3 shows a schematic of the Bao-Wierzbicki (B-W) triaxiality (η) based damage initiation envelope (Bao, Y., & Wierzbicki, T., 2004) which was used in the A1011 and TC128 material failure models. Triaxiality is defined as the ratio of the hydrostatic stress (mean stress) divided

by the von Mises stress (equivalent stress) and describes the general stress state of an element. The B-W envelope consists of three regions: I – Ductile Fracture, II – Mixed Fracture, and III – Shear Fracture.

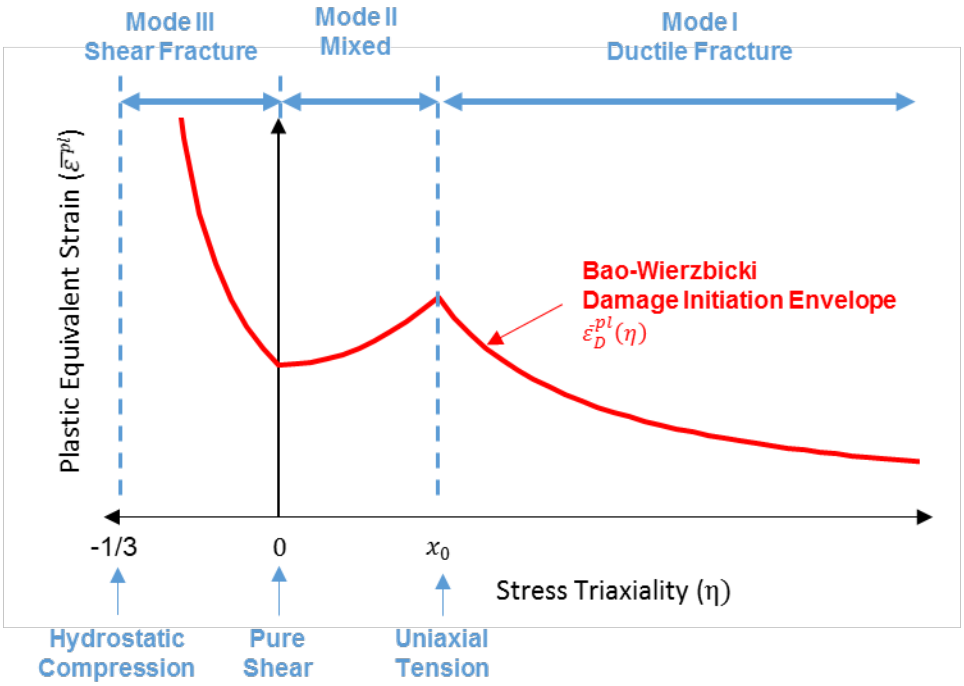

Figure F3. Schematic of Bao-Wierzbicki Damage Initiation Envelope

When $\eta < 0$ the element is in a state of compression, and when $\eta > 0$ the element is in a state of tension. A triaxiality of $\eta = -1/3$ corresponds to a stress state of hydrostatic compression and $\eta = 0$ corresponds to pure shear. The cusp of the B-W envelope is located at the average triaxiality on the fracture surface of a smooth round bar specimen under uniaxial tension at $\eta = x_0$ and is typically close to a value of 0.4.

The complete damage initiation envelope can be developed through a series of mechanical tests on 11 unique specimen geometries intended to cover a wide range of stress triaxialities; however, a simplified "quick calibration" approach was developed for industrial use by Lee and Wierzbicki (Lee, Y.-W, 2005) (Lee, Y.-W., & Wierzbicki, T, 2004) which requires only one uniaxial tensile geometry to estimate the entire failure envelope. The quick calibration approach is intended to be within 10 percent agreement with a failure envelope that was developed using the complete set of 11 specimens.

Two constants (a and b) govern the shape of the B-W damage initiation envelope (see Equation F2) and are calibrated based on coupon test results. The variable a corresponds to the PEEQ on the B-W envelope $(\bar{\varepsilon}_D^{pl})$ when $\eta=0$ (pure shear). The variable b corresponds to $(\bar{\varepsilon}_D^{pl})$ at the cusp of the B-W envelope when $\eta=x_0$.

Equation F2. B-W Damage Initiation Envelope

$$\bar{\varepsilon}_D^{pl}(\eta) = \begin{cases} \dfrac{a}{1+3\cdot\eta} & -\dfrac{1}{3} \le \eta \le 0 \\ (b-a)\cdot\left(\dfrac{\eta}{x_0}\right)^2 + a & 0 \le \eta \le x_0 \\ \dfrac{b\cdot x_0}{\eta} & x_0 \le \eta \end{cases}$$

For ductile metals in Abaqus, the damage threshold of an integration point is reached when the ductile criterion (DUCTCRT) reaches a value of 1. The DUCTCRT is calculated according to Equation F3.

Equation F3. Calculation of DUCTCRT in Abaqus

$$DUCTCRT = \int \frac{d\bar{\varepsilon}^{pl}}{\bar{\varepsilon}_D^{pl}(\eta)}$$

After DUCTCRT reaches a value of 1 the stiffness of the element is degraded according to the damage progression in the material definition. In this report, energy-based damage progression values are calibrated for each material; however, the damage progression could also be specified based on displacement.

F3 – ASTM A1011 Steel

The ASTM A1011 steel material model used in the jacket is based on the A1011 material response developed during a previous testing program (Test 6) (Carolan, M., & Rakoczy, P., 2019). Appendix F of the Test 6 report contains a full description of the process used to develop the A1011 material. As the material behaviors for A1011 were previously developed for implementation in a 0.04-inch fully integrated shell element (S4) mesh, this same mesh formulation and element size were used in the DOT-105 model. The plastic stress-strain behavior used in the DOT-105 model for the A1011 jacket is given in Table F1.

Table F1. ASTM A1011 Steel True Stress and Plastic Equivalent Strain Behavior

True Stress *psi*	PEEQ *in/in*
4.70E+04	0.00E+00
4.60E+04	8.22E-04
4.62E+04	1.20E-02
5.30E+04	3.00E-02
5.80E+04	6.00E-02
6.20E+04	1.10E-01
6.80E+04	1.95E-01
1.25E+05	1.15E+00

Figure F4 shows the stress-strain characteristic from a FEA of a 2-inch gauge tensile coupon using the same elements and mesh density as the full-scale model. The damage initiation

envelope used in the DOT-105 models is shown in Figure F5. A summary of the material properties is presented in Section 5.2.5.

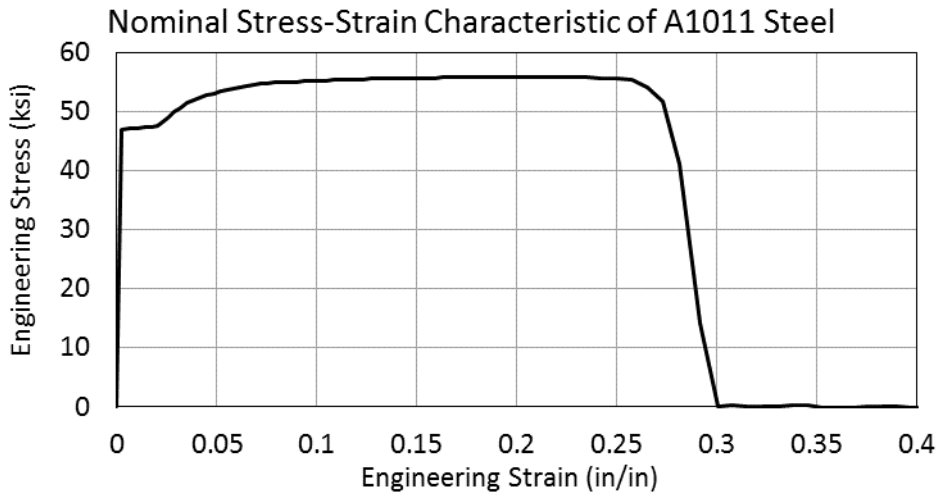

Figure F4. ASTM A1011 Steel Nominal Stress-Strain FE Results

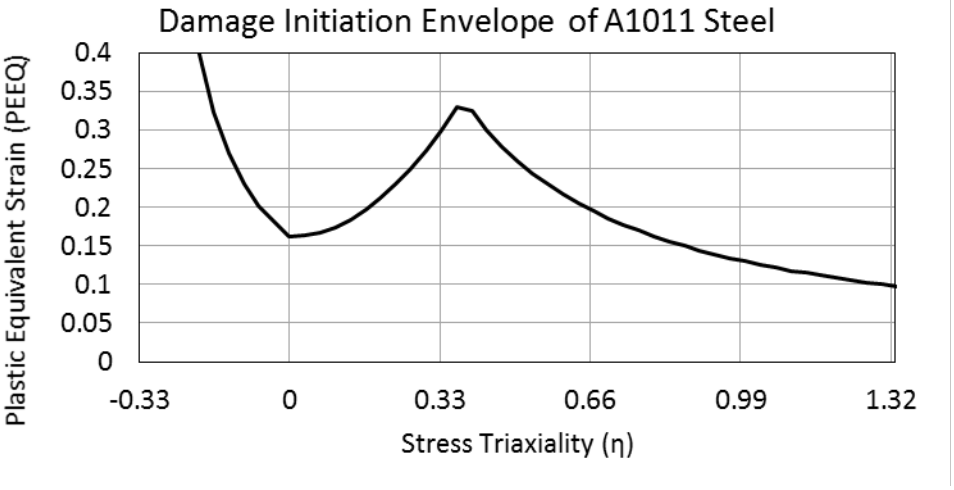

Figure F5. ASTM A1011 Steel B-W Damage Initiation Envelope

F4 – AAR TC128 Grade B Steel

Three characterizations of TC128 were used in modeling puncture of the DOT-105 tank car because the actual properties of the TC128 making up this DOT-105 tank car would not be known until coupons were cut from the tank car shell. Prior to the test, two models were developed with different TC128 steels from DOT-105 tank cars, corresponding to Test 2 (Kirkpatrick, S. W, 2010) and Test 6 (Carolan, M., & Rakoczy, P., 2019). After the test, a third characterization was developed based on the measured properties from tensile coupons cut from the tested (Test 8) DOT-105 tank car.

The average yield strength (YS), ultimate tensile strength (UTS), elongation, and reduction in area (RA) were averaged from TC128 tensile test results for each of these three tank cars. The average mechanical properties of the materials are summarized in Table F2.

Table F2. Summary of Mechanical Properties of TC128 in Pre- and Post-Test Models

FE Model	Source	YS *ksi*	UTS *ksi*	Elongation *Percent*	RA *Percent*
Pre-Test	Test 2	58	80	32	-
Pre-Test	Test 6	70	94	22	48
Post-Test	Test 8	70	94	25	49

From these data, it is apparent that there is considerable variation in the mechanical properties of TC128 that can be encountered, even from cars constructed in the same period of time to the same specification. More information on the range of mechanical properties of TC128 samples from retired tank cars can be found in Southwest Research Institute's report from McKeighan et al. (2008).

Two TC128 sources in Table F2 exhibited similarities. TC128 tensile coupons taken from the DOT-105 tank cars used in Test 6 and the current test (Test 8) exhibit nearly identical 0.2 percent offset YS, UTS, and RA. Test 8's tensile coupons had a slightly higher elongation at break than Test 6.

The TC128 coupons from Test 2 tended to have a lower YS and UTS but much higher elongation and therefore a higher overall toughness. This resulted in the pre-test puncture models that used a TC128 material definition calibrated from Test 2's tensile coupons having a higher puncture resistance (11 mph puncture speed) when compared with material characterized following Test 6 (9 mph puncture speed).

It was expected that the TC128 in the Test 8 DOT-105 tank car would likely have mechanical properties similar to the tank car from Test 6 because these cars were made in the same production run by the same manufacturer; however, there was still a possibility that the tank car from this test would have TC128 with a higher ductility so the TC128 from the Test 2 tank car was used as an upper bound. Because the specification for TC128 does not place an upper limit on elongation, the Test 2 TC128 must be understood as being the upper limit of ductility *for which data are currently available*. It is possible for other samples of TC128 to meet the strength requirements of the specification while exceeding the minimum ductility by an even greater amount; however, no such samples were identified in publicly available sources prior to the test.

F4.1 – Pre-Test TC128 Material Characteristics

Tabular true stress and PEEQ for the TC128 pre-test material models are given in Table F3 for Test 2 and Table F4 for Test 6.

Table F3. True Stress and Plastic Equivalent Strain Inputs for Test 2 TC128 (Kirkpatrick, S. W, 2010)

True Stress psi	PEEQ in/in
5.45E+04	0.00E+00
5.46E+04	8.22E-04
5.48E+04	1.30E-02
6.65E+04	2.76E-02
7.95E+04	5.41E-02
9.02E+04	9.87E-02
9.60E+04	1.49E-01
1.65E+05	1.15E+00

Table F4. True Stress and Plastic Equivalent Strain Inputs for Test 6 TC128 (Carolan, M., & Rakoczy, P., 2019)

True Stress psi	PEEQ in/in
7.150E+04	0.000E+00
7.175E+04	4.356E-03
7.200E+04	7.867E-03
7.520E+04	1.186E-02
8.207E+04	1.950E-02
8.814E+04	2.950E-02
9.302E+04	3.950E-02
9.690E+04	4.950E-02
9.994E+04	5.950E-02
1.023E+05	6.950E-02
1.042E+05	7.950E-02
1.058E+05	8.950E-02
1.072E+05	9.950E-02
1.091E+05	1.124E-01
1.620E+05	1.000E+00

Further details on the development of the Test 2 and Test 6 pre-test material models can be found in Appendix F4 of the Test 6 report from Carolan & Rakoczy (2019).

The B-W damage initiation envelopes for the TC128 materials definitions used in the pre-test puncture models are shown in Figure F6. The damage initiation envelope from Test 2 was calibrated from a series of tests on 5 specimen geometries and with average stress triaxialities in the region of failure ranging from 0 to 1.5 (see Figure 65 in the Test 2 report from Kirkpatrick [2010]). The damage initiation envelope from Test 6 was created using the quick calibration procedure on a standard uniaxial tensile geometry (see Table F8 of the Test 6 report from Carolan & Rakoczy [2019]).

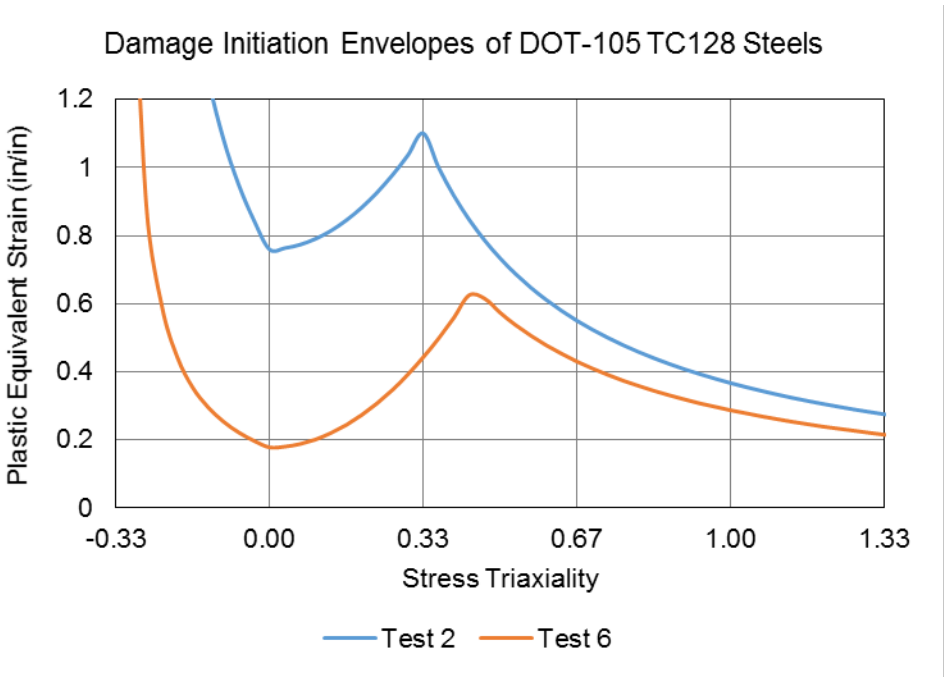

Figure F6. Damage Initiation Envelopes for TC128 from Pre-Test Models

The Test 2 material definition used an energy-based exponential damage progression value of 700 in-lbf/in^2. For the Test 6 material definition, an energy-based linear damage progression value of 1,400 in-lbf/in^2 was specified for the 0.085-inch mesh size. The results of FEA of the 2-inch gage, 0.5-inch diameter round bar tensile model (specified in Appendix F2) are shown in Figure F7. A vertical line is drawn on the plot to represent the nominal strain where damage initiates.

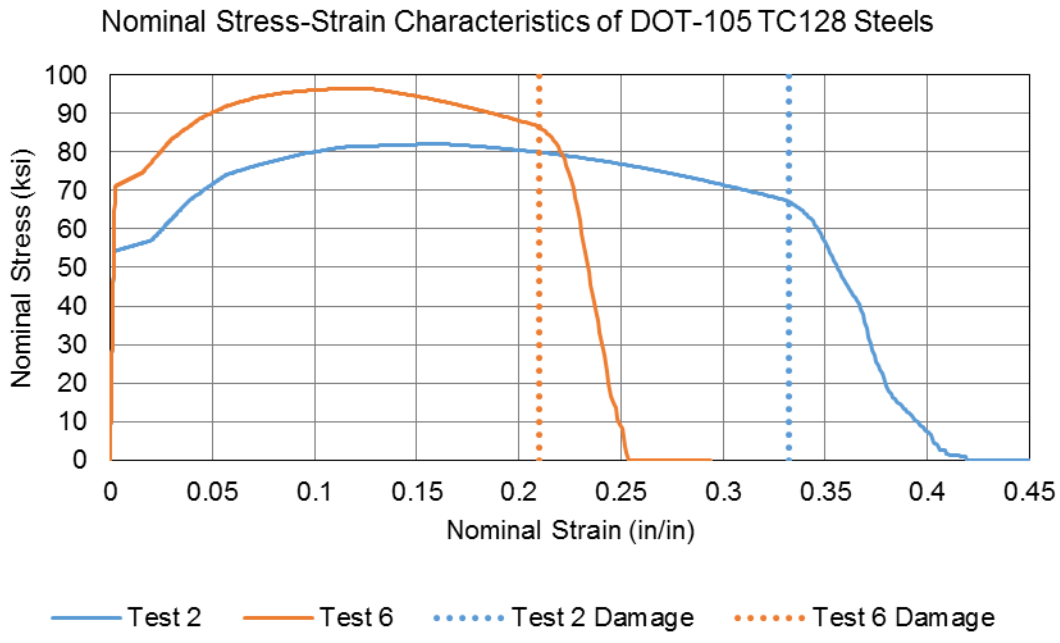

Figure F7. Pre-Test Nominal Stress-Strain Tensile Coupon FE Results

The Test 2 material has a relatively soft slope after damage initiates when compared with the Test 6 material. Also, the Test 2 material has an abrupt change in slope during the process of element deletion at an approximate nominal strain of 0.38 in/in when the center elements have been fully deleted but the edge elements have not yet had their stiffness fully degraded. This is due to a high damage initiation threshold at the Test 2 envelope's cusp ($\eta = 1/3$), which corresponds to the triaxiality in the edge elements, and a sharp decline at higher triaxiality corresponding to the triaxiality in the center elements. In the Test 6 case, the edge elements degrade first but the center elements also degrade and delete shortly afterwards so a secondary slope is not observed in the nominal stress-strain response from the model.

Figure F8 shows the deformed shape of the tensile coupon FE models with the Test 2 (left) and Test 6 (right) material definitions. Overlay contour plots of the DUCTCRT and PEEQ outputs are shown to compare how close the fracture surface elements are to the damage initiation envelope at the point where at least one element has crossed the damage threshold. For reference, a DUCTCRT value of 1 indicates that the element has started to damage and that the stiffness is being degraded.

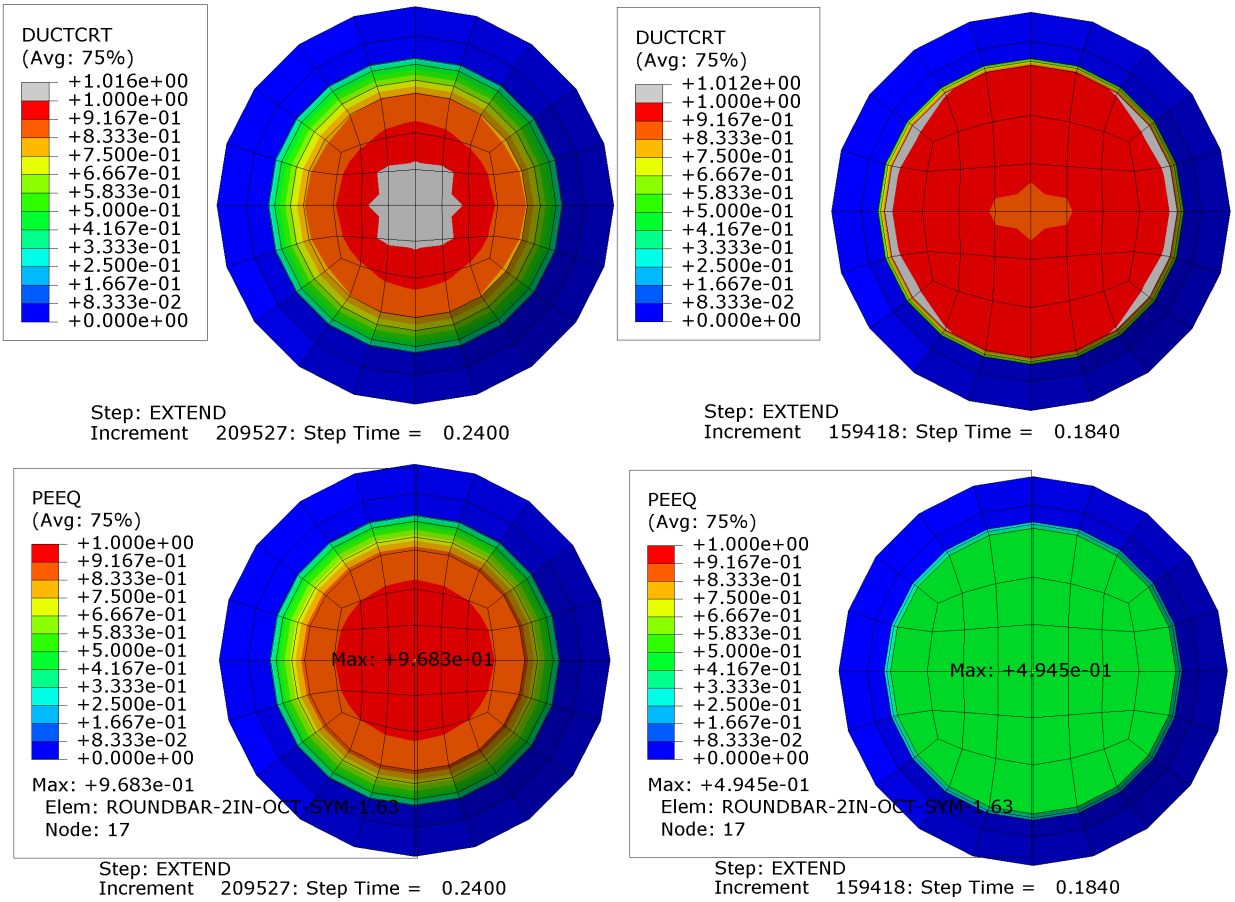

Figure F8. Tensile Coupon FE Model with Test 2 TC128 (left) and Test 6 TC128 (right) Showing Contour Plot of DUCTCRT (top) and PEEQ (bottom) Immediately After Damage Initiation

Comparing these images shows the fracture surface of the tensile coupon model with the Test 6 material definition has a more uniform DUCTCRT, which resulted in faster element degradation

and deletion. The tensile coupon model with the Test 2 material definition had elements deleting at the center of the fracture surface while the elements on the edge of the specimen had not yet had their stiffness degraded, which resulted in the soft failure characteristic visible in Figure F7.

Figure F8 also shows that the Test 6 coupon initiates damage at the edge first but the maximum PEEQ is located at the center of the coupon. This is a result of the damage initiation envelope being comparatively low for Mode II–Mixed Fracture and high for Mode I-Ductile Fracture (see Figure F3). The Test 2 damage initiation envelope is comparatively much higher in Mode II-Mixed Fracture.

Note that the nominal stress-strain characteristics from the tensile coupon FE models (Test 2 and Test 6) in the Test 6 report had lower elongations at break than the characteristics in this report (see Figure F7) even when using the exact same material definition in Abaqus. The coupon models used C3D8I (incompatible mode) elements in the Test 6 report, while C3D8 elements were used in this study. The C3D8I elements were observed to fail earlier than the C3D8 elements due to integration points near the edge of the coupon model reaching an unusually high stress triaxiality after necking. The observed stress triaxiality (~2) was outside the typical range $(1/3 \leq \eta \leq 1/2)$ for a smooth round bar uniaxial tension coupon.

The Test 6 failure model has a fracture energy of 1,400 in-lbf/in^2 whereas the post-test (Test 8) failure model has a fracture energy of 850 in-lbf/in^2. Recall that fracture energy is not a measured quantity, but it is calibrated by comparing the overall agreement of tensile simulation results with tensile test measurements. It is expected that the Test 6 failure model would have had a lower fracture energy specified if it had been calibrated using a tensile coupon FE model with C3D8 elements. This would result in the FE model elongation at break (25 percent) being closer to what was measured in testing (22 percent) and result in a lower toughness.

Even though the pre-test (Test 2 and Test 6) FE coupon nominal stress-strain characteristics tended to overestimate the elongation at break measured in testing (Table F2), the pre-test models were still accurate in predicting the speed range that puncture would occur for the current test. The residual puncture speed (approximately 0.5 mph) from the current test was only slightly lower than expected due to the pre-test puncture models being slightly less conservative than anticipated due to the change in solid element type.

F4.2 – Post-Test TC128 Material Characteristics

Following the test, three smooth round bar tensile coupons with a 0.5-inch diameter and 2-inch gage length were cut from the tested DOT-105 tank car and sent to a test lab for tensile testing. The results of the tensile tests are included in Appendix B. Additionally, the raw stress-strain test data was provided to Volpe for the purpose of calibrating a material definition in Abaqus for the actual TC128 in the tested tank car. Figure F9 contains a plot of the three-nominal stress-strain characteristics from the tested tensile coupons and the response from the FE model of the tensile coupon after calibrating the plasticity and material failure definitions.

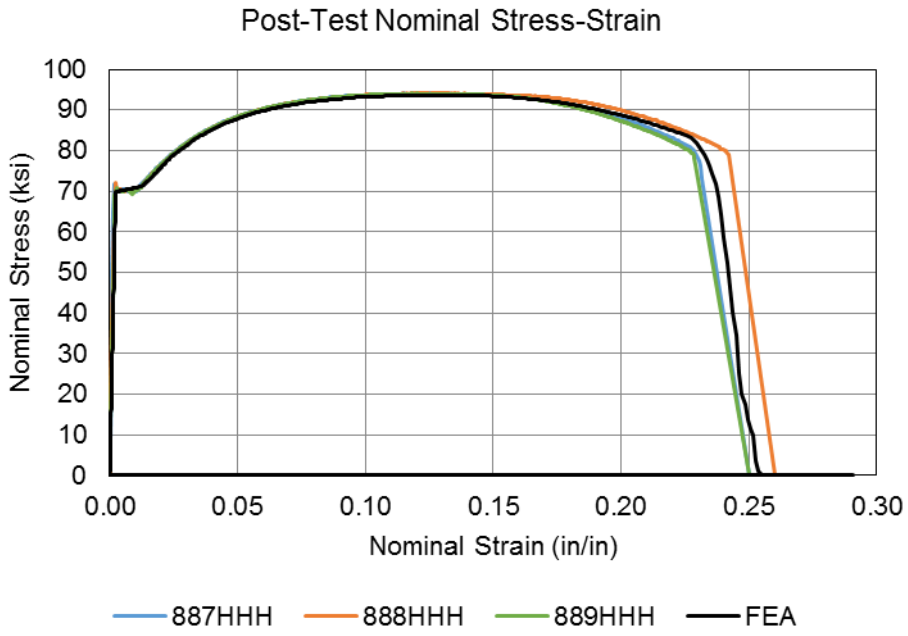

Figure F9. Nominal Stress-Strain Characteristics of Post-Test (Test 8) Tensile Coupons and FE Results

The nominal stress-strain characteristic of the most representative tensile coupon (887HHH in Figure F9) was used to calculate (see Equation F1) a true stress-PEEQ input for the FE model. A discrete number of points were manually fit onto the true stress-PEEQ curve up to the UTS of the specimen. In the region after UTS, where necking dominates the response, the isotropic hardening of the material was estimated using a power law fit up to a large (1 in/in) strain. The power law equation is given in Equation F4, and the constants (A = 138.38 *ksi*, $n = 0.1248$) were determined by a least-squares regression on the true stress and PEEQ characteristic of the representative tensile coupon sample using a window of the test data prior to the UTS.

Equation F4. Power Law Equation Used to Extrapolate True Stress at Large Strain

$$\sigma_{true}\left(\bar{\varepsilon}^{pl}\right) = A \cdot \left(\bar{\varepsilon}^{pl}\right)^{n}$$

The start of the window was adjusted manually until the extrapolated plasticity input curve resulted in an output from the tensile coupon FE model that accurately represented the necking behavior observed in the test data. Figure F10 shows: (1) the calculated true stress-strain curve from tensile coupon #887HHH, (2) the windowed test data where regression was applied, (3) the extrapolated plasticity using the power fit equation, and (4) the calculated true-stress strain response from the tensile coupon FE model, which can be compared with the test data.

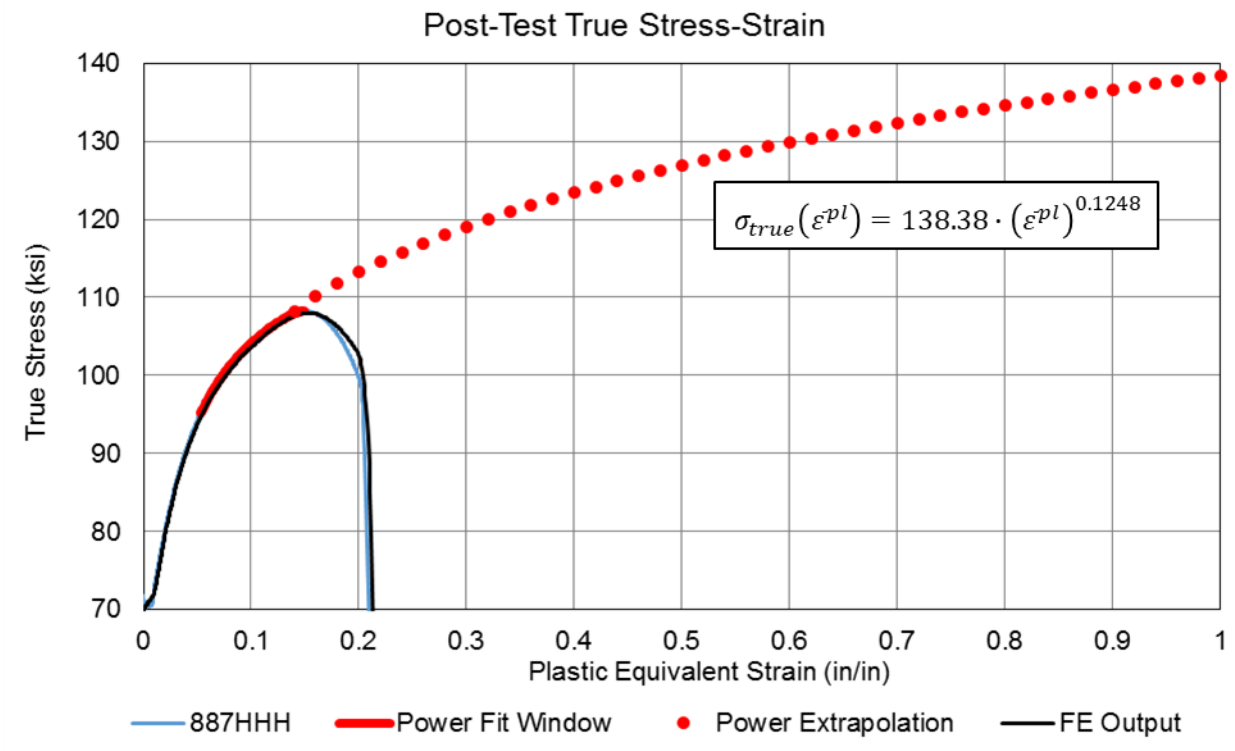

Figure F10. Calculated True Stress-Strain Characteristic of a Post-Test Tensile Coupon #887HHH (solid blue), Power Fit Window (solid red), Power Law Extrapolation (red circles), and FE Results (solid black)

Table F5 contains the tabular data used to define the isotropic plastic hardening of the TC128 material in the post-test FE model. The true stress response was extrapolated for large strains (according to Equation F4) starting at a plastic equivalent strain of 0.14 in/in, which was just before the UTS of the tensile coupon.

Table F5. True Stress and Plastic Equivalent Strain Inputs for Post-Test TC128 Material

True Stress psi	PEEQ in/in	True Stress psi	PEEQ in/in	True Stress psi	PEEQ in/in	True Stress psi	PEEQ in/in
7.025E+04	0.00E+00	1.117E+05	1.80E-01	1.256E+05	4.60E-01	1.333E+05	7.40E-01
7.025E+04	4.00E-03	1.132E+05	2.00E-01	1.263E+05	4.80E-01	1.337E+05	7.60E-01
7.025E+04	8.00E-03	1.145E+05	2.20E-01	1.269E+05	5.00E-01	1.342E+05	7.80E-01
7.475E+04	1.25E-02	1.158E+05	2.40E-01	1.275E+05	5.20E-01	1.346E+05	8.00E-01
8.025E+04	2.00E-02	1.170E+05	2.60E-01	1.281E+05	5.40E-01	1.350E+05	8.20E-01
8.625E+04	3.00E-02	1.180E+05	2.80E-01	1.287E+05	5.60E-01	1.354E+05	8.40E-01
9.075E+04	4.00E-02	1.191E+05	3.00E-01	1.293E+05	5.80E-01	1.358E+05	8.60E-01
9.425E+04	5.00E-02	1.200E+05	3.20E-01	1.298E+05	6.00E-01	1.362E+05	8.80E-01
9.700E+04	6.00E-02	1.209E+05	3.40E-01	1.304E+05	6.20E-01	1.366E+05	9.00E-01
9.925E+04	7.00E-02	1.218E+05	3.60E-01	1.309E+05	6.40E-01	1.369E+05	9.20E-01
1.028E+05	9.00E-02	1.226E+05	3.80E-01	1.314E+05	6.60E-01	1.373E+05	9.40E-01
1.064E+05	1.20E-01	1.234E+05	4.00E-01	1.319E+05	6.80E-01	1.377E+05	9.60E-01
1.083E+05	1.40E-01	1.242E+05	4.20E-01	1.324E+05	7.00E-01	1.380E+05	9.80E-01
1.101E+05	1.60E-01	1.249E+05	4.40E-01	1.328E+05	7.20E-01	1.384E+05	1.00E+00

Figure F11 shows the true stress-PEEQ inputs for Abaqus in the pre-test (Test 2 and Test 6) and post-test (Test 8) models. The Test 6 and Test 8 plasticity models are similar up to a PEEQ of 0.4 in/in but diverge afterwards due to the Test 6 model using linear extrapolation and the Test 8 model using a power law extrapolation at large strains.

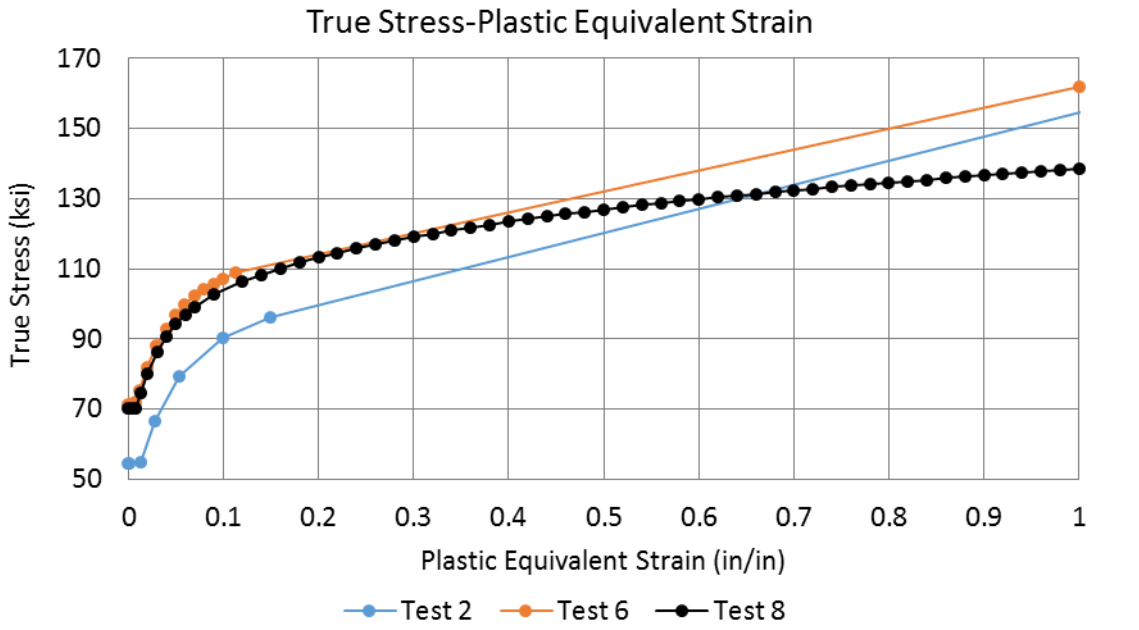

Figure F11. True Stress-Plastic Equivalent Strain Abaqus Inputs for Pre-Test (Test 2 and Test 6) and Post-Test (Test 8) Models

The tabular data used to define the damage initiation envelope of the post-test TC128 material was created using the B-W fracture criterion shown in Equation F2. The constants were calibrated via the Lee-Wierzbicki quick calibration procedure (Lee, Y.-W., & Wierzbicki, T, 2004) (Lee, Y.-W, 2005) using the average mechanical properties (see Appendix B4) from the round bar tensile coupon samples that were cut from the tank shell after the side impact test. The calibrated B-W constants are given in Table F6. The damage progression was specified as energy-based with linear softening and maximum degradation, and the fracture energy was set to 850 in-lbf/in^2.

Table F6. Bao-Wierzbicki Constants for Post-Test TC128 Material

a	b	x_0
0.201156	0.667887	0.4449058

Figure F12 shows that the post-test (Test 8) damage initiation envelope was nearly identical to the Test 6 pre-test model. This was expected given that the tensile coupons used to calibrate the envelopes were cut from both DOT-105 tank cars with certificates of construction showing that they were made by the same manufacturer at approximately the same time.

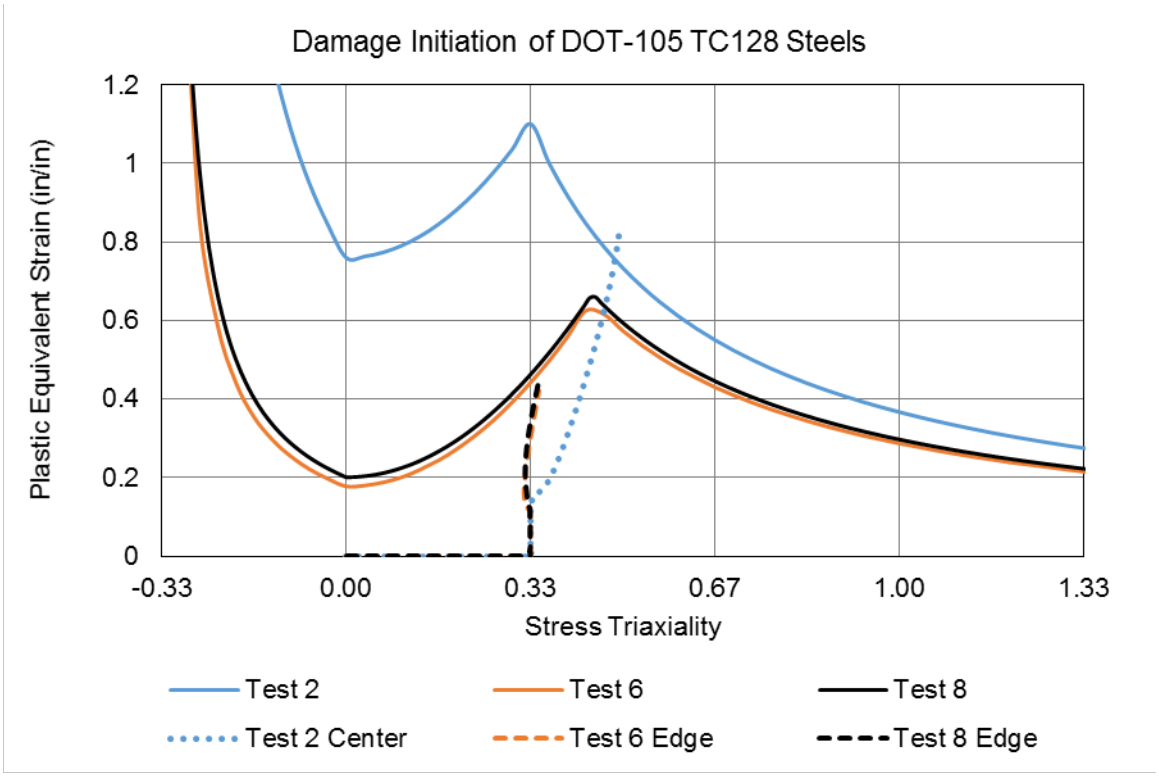

Figure F12. Damage Initiation Envelopes from Pre-Test TC128 Materials (Test 2 and Test 6) and Post-Test TC128 Material (Test 8) as Solid Lines and Dashed Lines Showing PEEQ-Triaxiality for Critical Element

Damage initiated at an approximate PEEQ of 0.4 in/in in the Test 6 and Test 8 coupons in the edge elements while it initiated at approximately 0.8 in/in in the Test 2 coupon in the center elements. Paredes et al. (2018) have shown that TC128 uniaxial tensile coupons tend to initiate fracture in the center of the specimen. Because of this, it is likely that the Test 6 and Test 8 damage initiation envelopes tend to underestimate the PEEQ associated with Mode II-Mixed Fracture and Mode III-Shear Fracture.

F5 – Foam Insulation

A simplified modeling approach was used to represent the foam insulation between the tank and the outer jacket. The basic technique for foam modeling was the same as found in the Abaqus Example Problem "Cask Drop with Foam Impact Limiter" (Abaqus Example Problems Manual, 2014). This example problem modeled a foam material using elasticity, plasticity, and density. While more sophisticated foam materials are available within the Abaqus modeling software, this simplified approach was chosen for the post-test models including foam insulation, as the intent was not to perform an in-depth analysis of the foam behavior. Rather, the post-test insulation modeling was undertaken to attempt to account for the force drop exhibited by the post-test model without material between tank and jacket.

From the certificate of construction for the DOT-105 tank car used in this test, the foam insulation was reported to have a density of 2 lbf/ft^3. The foam material described in the Abaqus example problem had a density of approximately 19 lbf/ft^3. Therefore, while the modeling techniques and general shape of the stress-strain curve from the example problem could be used

in the foam insulation modeling, the mechanical properties from the example problem could not be directly duplicated due to this difference in foam densities.

The desired mechanical properties were the modulus of elasticity of the foam and the collapse stress (i.e., the stress at which plastic behavior initiates in the model). The stress-strain response from the Abaqus example problem could then be scaled based on the collapse stress for foam having a density of 2 lbf/ft^3. A reference was found that provided relationships between compression/tension moduli and collapse stress of foams as functions of density (Goods, S. H., Neuschwanger, C. L., Whinnery, L. L, 1998). Values for modulus of elasticity and collapse stress were obtained using 2 lbf/ft^3 and this reference. The remainder of the stress-strain curve obtained from the Abaqus example problem were then scaled by the ratio of the calculated collapse stress to the collapse stress used in the example problem. A summary of the mechanical properties of the insulation foam is presented in Section 5.2.4.

The plastic stress-strain response obtained by using density relationships to scale the example plastic stress-strain behavior is shown in Figure F13 and the values are given in Table F7.

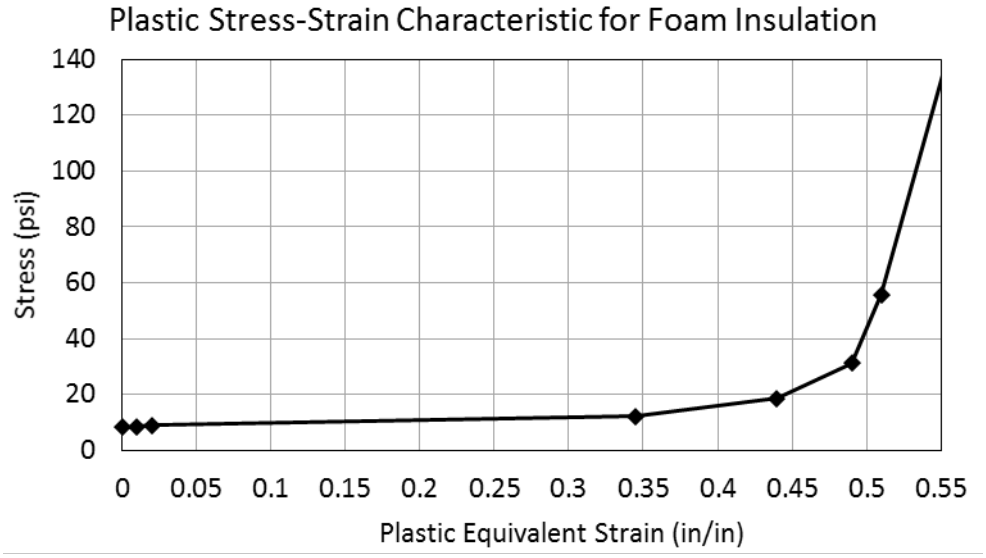

Figure F13. Plastic Stress-strain Characteristic of Foam Insulation

Table F7. Plastic Stress-strain Input for Foam Insulation

True Stress psi	**Plastic Strain** in/in
8.2100E+00	0.00E+00
8.5100E+00	1.00E-02
8.8600E+00	2.00E-02
1.2280E+01	3.45E-01
1.8660E+01	4.40E-01
3.1170E+01	4.90E-01
5.5760E+01	5.10E-01
2.8847E+03	2.00E+00

Finally, based on previous test observations from Carolan & Rakoczy (2019) that the foam breaks into pieces during impact, a strain-to-failure was implemented in the foam material. From Figure F13, it is apparent that this strain corresponds to the region where the foam experiences a steep increase in stress for an incremental increase in strain. When the plastic strain reached a value of 0.55 in a given element, that element would begin to fail. The plastic strain to initiate failure was fixed at 0.55 regardless of the stress triaxiality of the element. A damage progression energy of 1.0 in-lbf/in^2 was used to ensure a conservative failure model (i.e., a model that was likely to fail sooner than the physical material).

Abbreviations and Acronyms

ACRONYMS	EXPLANATIONS
ASTM	American Society for Testing and Materials
AAR	Association of American Railroads
B-W	Bao-Wierzbicki
K	Bulk Modulus
CFC	Channel Frequency Class
DOF	Degrees-of-Freedom
DUCTCRT	Ductile Criterion
EOS	Equations of State
FRA	Federal Railroad Administration
FE	Finite Element
FEA	Finite Element Analysis
C_p	Heat Capacity of Air
HD	High Definition
HHFT	High-Hazard Flammable Trains
HS	High Speed
KE	Kinetic Energy
ρ	Mass Density
MW	Molecular Weight
NDT	Non-Destructive Testing
PHMSA	Pipeline and Hazardous Materials Safety Administration
PEEQ	Plastic Equivalent
PRV	Pressure Relief Valve
RA	Reduction in Area
SSC	Shell-to-Solid Coupling
SPH	Smoothed Particle Hydrodynamics
SAE	Society of Automotive Engineers
c	Speed of Sound
TRIAX	Stress Triaxiality
TIH	Toxic by Inhalation
TC	Transport Canada

ACRONYMS	EXPLANATIONS
TTC	Transportation Technology Center (the site)
TTCI	Transportation Technology Center, Inc. (the company)
UTS	Ultimate Tensile Strength
DOT	United States Department of Transportation
R	Universal Gas Constant
Volpe	Volpe National Transportation Systems Center
YS	Yield Strength